UNIVERSITY OF OKLAHOMA

GRADUATE COLLEGE

SPIN RESOLVED CYCLOTRON RESONANCE IN InSb QUANTUM WELLS

A Dissertation

SUBMITTED TO THE GRADUATE FACULTY

In partial fulfillment of the requirements for the

degree of

Doctor of Philosophy

By

ROBERT MEYER
Norman, Oklahoma
2005

UMI Number: 3162829

UMI Microform 3162829

ProQuest Information and Learning Company
300 North Zeeb Road
P.O. Box 1346
Ann Arbor, MI 48106-1346

SPIN RESOLVED CYCLOTRON RESONANCE IN InSb QUANTUM WELLS

A DISSERTATION APPROVED FOR THE
DEPARTMENT OF PHYSICS AND ASTRONOMY

BY

Michael Santos (Advisor)

Ryan Doezema (Co-Advisor)

Bruce Mason

Sheena Murphy

Patrick McCann

Acknowledgements

First, I would like to thank my wonderful family, especially my mother, my sister Beverly and my brother Christopher. They have always given me complete support in whatever I have tried to accomplish and I'm convinced that without that support my success in school, as well as almost all other areas of my life, would have been far more limited.

I would also like to thank my advisors, Mike Santos and Ryan Doezema, who's guidance and training throughout my graduate career obviously played a key role in my research. I've enjoyed working with them, as well as their friendship.

In addition, I owe a great deal of thanks to Dr. Y. J. Wang at the National High Magnetic Field Laboratory in Tallahassee, Florida. Without his excellent expertise and help, the experiments conducted there would not have been nearly as successful and enlightening.

I would also like to acknowledge my fellow graduate students who I worked with and who helped train me and provided the necessary samples for this work, Giti Khodaparast, Ning Dai, Kory Goldhammer, Soekjae Chung, Niti Goel and Taroshani Kasturiarachchi.

Finally, I would like to thank the machine shop staff for helping to design and make the experimental setup, Joel Young, Bob Littell, and Berry Bergeron.

Contents

Abstract

In this study we looked at spin resolved cyclotron resonance in InSb quantum wells. InSb is an attractive material for this type of work due to its small electron effective mass (0.014 m_o), high intrinsic electron mobility, large electron g-factor (-51), and non-parabolic conduction band. The energies of the spin resolved transitions agreed with calculated values, even though some discrepancies in the intensities were evident. We used this spin-resolved cyclotron resonance to observe and study four subband Landau level avoided level crossings. These observed avoided level crossings are associated with the lowest Landau levels of the ground and first excited subbands of the InSb quantum wells. It was found that the energy gaps associated with anti-crossings of the same spin Landau levels depend on the tilt of the sample with respect to the magnetic field direction. This result is consistent with earlier, non spin-resolved, studies of Landau level coupling in GaAs quantum wells. We also observed anti-crossings associated with Landau Levels of opposite spin, with energy gaps that are essentially independent of sample tilt angle. Opposite spin anti-crossings are not expected from the theory explaining the GaAs experiments. Although spin-orbit effects are strong in InSb, the origins of the opposite spin anti-crossings are not definitively identified.

Chapter 0

Introduction

The unique characteristics of the III-V narrow gap semiconductors make them a natural choice for the study of fundamental physics. Of the various III-V semiconductor systems, InSb possess the smallest electron effective mass (0.014 m_o), the highest intrinsic electron mobility at room temperature, the largest electron g-factor (-51), and the most non-parabolic electron dispersion relation. These characteristics make InSb an excellent candidate for band structure studies and experimental exploration of spin properties. The study of these properties is the motivation behind this work.

The band structure of InSb can be described experimentally by Kane ($k \bullet p$) or Luttinger models [1, 9]. These models will be investigated in chapter 1. The purpose of this chapter is to explore some of the theories of narrow gap semiconductors. Non-parabolicity in the band structure as well as the InSb/$Al_xIn_{1-x}Sb$ band offset will be discussed. In addition, the theoretical foundation surrounding Landau levels and the resulting fan diagrams will be investigated. Finally, the numerical methods used to calculate these quantities will be explored.

The purpose of chapter 2 is to discuss the InSb quantum well structure, as well as sample preparation, and some of the experimental techniques used to

measure the transport, transmission, and photo-conductivity properties of the samples. These measurements can then be used to determine some of the fundamental properties of the InSb quantum wells.

Chapter 3 will discuss the spin-split cyclotron resonance experiments conducted for this work at the National High Magnetic Field Lab (NHMFL) in Tallahassee, Florida. The sample's layer structure as well as its energy profile will be reviewed. The experimental setup at the NHMFL will be discussed as well. The fan diagram / Landau level plots will then be touched upon again, but derived in a less rigorous fashion than previously. Then, some representative data of both the cyclotron resonance energies as well as intensities will be examined and an interpretation of the data will be made in light of the established theoretical backdrop.

In chapter 4 the focus will be on using cyclotron resonance to probe anti-crossings that occur between Landau levels of different subbands within the same quantum well. Specifically, this chapter will discuss anti-crossings that occur between same spin states. Chapter 5 will consider opposite spin anti-crossings. To begin, we will review the sample structure once more in order to understand how the fan diagram changes with the inclusion of different subbands in the well. We will then touch on previous experiments done using GaAs [62, 63, 64] where the first evidence of anti-crossings was observed. Next, a theoretical foundation

will be discussed to explain the anti-crossings and a comparison will be made between the theoretical and experimental results for the same spin crossings.

Finally, the purpose of chapter 6 will be to summarize the data and results of the previous two chapters and to discuss future improvements to the OU light pipe assembly in order to reduce previous signal-to-noise problems with the OU FTIR experimental setup and further extend this work. A discussion of the positions of both the same spin and opposite spin anti-crossings in B-field for sample s842 will be covered. Specifically, the adjustment of various parameters in the calculated fan diagrams in order to bring the theory more in line with the observed positions will be discussed. This discussion can then be extended to other samples in this study. Also, some possible anti-crossings seen in the data for samples s499, s702, and s716 will be discussed.

Chapter 1

Theoretical Foundations

The purpose of this chapter is to explore some of the theories of narrow gap semiconductors. Non-parabolicity in the band structure as well as the determination of the band offset will be discussed. In addition, the theoretical foundation surrounding Landau levels and the resulting fan diagrams will be investigated. Finally, the numerical methods used to calculate these quantities will be explored.

1.1 Introduction

InSb is a direct band gap semiconductor. The important parts of the band structure for this material are the conduction, heavy hole, light hole, and spin-orbit bands. An example of this type of band structure, near the band edges of such a direct band gap semiconductor, is shown in Figure 1.1. The band gap for InSb is approximately 0.236 eV at 4 K with a $0.014m_0$ conduction band edge effective mass.

In addition to being a direct band gap semiconductor, InSb also possesses a strongly non-parabolic band structure. The result of this non-parabolicity is an energy dependent effective mass and g-factor. The Kane model [1] is capable of

describing this non-parabolicity and will be covered in the next section. Also, in the InSb/$Al_xIn_{1-x}Sb$ heterostructures used in this study, there exists a lattice mismatch between the InSb and $Al_xIn_{1-x}Sb$ layers. This results in the quantum

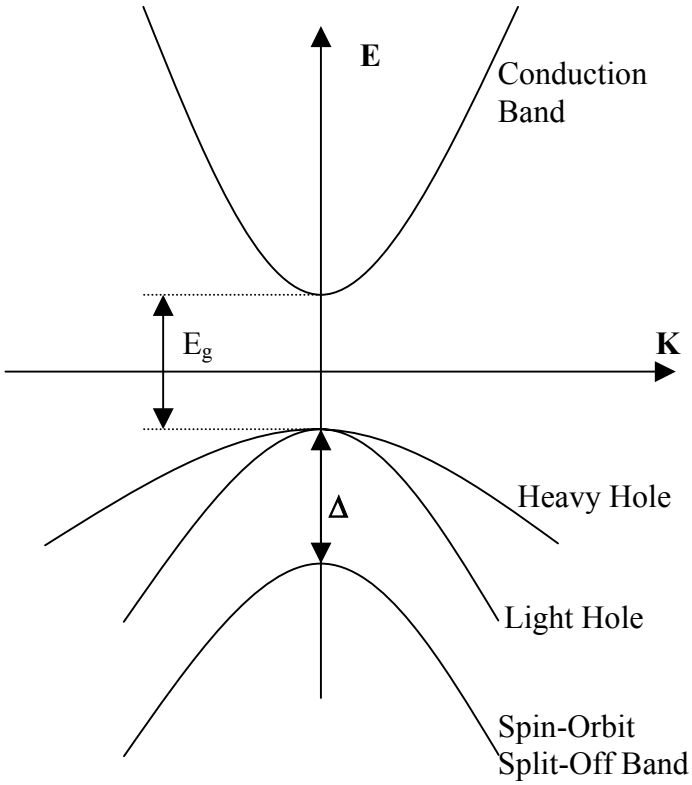

Figure 1.1: Typical band structure of a direct band gap semiconductor showing the conduction, heavy hole, light hole, and spin-orbit bands.

well being under strain, resulting in a strain dependent band gap and splitting of the heavy hole and light hole bands. The resulting band alignment is shown in Figure 1.2.

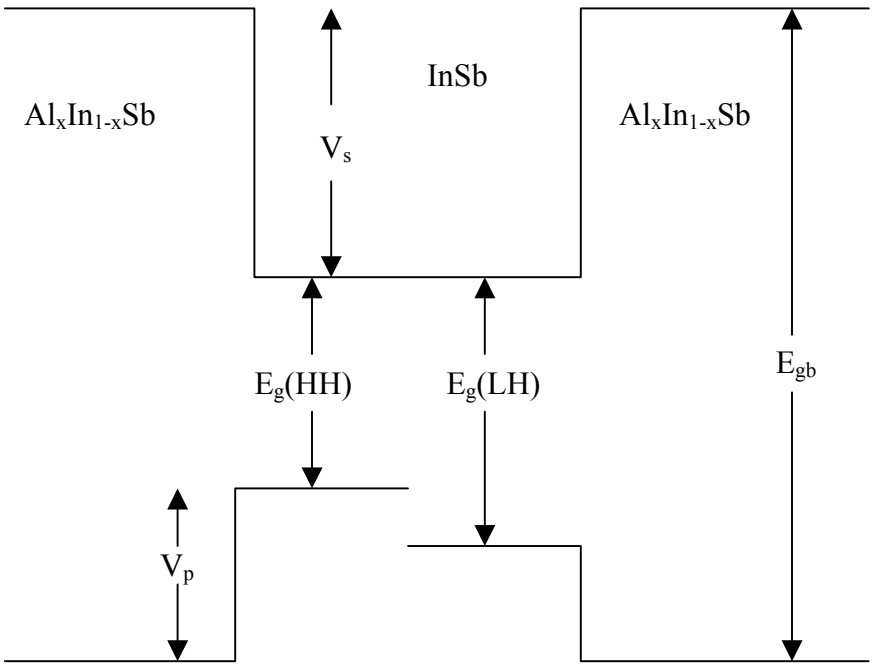

Figure 1.2: InSb/$Al_xIn_{1-x}Sb$ band alignment. Since the well is under strain due to lattice mismatch, the heavy hole and light hole bands are split.

1.2 The Kane Model (a.k.a the k•p theory)

For any solid, the dependence of the electron's energy on the wave vector, (i.e. - the band structure) is defined by the Schrödinger equation. For an electron in a periodic potential and in the absence of the spin-orbit interaction, the Schrödinger equation is given by [2, 3, 4]:

$$\frac{-\hbar^2}{2m_0}\nabla^2\Psi(r) + V(r)\Psi(r) = E(k)\Psi(r) \tag{1.1}$$

$$V(\mathbf{r}) = V(\mathbf{r} + \mathbf{R}) \tag{1.2}$$

$$\mathbf{R} = n_1\mathbf{e}_1 + n_2\mathbf{e}_2 + n_3\mathbf{e}_3 \tag{1.3}$$

where $\mathbf{e}_1$, $\mathbf{e}_2$, and $\mathbf{e}_3$ are the lattice vectors and n_1, n_2, and n_3 are integers.

Notice that $\Psi(\mathbf{r})$ and $\Psi(\mathbf{r} + \mathbf{R})$ are both solutions of the Hamiltonian. This suggests that the Hamiltonian is invariant under lattice vector translations $\mathbf{r} \rightarrow \mathbf{r} + \mathbf{R}$. Also, from the Bloch theorem, the solution of the Hamiltonian given above can be rewritten as:

$$\Psi_{nk}(\mathbf{r}) = e^{i\mathbf{k}.\mathbf{r}}\, u_{nk}(\mathbf{r}) \tag{1.4}$$

where $u_{nk}(\mathbf{r})$ is a periodic function, n is the band index, and k is the wavevector. Substituting this back into Equation (1.1) and using the fact that $\frac{\hbar}{i}\nabla = p$, the Schrödinger equation becomes [4]:

$$[\frac{p^2}{2m_0} + \frac{\hbar}{m_0}\vec{k} \bullet \vec{p} + V(\vec{r})]u_{nk}(\vec{r}) = [E_n(\vec{k}) - \frac{\hbar^2 k^2}{2m_0}]u_{nk}(\vec{r}) \tag{1.5}$$

Notice the $\mathbf{k}\bullet\mathbf{p}$ term that is now present in the Hamiltonian. This is the $\mathbf{k}\bullet\mathbf{p}$ Hamiltonian for which the theory is named. This Hamiltonian results in a 2-band model. These two bands are the familiar conduction band (CB) and valence band (VB).

However, the $\mathbf{k}\bullet\mathbf{p}$ Hamiltonian given in Equation (1.5) does not yet contain the spin-orbit interaction. With this interaction included, the Hamiltonian takes on the following form [4]:

$$[\frac{p^2}{2m_0} + \frac{\hbar}{m_0}\vec{k} \bullet \vec{p} + V(\vec{r}) + \frac{\hbar}{4m_0^2c^2}[\vec{\nabla}V \times \vec{p}] \bullet \vec{\sigma} + \frac{\hbar^2}{4m_0^2c^2}\vec{\nabla}V \times \vec{k} \bullet \vec{\sigma}]u_{nk}(\vec{r}) = E' u_{nk}(\vec{r}) \tag{1.6}$$

where $$E' = [E_n(\vec{k}) - \frac{\hbar^2 k^2}{2m_0}] \quad (1.7)$$

The inclusion of the spin-orbit interaction removes the degeneracy in the valence band, resulting in the heavy-hole (HH), light-hole (LH), and split-off (SO) bands (see Figure 1.1).

In this case, the dispersion relation is doubly degenerate with the following solutions:

$$E' = -E_g \quad (1.8)$$

$$E'(E' + E_g)(E' + E_g + \Delta) - k^2 P^2 (E' + E_g + 2/3*\Delta) = 0 \quad (1.9)$$

Note, these solutions assume the bottom of the conduction band as the zero point energy [2]. Also, the parameter P in Equation (1.9) is a measure of the coupling between the conduction band and the valence band, and is given by:

$$P = -i \frac{\hbar}{m_0} \langle S | p_z | Z \rangle \quad (1.10)$$

In addition, in Equation (1.9), Δ is the spin-orbit split-off energy and E_g is the band gap (refer to Figure 1.1).

At $k \approx 0$, there will be three solutions to Equation (1.9):

$$E' = 0 \quad (1.11)$$

$$E' = -E_g \quad (1.12)$$

$$E' = -E_g - \Delta \quad (1.13)$$

In the vicinity of k = 0, consider a small term $\varepsilon(k^2)$ where $\varepsilon(k^2) << E_g$ and

$\varepsilon(k^2) << \Delta$. Adding this term to these three solutions we get the following solutions in the vicinity of k = 0:

$$E' = 0 + \varepsilon(k^2) \tag{1.14}$$

$$E' = -E_g + \varepsilon(k^2) \tag{1.15}$$

$$E' = -\Delta - E_g + \varepsilon(k^2) \tag{1.16}$$

Now, considering these three solutions and assuming that the top of the valence band as zero energy [4], the dispersion relations for the CB, HH, LH and SO will have the following forms:

$$E_{CB} = E_g + \frac{\hbar^2 k^2}{2m_0} + \frac{k^2 P^2 (E_g + 2\Delta/3)}{E_g (E_g + \Delta)} \tag{1.17}$$

$$E_{HH} = \frac{\hbar^2 k^2}{2m_0} \tag{1.18}$$

$$E_{LH} = \frac{\hbar^2 k^2}{2m_0} - \frac{2k^2 P^2}{3E_g} \tag{1.19}$$

$$E_{SO} = -\Delta + \frac{\hbar^2 k^2}{2m_0} - \frac{k^2 P^2}{3(E_g + \Delta)} \tag{1.20}$$

At this point it should be noted that the Kane model does not include the effect of higher bands. This fact results in an incorrect effective mass for the heavy holes. The Kane model is, however, sufficient to describe the effective mass of both the electrons and the light holes. From Equation (1.9) this energy dependent effective mass has the form:

$$\frac{1}{m^*(E')} = \frac{2P^2}{3}\left[\frac{2}{E'+E_g} + \frac{1}{E'+E_g+\Delta}\right] \tag{1.21}$$

In some materials, the energy E' is negligible when compared to E_g and Δ and can usually be ignored. However, in narrow gap materials like InSb, this is not the case. This implies that these non-parabolicity corrections are indeed important. The result of the Kane model for the effective mass will be used in the following sections in order to define the subband energies in doped quantum wells.

1.3 Sub-bands for Doped Quantum Wells

The main goal of the self-consistent computer simulations discussed in this section is solving the Schrödinger and Poisson equations for a remotely doped $Al_xIn_{1-x}Sb$/InSb square quantum well (SQW) in order to determine the subband energies for the conduction and valence bands. Because InSb possesses such a large dielectric constant and small effective mass, the exchange potential has a small contribution. This results in the Hartree potential being the dominant term. This Hartree potential should, of course, be calculated self consistently.

The Schrödinger equation inside a square quantum well is given by:

$$\left[\frac{\partial}{\partial z}\left(\frac{-\hbar^2}{2m_1^*(E_i,z)}\right)\frac{\partial}{\partial z} - E_i + V_1(z) + \frac{\hbar^2 K_t^2}{2m_1^*(E_i,z)}\right]\Psi_{1i,kt}(z) = 0 \tag{1.22}$$

where *i* is the subband index and K_t is the transverse wave vector. Likewise, the Schrödinger equation outside the well is given by:

$$\left[\frac{\partial}{\partial z}\left(\frac{-\hbar^2}{2m_2^*(E_i,z)}\right)\frac{\partial}{\partial z} - E_i + V_2(z) + \frac{\hbar^2 K_t^2}{2m_2^*(E_i,z)}\right]\Psi_{2i,kt}(z) = 0 \qquad (1.23)$$

In these Schrödinger equations, $m_1^*(E_i,z)$ and $m_2^*(E_i,z)$ are the energy dependent effective masses in the well and the barrier respectively. If the bottom of the square well is defined as zero energy, then $V_1(z) = V_H(z)$ where $V_H(z)$ is the Hartree, or electrostatic potential. Likewise, $V_2(z) = (E_{gBarrier} - E_{gWell})$ x Q where Q is the offset. This offset has been determined experimentally for InSb quantum wells to be approximately 62% [5].

The Hartree (or electrostatic) potential mentioned above is given by:

$$\nabla^2 V_H(z) = \frac{-n(z)e^2}{\kappa\varepsilon_0} \qquad (1.24)$$

where ε_0 is the vacuum dielectric constant and κ is the relative dielectric constant for the material in question. For InSb, κ is equal to 17.7. The electron distribution is obtained by:

$$n(z) = \sum_{i=1}^{N}\left(\sum_{K_t=0}^{K_{Fi}}\left|\Psi_{i,K_t}(z)\right|^2\right) \qquad (1.25)$$

where N is the number of occupied subbands and K_{Fi} is the Fermi wavevector for the different subbands. The second summation in Equation (1.25) can be rewritten as:

$$\sum_{K_t=0}^{K_{Fi}}\left|\Psi_{i,K_t}(z)\right|^2 = \frac{2}{(2\pi)^2}\int_0^{K_{Fi}} d^2K_t\left|\Psi_{i,K_t}(z)\right|^2 = \frac{1}{\pi}\int_0^{K_{Fi}} K_t\,dK_t\left|\Psi_{i,K_t}(z)\right|^2 \qquad (1.26)$$

Note that the factor of 2 in the second term of Equation (1.26) is due to the two spin states of the electrons. With Equations (1.25) and (1.26) in mind, Poisson's equation (1.24) becomes:

$$\nabla^2 V_H(z) = \frac{-e^2}{\kappa\varepsilon_0} \sum_{i=1}^{N} \frac{1}{\pi} \int_0^{K_{Fi}} K_t \, dK_t \left| \Psi_{i,K_t}(z) \right|^2 \tag{1.27}$$

Assuming that $V_H(z) = 0$, a self-consistent procedure will produce a set of wave functions. These wave functions are then used in Equation (1.27) to calculate $V_H(z)$. This $V_H(z)$ will then be substituted back into the Schrödinger equation in order to generate a new set of subband energies. This procedure is then repeated until variations in the calculated potential converges to some acceptably small value.

1.4 Numerical Techniques

1.4.1 Solving the Schrödinger Equation

In order to solve the Schrödinger equation numerically, the *Runge-Kutta* [6] method of fourth order was used. To employ this method, the spatial dimension in question, in this case the region containing the quantum well, is first divided into evenly spaced points. For simplicity, throughout the calculation, the width of the quantum well is scaled to one, and the Schrödinger equation is divided by $\frac{\hbar^2}{2m^* W^2}$ where W is the width of the well [6]. Using this method, the

wave function and its first derivative on each grid point can be determined as follows:

$$\Psi(z+h)=\left[1+\frac{h^2A(z)}{6}+\frac{h^2A(z+h/2)}{3}+\frac{h^4A(z)A(z+h/2)}{24}\right]\Psi(z)$$

$$+\left[1+\frac{h^2A(z+h/2)}{6}\right]h\Psi'(z) \qquad (1.28)$$

$$\Psi'(z+h)=\left[1+\frac{h^2A(z+h/2)}{3}+\frac{h^2A(z+h)}{6}+\frac{h^4A(z+h)A(z+h/2)}{24}\right]\Psi'(z)$$

$$+[A(z)+4A(z+h/2)+A(z+h)+\frac{h^2A(z)A(z+h/2)}{2}$$

$$\frac{h^2A(z+h)A(z+h/2)}{2}]\frac{h}{6}\Psi(z) \qquad (1.29)$$

where

$$A(z)=\frac{V(z)-E_{i,K_t}}{\frac{\hbar^2}{2m^*W^2}}+k_tW^2 \qquad (1.30)$$

is a unitless variable and h is the grid size. It should also be noted that the *Runge-Kutta* method needs an initial guess for the wave function and its first derivative.

Using Equations (1.28) and (1.29) above, the wave function and its first derivative can be determined on each grid point. In a quantum well system such as $Al_xIn_{1-x}Sb/InSb$, the bound states can be found by propagating the wave function from a grid point in the barrier and the well regions to a matching point.

The bound states are those states for which the Wronskien at the matching point goes to zero. The Wronskien is given by:

$$Wr(z) = \Psi_l(z)\Psi'_r(z) - \Psi_r(z)\Psi'_l(z) \tag{1.31}$$

The indicies *l* and *r* correspond to the solutions from the left and right sides of the matching point.

A C++ computer program, which performs the calculation described above, was written by Giti Khodaparast [6] and was used for all the subsequent calculations in this work.

1.5 Sub-Bands in Undoped QW: Bastard Formalism

1.5.1 Subband Energies ($K_t = 0$)

Consider a square quantum well of narrow gap material with the Hamiltonian given by [2]:

$$\left[p_z \frac{1}{2m(E,z)} p_z + V_s(z) \right] f(z) = Ef(z) \tag{1.32}$$

The function f(z) and $\frac{1}{m(E,z)}\frac{df(z)}{dz}$ are continuous at the well-barrier interface. m(E,z) is the energy dependent effective mass and in the presence of band bending, it has an explicit position dependence. The solutions of a square quantum well are well known, with the dispersion relation for both odd and even solutions in the well:

$$\cos(k_w L) - \frac{1}{2}[-\xi + \frac{1}{\xi}]\sin(k_w L) = 0 \tag{1.33}$$

$$\xi = (m_b(E)K_w)/(m_w(E)K_b) \tag{1.34}$$

$$\frac{1}{m_w} = \frac{2P^2}{3}\left[\frac{2}{E+E_{gw}} + \frac{1}{E+E_{gw}+\Delta_w}\right] \tag{1.35}$$

$$\frac{1}{m_b} = \frac{2P^2}{3}\left[\frac{2}{E-V_s+E_{gb}} + \frac{1}{E+E_{gb}+\Delta_b}\right] \tag{1.36}$$

The Kane model discussed previously gives the wave vectors in the well and the barrier for electrons and light holes:

$$K_w^2 = \frac{E(E+E_{gw})(E+E_{gw}+\Delta_w)}{\hbar^2 P^2 (E+E_{gw}+\frac{2\Delta_w}{3})} \tag{1.37}$$

$$K_b^2 = \frac{(E-V_s)(E-V_s+E_{gb})(E-V_s+E_{gb}+\Delta_b)}{\hbar^2 P^2 (E-V_s+E_{gb}+\frac{2\Delta_b}{3})} \tag{1.38}$$

For heavy holes, the dispersion relation is parabolic and the associated wave vectors for the well and barrier are given by:

$$k_w = \sqrt{-2m_{hhw}(E_{gw}+E)}/\hbar \tag{1.39}$$

$$k_b = \sqrt{-2m_{hhb}(E_{gw}+E+V_p)}/\hbar \tag{1.40}$$

The effective mass of the heavy holes is related to the Luttinger parameters which will be discussed in the next section. The bound states are the solutions of Equation (1.33) and can be calculated using any number of numerical techniques. Also, the terms $V_s(z)$ and $V_p(z)$ are defined in Figure 1.3.

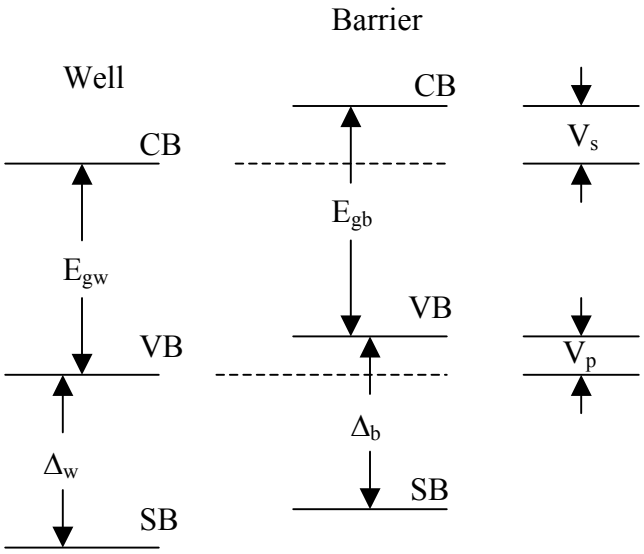

Figure 1.3: Relationship between V_s, V_p, and the various band parameters.

1.5.2 Subband Energies for $K_t \neq 0$

The wavevectors in the well and barrier for $K_t \neq 0$ have the following forms [8]:

$$K_w^2 = \frac{E(E+E_{gw})(E+E_{gw}+\Delta_w)}{\hbar^2 P^2 (E+E_{gw}+\frac{2\Delta_w}{3})} - K_t^2 \tag{1.41}$$

$$K_b^2 = K_t^2 - \frac{(E-v_s)(E-v_s+E_{gb})(E-v_s+E_{gb}+\Delta_b)}{\hbar^2 P^2 (E-v_s+E_{gb}+\frac{2\Delta_b}{3})} \tag{1.42}$$

And the bound states are the solutions of the following dispersion relation:

$$\cos(k_w L) + \frac{1}{2}\left[\frac{K_b m_w}{m_b K_w} - \frac{K_w m_b}{m_w K_b} - \frac{K_t^2}{K_w K_b}\frac{(\eta_w-\eta_b)^2}{m_w m_b}\right]\sin(k_w L) = 0 \tag{1.43}$$

where

$$\frac{1}{\eta_w} = \frac{2P^2}{3}\left[\frac{1}{E+E_{gw}} - \frac{1}{E+E_{gw}+\Delta_w}\right] \tag{1.44}$$

$$\frac{1}{\eta_b} = \frac{2P^2}{3}\left[\frac{1}{E - V_s + E_{gb}} - \frac{1}{E + E_{gb} + \Delta_b}\right] \tag{1.45}$$

1.6 Luttinger Model

As stated earlier, the Kane model does not produce the correct effective mass for heavy holes [7]. This deficiency can be overcome, however, by using the Luttinger model to define the heavy hole effective mass. This model describes the valence bands more accurately than the Kane model. It also includes the warping of the valence band. This latter fact is very important and cannot be ignored in InSb. The details of the Luttinger model can be found in several different references such as Ref. [9, 10]. This model produces a valence band dispersion relation given by:

$$E(k) = \frac{\gamma_1 \hbar^2 k^2}{2m_0} \pm \frac{\hbar^2}{m_0}\left[\gamma_2^2 k^4 + 3(\gamma_3^2 - \gamma_2^2)(k_x^2 k_y^2 + k_y^2 k_z^2 + k_z^2 k_x^2)\right]^{1/2} \tag{1.46}$$

In Equation (1.46), the γ's are the standard Luttinger parameters which can be found in Landolt-Börnstein [11]. And although for this analysis, the calculation of the heavy hole effective masses is of primary interest, corresponding to the (-) in Equation (1.46), this model can also be used to calculate the light hole effective masses by using the (+) sign in the above equation.

This dispersion relation for heavy and light holes can be rewritten using Luttinger's valence band Hamiltonian for k ‖ [001] as:

$$E_{\pm} = \frac{\hbar^2}{2m_0}(\gamma_1 \pm 2\gamma_2)k^2 \tag{1.47}$$

Using this dispersion relation, the band edge effective masses for heavy holes and light holes becomes:

$$m^*_{hh} = \frac{m_0}{(\gamma_1 - 2\gamma_2)} \tag{1.48}$$

$$m^*_{lh} = \frac{m_0}{(\gamma_1 + 2\gamma_2)} \tag{1.49}$$

where γ_1 and γ_2 are, of course, the Luttinger parameters.

At this point it is important to note that the band edge effective mass and the cyclotron mass are the same only when the constant energy surfaces are spherical, i.e. - when $\gamma_2 = \gamma_3$. Thus, with the warping of the energy surfaces in systems such as InSb, it is important to distinguish between the cyclotron mass and the band edge effective mass. With this distinction in mind, the cyclotron masses can be related to the Luttinger parameters for when B ‖ [001] by:

$$m^*_{hh} = \frac{m_0}{\gamma_1 - \{\gamma_2^2 + \frac{3}{4}(\gamma_2 + \gamma_3)^2\}^{1/2}} \tag{1.50}$$

$$m^*_{lh} = \frac{m_0}{\gamma_1 + \{\gamma_2^2 + \frac{3}{4}(\gamma_2 + \gamma_3)^2\}^{1/2}} \tag{1.51}$$

1.7 Interaction of a 2DEG with a Magnetic Field

1.7.1 Landau Levels (a.k.a – Fan Diagram)

From a classical viewpoint, the motion of an electron in a uniform magnetic field follows a closed circular orbit. Quantum mechanically, the energy of an electron in such a closed orbit must have quantized values. The quantized energy levels of this two dimensional motion are referred to as Landau Levels [12, 13]. The goal of this section is to derive and discuss these Landau Levels.

Consider electron moving in a uniform magnetic field in the z – direction. In this case the Hamiltonian is of the form [6]:

$$H = \frac{1}{2m^*}(\nabla + e\vec{A})^2 + V(z) \tag{1.52}$$

Since the magnetic field is in the z – direction, in the symmetric gauge, **A** is given by:

$$\vec{A} = \frac{-B}{2}(y,-x,0) \tag{1.53}$$

By applying the following transformation:

$$\mathbf{A} = \mathbf{A} + \nabla \Lambda \tag{1.54}$$

$$\Lambda = -Bxy/2 \tag{1.55}$$

A will then be changed into the Landau gauge:

$$\mathbf{A} = -B(y, 0, 0) \tag{1.56}$$

Thus, the Hamiltonian becomes:

$$H = \frac{1}{2m^*}(\nabla_x - eBy)^2 + \frac{1}{2m^*}\nabla_y^2 + \frac{1}{2m^*}\nabla_z^2 + V(z) \tag{1.57}$$

Since this Hamiltonian commutes with $\nabla_{x,}$ the wavefunction can be written as:

$$\psi = e^{ikx} f(x)\, \Phi(y) \tag{1.58}$$

This results in the Schrödinger equation being written as:

$$\nabla_y^2 \Phi(y) f(z) + \left[\frac{2m^* E}{\hbar^2} - \frac{m^2 \omega_c^2}{\hbar^2} (y - y_0)^2 \right] \Phi(y) f(z) - [\nabla_z^2 f(z) + V(z) f(z)] \Phi(y) = 0 \tag{1.59}$$

where $\omega_c = \frac{eB}{m^*}$ and $y_0 = \frac{\hbar k_x}{eB}$. Notice that this Schrödinger equation is the equation for a shifted harmonic oscillator. An equation of this type has solutions of the form:

$$E = (n + \tfrac{1}{2})\hbar\omega_c + E_z \qquad n = 0,1,2,... \tag{1.60}$$

The first term in Equation (1.60) corresponds to the energies due to the electron's motion in the plane (in this case the xy-plane) perpendicular to the magnetic field. These energies are referred to as Landau Levels. The E_z term in Equation (1.60) is the solution along the z-axis.

Next, including the energy due to the electron's spin, Equation (1.60) becomes:

$$E = E_z + (n + \tfrac{1}{2})\hbar\omega_c \pm \tfrac{1}{2} g\mu_B B \tag{1.61}$$

where the – refers to spin down (i.e. electron's spin anti-aligned with the magnetic field) and the + refers to spin up (i.e. electron's spin aligned with the magnetic field). Thus, each Landau level is further divided into two spin-split energy levels. Quantum mechanically, electron transitions between Landau levels of the

same spin are referred to as cyclotron resonance transitions, while transitions between spin-split states of the same Landau level are called spin resonances. A simple diagram depicting these two types of transitions, in the absence of non-parabolicity, is given in Figure 1.4.

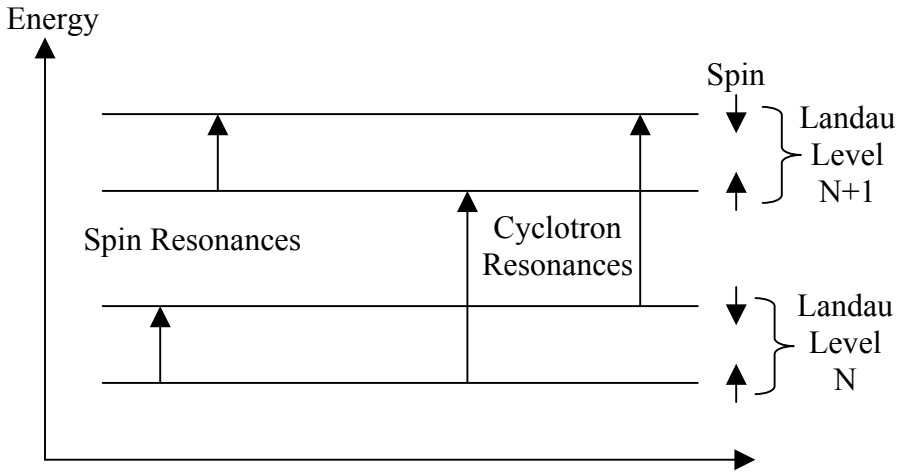

Figure 1.4: A simple picture of cyclotron and spin resonance. Note that cyclotron resonance occurs when $\Delta n = 1$ and $\Delta s = 0$ and spin resonance when $\Delta n = 0$ and $\Delta s = -1$

Of course, in an actual system, the samples have impurities and defects. Collisions between the electrons in the samples and these impurity atoms or defects account for the majority of the energy dissipation of the electrons in the samples. The result of this is that, rather than the Landau levels being a sharp energy level as they would be in a pure material, in the presence of impurities the Landau levels will spread out into a band which contains many distinct energy levels. States near the bottom and near the top of the Landau level are localized states, and therefore electrons trapped in these states cannot contribute to current

carried through the sample. However, near the center of each band the states are spatially extended. Electrons in these states are mobile and can therefore carry current through the sample. Thus, each Landau Level can be occupied by a large number of electrons that all possess the nearly the same energy. The population of these levels changes with the strength of the magnetic field. The magnetic length of the electrons within the sample is give by:

$$l = \left(\frac{\hbar}{eB} \right)^{1/2} \tag{1.62}$$

which will clearly decrease with increasing magnetic field. This, in turn, results in an increasing degeneracy of the Landau Levels [12, 13] given by:

$$D = \frac{1}{2\pi l^2} = \frac{eB}{h} \tag{1.63}$$

The number of occupied Landau Levels is referred to as the *filling factor* and is defined by:

$$\nu = N / D \tag{1.64}$$

where N is the number of electrons per unit sample area. Figure 1.5 shows an example of a 5 electron system demonstrating the ideas discussed above.

As can be seen in the figure, at high magnetic fields, all the electrons lie in the lowest Landau Level ($\nu < 1$). By reducing the magnetic field strength, the spacing, as well as the degeneracy of the Landau levels, decreases. Thus, there will be a magnetic field such that the lowest Landau Level is exactly filled. When this occurs, $\nu = 1$. Extending this line of reasoning, as the magnetic field is still

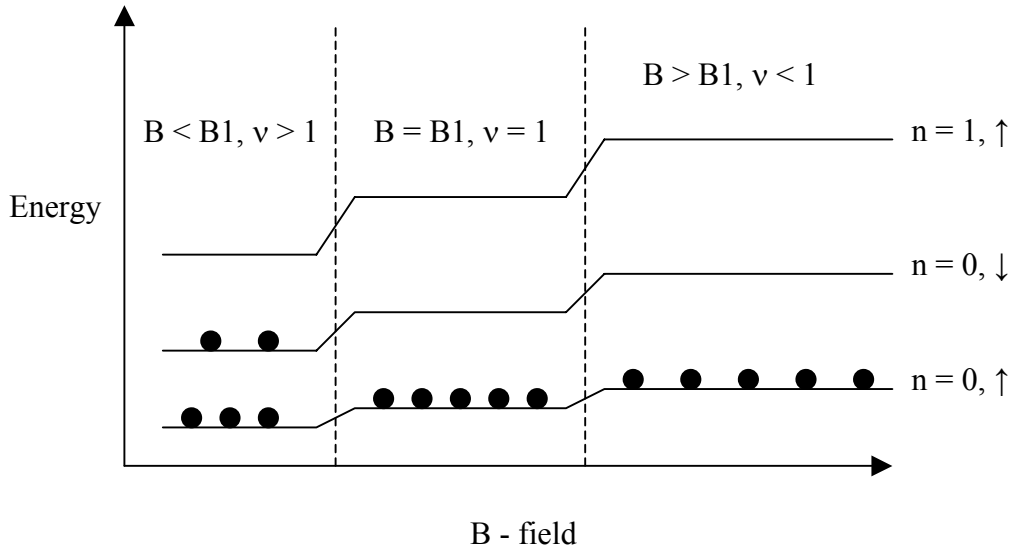

Figure 1.5: The three lowest Landau Levels for a sample 5 electron system. At B = B1 the lowest Landau Level is exactly filled (ν = 1). For smaller B, some electrons are forced into higher levels (ν > 1) resulting in a reduction of the degeneracy of the system [12].

decreased further, at some point the two lowest Landau Levels will be exactly filled (ν = 2), and so on. Thus, for any integer value *i* there is a magnetic field:

$$B_i = \frac{Nh}{ie} \tag{1.65}$$

for which the *i*th lowest Landau Levels are completely filled and all higher levels are empty. This effect leads to the integer quantum Hall effect, which is the subject of the next section.

1.7.2 Integer Quantum Hall Effect

As mentioned in the previous section, dissipation of the electron's energy occurs when electrons can scatter into an empty energy level. However, at integer

filling factors, the empty levels are at higher energies and thus cannot be reached when the sample is at low temperatures. This fact leads electron transport without dissipation in the energy and therefore to a vanishing of ρ_{xx} [12, 13].

The zeros of ρ_{xx} correspond to the plateaus in a Hall resistance trace. The value of the Hall resistance in terms of the filling factor is given by:

$$R_H = \rho_{xy} = \frac{B}{Ne} = \frac{hD}{Ne^2} = \frac{h}{e^2\nu} \tag{1.66}$$

Clearly, R_H is independent of magnetic field for integer filling factors and just depends on the fundamental constants indicated in Equation (1.66). For example,

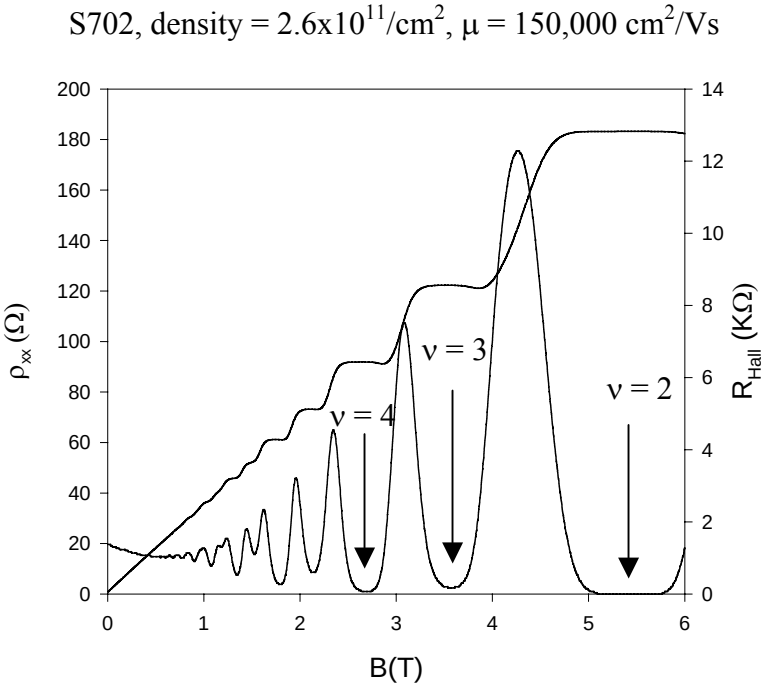

Figure 1.6: Plot of the Hall resistance and ρ_{xx} as a function of B at 4.2 K for s702. Notice the plateaus in the Hall resistances and how these correspond to the dips in the Shubnikov-de Haas trace.

the Hall resistance is ≈ 25.8 KΩ for $\nu = 1$. A trace of both R_H and ρ_{xx} for sample s702 at a temperature of 4.2 K is given in Figure 1.6 showing the discussed plateaus.

In order to understand the plateaus in the Hall resistance one should revisit the defects and impurities picture mentioned above. Recall that the electrons trapped by impurities or defects cannot contribute to the flow of current through the sample. However, small changes of the magnetic field away from the specific magnetic field at an integer filling factor will change the number of trapped electrons, but will not change the number of filled extended states. This implies no change in R_H (i.e. – a plateau in the R_H trace).

The integer quantum Hall effect is a very useful tool for characterizing the samples used in this study as well as studying fundamental physics. In a Shubnikov-de Haas (SdH) trace the minima in the ρ_{xx} correspond to integer filling factors. This fact, combined with Equation (1.65), can be used to determine the electron density of the samples. Also, in the Van der Pauw geometry (see Chapter 2), the average of ρ_{xx} at $B = 0$ can be used, again in conjunction with Equation (1.65) to evaluate the resistivity and then, in turn, the mobility of the samples. In addition, the Hall traces can also be used to determine the density of the samples. This is because the slope of the Hall trace at low magnetic fields is inversely proportional to the density.

1.7.3 Technical Aside – Input Parameters for Landau Level Calculation

As a technical aside, a program written in C++ is used to perform the Landau Level calculation discussed above. When this program is run, various input parameters are required by the user. These parameters are as follows:

Output file name

Well width in Angstroms

Al concentration

Starting magnetic field

Number of data points for field

Interval for field

Landau Level index

The *output file name* is the file under which the results of the calculation will be saved. After the calculation is completed, this file will be located in the C:\BCC\BIN\ directory. The *well width in Angstroms* and *Al concentration* are the width of the quantum well and aluminum concentration in the barrier of the sample for which the calculation is being performed. *Starting magnetic field* is the magnetic field value at which the calculation will begin, typically chosen to be zero Tesla. *Number of data points for field* is the number of individual data point for which the calculation is repeated, typically chosen to be between 100 and 150. *Interval for field* is the spacing in magnetic field between data points, usually chosen to be 0.25 Tesla. By choosing the above two values, the Landau level

calculation will extend to between 25.0 Tesla and 37.5 Tesla. And finally, *Landau level index* is the Landau level index for the calculation, typically zero, one or two.

In addition to the input parameters discussed above, there are also two values within the body of the program that one could desire to alter. Those are the momentum matrix element and the sample tilt angle. The momentum matrix element is defined on line 17 of the program:

Define p sqrt(11.3*cf/m0)

The value of the matrix element is highlighted in red above and was kept at a value of 11.3 in all the calculations of this study. The sample tilt angle is found in line 88 of the program:

kt = sqrt((2.0*lan+1.0)*cf*bf*1.0/hb)

The highlighted term in the above equation represents the cos θ term of the sample tilt angle. This value is, of course, changed on a sample by sample basis.

Chapter 2

Sample Preparation and Experimental Techniques

The purpose of this chapter is to discuss the InSb quantum well structure, as well as sample preparation, and some of the experimental techniques used to measure the transport, transmission, and photo-conductivity properties of the samples. These measurements can then be used to determine some of the fundamental properties of the InSb quantum wells.

2.1 The Quantum Well Structure

The samples used in these experiments are InSb quantum wells (QW) grown on GaAs (001) substrates using molecular beam epitaxy (MBE). The barrier material is $Al_xIn_{1-x}Sb$ where x is usually 0.09 or 0.15. Carrier concentration in the well is achieved with Si delta doping in the barrier layers [14, 15] and can be either symmetric or asymmetric in nature. This type of doping is advantageous because it leads to reduced scattering by ionized dopants, thus resulting in high electron mobility inside the well. A typical example of the cross-sectional layer structure for a symmetric sample (specifically sample s842) is given in Figure 2.1.

As stated above, by placing dopants on only one side of the well, one can achieve a QW with an asymmetric energy profile, while dopants on both sides of

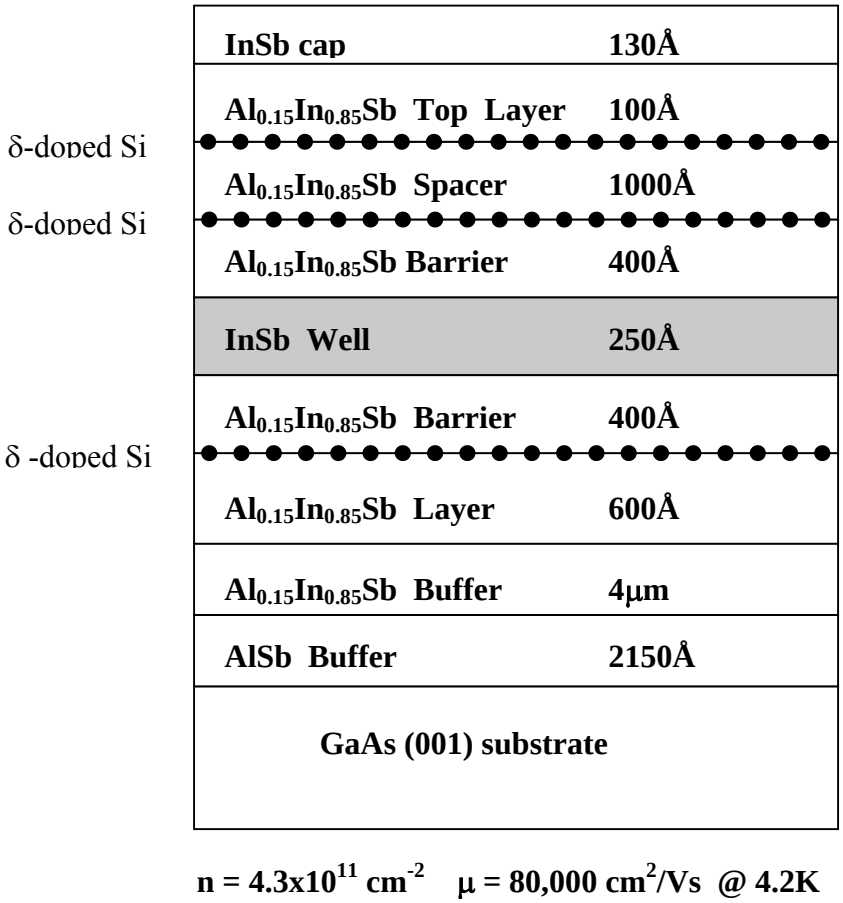

Figure 2.1: A typical layer structure for a triple δ-doped sample (specifically s842). In this case the dopants are both above and below the QW, resulting in a symmetric sample.

the well result in a symmetric profile. Also, an asymmetric profile can be achieved by growing the sample with different Al concentrations in the barriers on either side of the well. See Figure 2.2 for some schematic examples of these

different sample structures. Referring to Figure 2.2 we can see that for symmetric doping, the electrons in the well experience no net external field (Figure 2.2 (a)),

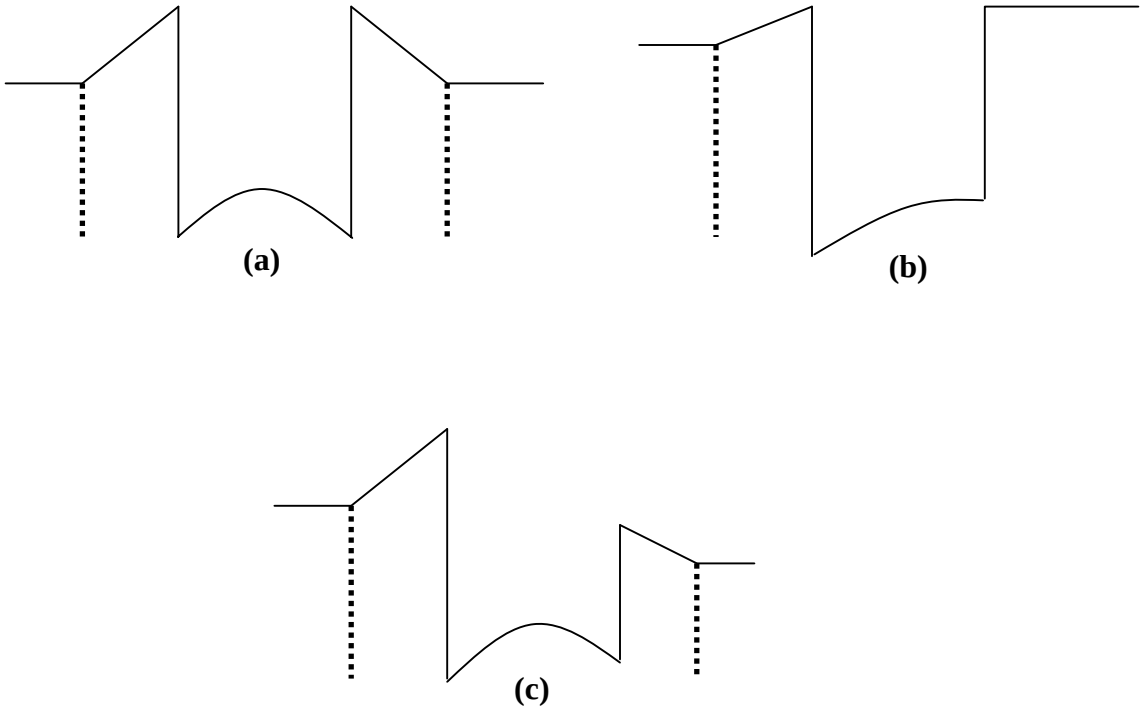

Figure 2.2: a) Symmetric structure resulting from doping on both sides of the QW. b) Asymmetric structure resulting from doping on only one side of the well. c) Asymmetric structure resulting from having different Al concentrations on the two sides of the well.

thus the electron probability distribution in the well will be symmetric. However, in samples with asymmetric doping, the electrons in the well experience a non-zero net external field (Figure 2.2 (b)). This moves the electron probability density towards the side of the well closest to the dopant layer. This asymmetry in the confining potential can be useful as it lifts the spin degeneracy of the electrons, even in the absence of an external magnetic field.

2.2 Sample Preparation

2.2.1 Wedging the Samples

The first step in preparing the samples for optical measurement is wedging. This is needed to minimize Fabry-Perot interference that can occur due to the parallel nature of the front and back surfaces of an un-wedged sample. Wedging begins by mounting the sample, face down (so the back of the sample gets material removed) on a piece of clean glass (usually a piece of microscope slide, cleaned with methanol) using white paraffin wax. The samples are mounted on either a 2^0 or 4^0 mounting block. This mounting block attaches to a South Bay Technology hand lapping fixture (model 155) by means of a threaded knob. Then, a small amount of Silicon Carbide powder (600 grit / 14.5 micron) is mixed with water on a piece of flat glass. The sample and fixture are then rubbed over this mixture for a few minutes in order to wedge the sample. Care must be taken when placing the fixture into the flat glass so as to not break the sample.

Finally, in order to remove the sample from the microscope slide piece, the mounting block with the sample still on it is heated on a hot plate. Any remaining white wax on the sample can be removed by placing the sample, in order and under a vent hood, in boiling trichloroethylene for 2 minutes, boiling acetone for 4 minutes, and finally boiling methanol for 4 minutes. The sample can then be dried using dry nitrogen gas.

2.2.2 Ohmic Contacts

In order to measure the electron density and photo-conductivity effects of our samples, ohmic contacts need to be made on the samples. First, after the samples are removed from the MBE chamber, they are cleaved into typically 5 mm square pieces (sometimes as small as 2 mm x 3 mm, depending on what is needed). Then, after wedging (if optical measurements are planned) ohmic contacts are prepared on the 4 corners of the sample by placing small indium spots in the corners using a soldering iron. The indium used is kept clean of contaminates by only being cut with a clean razor blade and the soldering iron used is only used for this purpose and cleaned on a regular basis.

Once the contact indium is on the surface of the sample, the sample needs to be annealed in order for this contact indium to diffuse into the sample and make good ohmic contact with the quantum well below. Therefore, the sample is then placed in the annealing station in the Thin Films Lab. While a flow of approximately 4 liters/min of forming gas (mixture of 80% N_2 and 20% H_2) is passing over the sample, the sample is heated to approximately 220^0 C for about 5 minutes. Note, depending on the sample structure (i.e. – well depth and layer structure) and the type of experiment being done, the annealing temperature and time can vary somewhat (example: 230^0 C for 7 minutes).

Once annealed, 99.99% gold wires are soldered onto the corner indium contacts. The other ends of the wires are then connected to the sample holder pins

when the sample is mounted for experimentation. The sample should have an appearance similar to Figure 2.3.

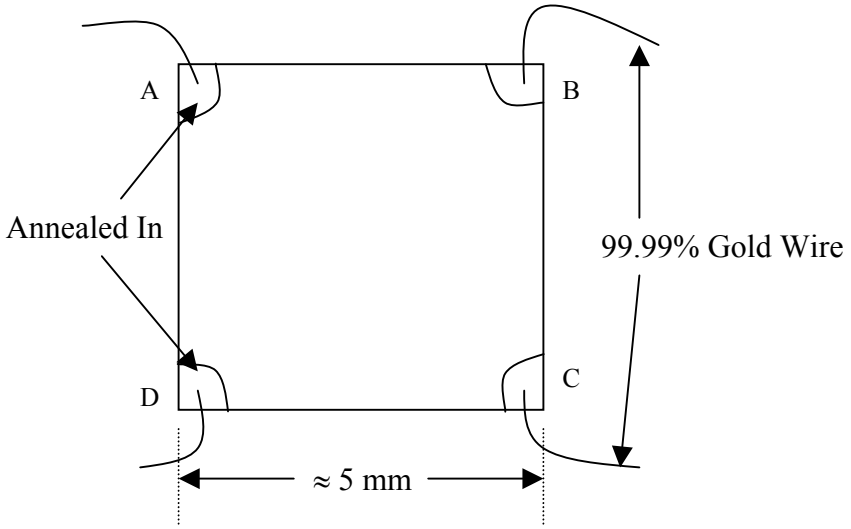

Figure 2.3: Sample contact and wiring setup

2.3 Hall Effect

2.3.1 Theory

Consider a conductor placed in a magnetic field as shown in Figure 2.4.

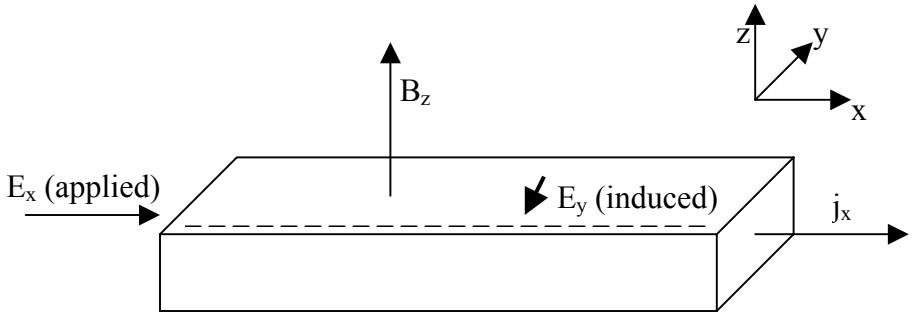

Figure 2.4: Hall setup. *n*-type carrier flow in the x-direction will get deflected by the B-field in the z-direction. Charge collects on the sides and creates a transverse electric field, E_y. A steady-state results when the repulsive force from E_y equals the deflection force of B_z.

When an electric field E_x is applied in the +x-direction a 2D current density j_x is induced in the same direction. The electrons will therefore flow in the –x-direction. However, due to the presence of the magnetic field B_z, these electrons will feel a Lorentz force:

$$\mathbf{F} = -e (\mathbf{v} \times \mathbf{B}) \tag{2.1}$$

where e is the electrons charge and v is the average electron velocity. If the direction of the current and magnetic field are those given in Figure 2.4, the flowing electrons will be deflected in the –y-direction. This will result in a net negative charge on one side of the bar. Thus, an additional electric field, E_y, is induced perpendicular to the original electric field and current density. In general, equation (2.1) becomes:

$$\mathbf{F} = -e (\mathbf{E} + \mathbf{v} \times \mathbf{B}) \tag{2.2}$$

Steady state is reached when enough charge accumulates on the side of the conductor so that the force on the electrons from E_y (in the +y-direction) is equal to the force from B_z (in the –y-direction).

Knowing (or, rather, in our case, measuring) the quantities discussed above allows one to determine the Hall coefficient for the sample:

$$R_H = \frac{E_y}{j_x B} \tag{2.3}$$

With the Hall resistance known, the carrier concentration can be determined by using:

$$R_H = -\frac{1}{ne} \tag{2.4}$$

where n is the 2D density.

2.3.2 Van der Pauw Technique

The above discussion assumes that the sample is in what is known as "Hall bar geometry" [16], i.e. – the sample is long and thin resulting in the x and y components of the voltage and current being decoupled. However, in practice, the simpler van der Pauw [17, 18] geometry tends to be more convenient. An example of this geometry can be seen by referring back to Figure 2.3. As can be seen in the figure, in this technique the contacts are symmetric on the four corners of a square sample. The 2D resistivity of the material is given by:

$$\rho = \frac{\pi}{\ln 2}\frac{(R_{AB,CD} + R_{BC,DA})}{2} f(\frac{R_{AB,CD}}{R_{BC,DA}}) \tag{2.5}$$

where $R_{AB,CD}$ is the potential difference, $V_D - V_C$, divided by the current passed from contact A to contact B, with no magnetic field. $R_{BC,DA}$ is similarly defined. If the sample is a homogenous square sample, with contacts on the four corners, then $R_{AB,CD} = R_{BC,DA}$, and the function *f* in this model is equal to one. The density can then be obtained from the slope of the Hall resistance vs. magnetic field, and the mobility is given by:

$$\mu_H = \frac{1}{\rho en} \tag{2.6}$$

where $n = N / d$ is the samples 2-D density.

2.4 Magneto-Optics Measurments

2.4.1 Experimental Setup

The experimental setup for the magneto-optical experiments conducted at the University of Oklahoma used in this work is shown in Figure 2.5.

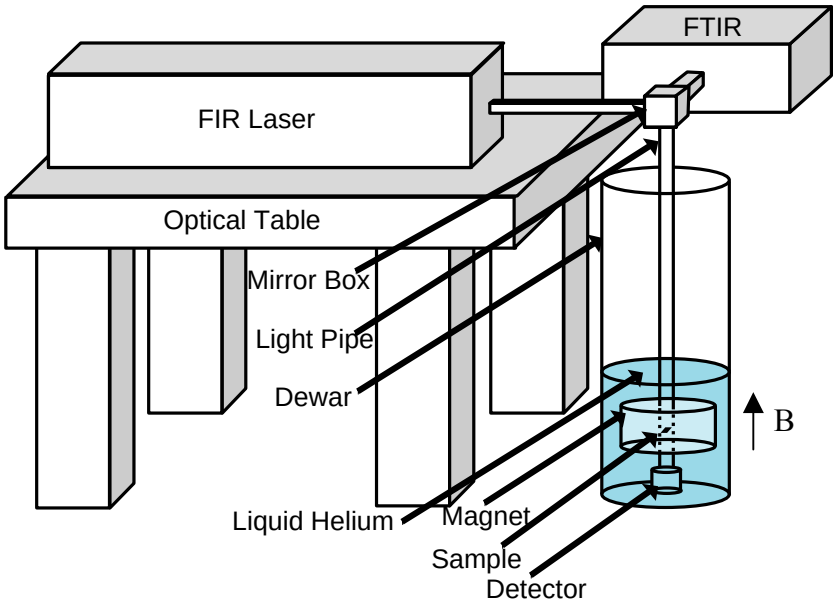

Figure 2.5: Schematic of the magneto-optical experimental setup. Note, the setup is such that the FIR laser or the FTIR can be used as the source of the incident light.

This setup begins with an Edinburgh FIR laser model 100 which is pumped by a CO_2 laser. This laser is capable of providing far infrared (FIR) radiation in the 40 – 1200 μm wavelength range. This radiation is directed via a mirror box and light pipe onto the sample that sits at the center of a superconducting magnet. The radiation that gets transmitted through the sample is then detected by either a Ge:Ga doped photoconductor or a bolometer detector. The sample, magnet, and

the detector are all held at 4.2 K by being immersed in liquid helium at the bottom of a vacuum jacketed dewar. Also, a small portion of the FIR laser beam is monitored as a reference signal using a polyethylene beam splitter (not shown in the figure) by a room temperature pyroelectric detector.

2.4.2 The Superconducting Magnet

As indicated in the figure, the magnet used in this setup is located inside a cryogenic dewar. It is a Cryomagnetics Inc. superconducting NiTb magnet capable of providing a magnetic field of 7.7 Tesla, although in our experiments we rarely went above approximately 6 Tesla. A programmer, connected to the magnet power supply, controls the maximum field, the sweep direction, and the sweep rate. Voltage across a shunt on the back of the power supply is used to measure the strength of the magnetic field. The field to current ratio for this setup is 969.3 Gauss/Ampere.

In order to properly operate our magnet, the following considerations should be taken into account:

(1) The power supply to the magnet should only be turned off when the magnetic field is zero.

(2) Using a switch box located in the far infrared lab, one can change the direction of the magnetic field. This should only be done when the magnet power supply is OFF.

(3) The magnetic field sweep rate should NOT exceed 0.1 Tesla per second, otherwise quenching of the magnet could occur. The sweep rate can be changed using a sensitive potentiometer, which allows a sweep rate as low as 0.01 Amps per second.

(4) At low sweep rates, typically less than 0.05 Amp/sec, the programmer does NOT change the sweep direction. In order to overcome this, one can first set the sweep rate to a larger value (but still not greater than 0.1 Tesla/sec) and then adjust it to a lower rate once the sweep direction has changed as desired.

(5) In order to operate the magnet at high field, a sufficient amount of liquid Helium is required (typically a liquid helium level of 5 cm, see the section on system cool down), otherwise, quenching of the magnet can occur.

(6) The magnet leads are vapor cooled. Therefore, the holes on top of the leads should not be covered during normal magnet operation.

(7) Before the magnet is cooled down, it should be dried using dry nitrogen gas.

(8) The magnet leads can carry very high current. Therefore, good electrical isolation is required and the leads should NOT be touched unless the magnet power supply is off.

2.4.3 Cooling Down the System

The first step in cooling down the system to perform a low temperature experiment is to be sure that the magnet is dry using the nitrogen gas mentioned above. This is important to prevent any water ice from forming at the base of the setup that could later interfere with the insertion of the vacuum can / light pipe assembly. Also, it is a good idea to pump on the cryogenic dewar to at least 10^{-5} Torr before continuing. Note however, that the dewar does not need to be pumped on before every experiment. Pumping on the dewar overnight approximately once a month with a good diffusion pump is usually sufficient to maintain the necessary low pressure.

Once the magnet is dry and the dewar pressure is sufficiently low then the magnet can be pre-cooled by filling the dewar with approximately 30 liters of liquid nitrogen the night before the experiment. This transfer of liquid nitrogen should occur at a slow rate so as not to damage the magnet. The temperature of the magnet can be monitored by connecting a standard ohm meter to the magnet leads in order to measure the resistance of the magnet. The magnet has a resistance of about 600 Ω at room temperature and 70 – 77 Ω at 77 K.

Once the magnet has been pre-cooled, the liquid nitrogen should be removed by pressurizing the dewar with helium gas. Note that this pressure should not exceed 2 PSI. As this is being done, the resistance of the magnet should again be monitored. As the liquid nitrogen is removed, the magnet will

warm up slightly. Thus, when the liquid nitrogen is full expunged from the dewar the magnet should have a resistance of about 110 – 120 Ω.

At this point, the system is ready to be filled with liquid helium. The initial transfer of liquid helium into our system usually requires 30 – 35 liters in order to achieve a liquid helium level of 20 cm, as measured from the bottom of the magnet. After this initial transfer, the same level can usually be obtained with approximately 15 – 20 liters of liquid helium. Again, the resistance of the magnet should be monitored during the initial liquid helium transfer. The magnet resistance will, of course, drop to zero as it becomes superconducting. However, until that time, there will not be a significant increase in the liquid helium level. Once the magnet becomes superconducting, the helium level should rise noticeably faster. Also, again, so as to not damage the magnet, the initial liquid helium transfer should be conducted slowly. An initial transfer of one hour is not uncommon. However, after that, subsequent transfers can occur much quicker, sometimes only 15-20 minutes depending on the amount of addition liquid helium needed. But keep in mind, the general rule of thumb for all transfers is: The Slower the Better.

The final step in cooling the system is to prepare the vacuum can / light-pipe assembly. This assembly requires pre-cooling as well. First, the vacuum can should be pumped on with a diffusion pump to at least 10^{-4} Torr. Then, a small amount of helium exchange gas is introduced into the can. Next, the assembly is

immersed in liquid nitrogen for at least 20 minutes. Once this is achieved, the assembly can be removed from the liquid nitrogen and placed inside the liquid helium filled magnet dewar and the experiment can proceed.

2.4.4 Warming Up the System

The first step to warming up the system after completing an experimental run is to remove the vacuum can / light-pipe assembly. The procedure to complete the assembly warm up will be addressed shortly. For the magnet, two methods can be employed. The simplest method is simply to allow the remaining liquid helium in the magnet dewar to boil off and permit the magnet to warm up on its own. This method is attractive if there is no rush to use the setup again. If, however, a faster warm up is required, dry nitrogen gas can be circulated through the dewar, but only after the magnet has reached a temperature above 77 K (or approximately 100 Ω magnet resistance). Waiting until a reading of 100 Ω will prevent any nitrogen ice from forming at the base of the dewar.

The procedure for warming up the vacuum can / light pipe assembly involves using a heat gun on the assembly to expedite the warm up. Note, caution must be taken to avoid an excessive amount of hot air near the indium seal at the base of the vacuum can between the vacuum can and the gold colored detector casing. Also, recall that a small amount of nitrogen transfer gas was added to the vacuum can before pre-cooling. This nitrogen gas should be pumped out of the

assembly using a mechanical pump when the assembly is about half-way warmed up (i.e. – when the heat gun has removed about half the water condensation that forms when the assembly is removed from the magnet dewar).

2.4.5 FTIR Principles

In the Fourier transform spectrometer, the radiation from a broad-band light source is divided into two parts by a beam splitter. After reflection from a fixed and movable mirror, respectively, the two partial waves are combined by the same beam splitter and focused on a detector. There they interfere and yield the total intensity. For different positions of the movable mirror the two partial waves get different phase shifts with respect to each other. Therefore, on the detector the radiation field is superimposed with a time-delay copy of itself. Refer to Figure 2.6. Hence, what is basically measured when the detector signal is recorded while the mirror moves is the autocorrelation function of the radiation field. This autocorrelation function is called the interferogram in FTIR spectroscopy and it is the Fourier transform of this interferogram that is the desired power spectrum in the frequency domain.

Let us consider these ideas in more detail. First, if *monochromatic* light of wavenumber k and amplitude A is incident, the beam splitter will send light of amplitude $A\sqrt{2}$ along each arm. This light will then be reflected at the two mirrors and as a result of the different path lengths traveled in the two arms, will

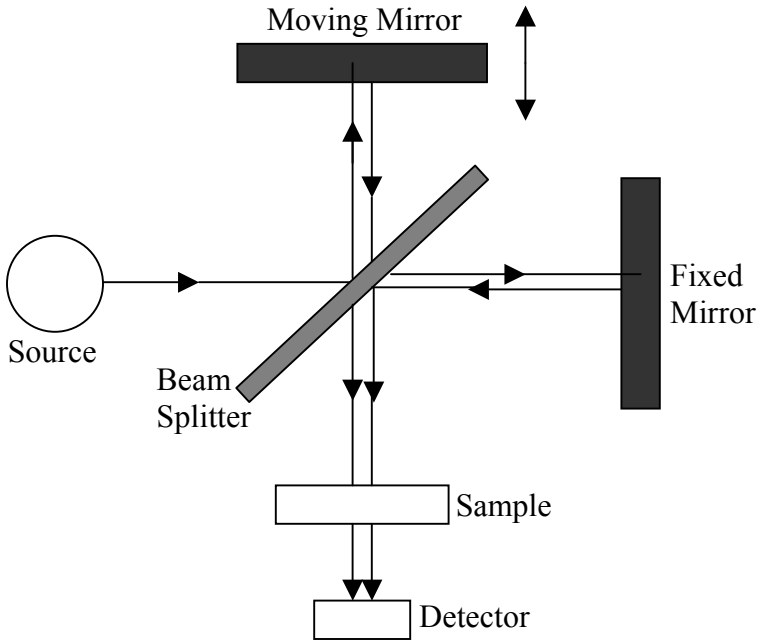

Figure 2.6: Scheme of a Fourier transform spectrometer. Light waves emitted from the light source are divided by the beam splitter. One fraction is reflected by the fixed mirror, the other by the movable mirror. The partial waves interfere on the detector, where the total intensity is measured. The sample is usually placed between the interferometer and the detector.

recombine with different phases at the beam splitter. For convenience, consider a moment when the phase is zero at the point of division. If this is the case then if the two paths have lengths d_1 and d_2, then the phases will be $2\pi k 2d_1$ and $2\pi k 2d_2$. Then the two amplitudes, whom are both complex when the phases are included, are added and the transmitted amplitude is given by:

$$A_T = (A/2)[e^{2\pi i k d_1} + e^{2\pi i k d_2}] \tag{2.7}$$

The transmitted intensity is then:

$$I_T = A_T A_T^* = (A^2/4)[e^{2\pi i k d_1} + e^{2\pi i k d_2}][e^{-2\pi i k d_1} + e^{-2\pi i k d_2}] \tag{2.8}$$

Writing the path difference of $2(d_1-d_2)$ as Δ and multiplying, this becomes:

$$I_T = (I/2)[1+\cos(2\pi k\Delta)] \tag{2.9}$$

where $I = AA^*$ is the input intensity.

If, instead of a monocromatic source is used, a broad band spectrum source is employed, then the intensity at wavenumber k will be given by a I(k). In other words, the power entering the interferometer between wavenumbers k and k+dk will be I(k)dk. Therefore, the emerging intensity will be given by:

$$dJ(\Delta) = \frac{I(k)}{2}[1+\cos(2\pi k\Delta)]dk \tag{2.10}$$

and the integral of this over the entire spectrum is:

$$J(\Delta) = \int_{k=0}^{\infty} \frac{I(k)}{2}dk + \int_{k=0}^{\infty} \frac{I(k)}{2}\cos(2\pi k\Delta)dk \tag{2.11}$$

The first integral in the above expression is half the total input intensity, I. Thus, it is often more convenient to write $K(\Delta) = 2J(\Delta) - I/2$, so that:

$$K(\Delta) \leftrightarrow I(k) \tag{2.12}$$

Thus, if the interferogram $J(\Delta)$ is recorded at suitable intervals of path difference, the spectral power density I(k) can be recovered by a Fourier Transform [19].

Figure 2.7 shows an example of a typical interferogram and its corresponding intensity spectrum. The maximum of the interferogram corresponds to equal distances of the two mirrors to the beam splitter which causes constructive interference of the two partial waves for all wavelengths. For this reason, the peak is sometimes called the "White Light Position" (WLP).

Outside this central structure the phase difference between the partial waves reflected at the two mirrors depends on the wavelength. For a broadband source

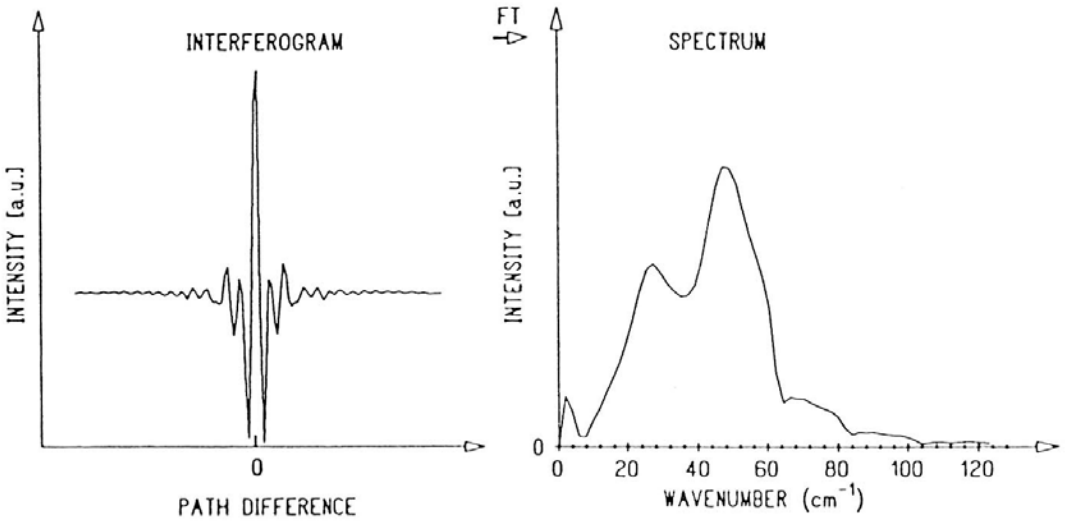

Figure 2.7: A typical interferogram obtained by a FTIR spectrometer and the corresponding spectrum.

their superposition to the interferogram contain less and less structures the further away one gets from the WLP. From the Fourier transformation it follows that a narrow WLP correlates to a broad frequency distribution, where as a broad interferogram correlates with a narrow, or "monochromatic", frequency distribution. The spectral resolution in an FTIR is determined by the inverse of the total path length of the movable mirror.

2.4.6 The Detectors

Two different types of optical detectors were used in the magneto-optical experiments discussed above. The first is a gallium doped germanium (*Ge : Ga*)

photo-conductor detector (serial number 2754) from Infrared Laboratories. This detector's operating temperature is in the range 1.5 – 4.2 K and has a spectral range of 40 μm – 120 μm. The output of this detector is connected to a pre-amplifier control box (model number LN6, serial number 2732). The box contains two internal 9 volt batteries to amplify the detector signal, as well as a single 15 volt battery to provide the bias. The lifetime on these batteries is approximately 100 hours. When the DC bias switch is turned on during normal operation, the bias is adjusted by the use of a 10-turn potentiometer built into the control box. The detector is connected to a 6 pin connector at the top of the vacuum can with two shielded cable containing Constantan wires. The pins on the connector of the amplifier box (labeled A through F) are connected to the Fisher connector (labeled by numbers) on the top of the vacuum can as follows:

Pin A → Bias (pin 6, green wire of the second cable)

Pin B → Drain (pin 5, black wire of the first cable)

Pin C → Gain (pin 10, white wire of first cable)

Pin D → Source 2 (pin 12, green wire of first cable)

Pin E → Source 1 (pin 4, red wire of first cable)

Pin F → Feedback (pin 8, white wire from second cable).

The second type of detector used in these experiments is a Si Bolometer (serial number 2851), also from Infrared Laboratories. For this detector the operating temperature is in the range 0.3 – 4.2 K and has a spectral range of 2 μm

– 3000 μm. Again, the output of this detector is connected to a pre-amplifier control box (model number LN6, serial number 623) and likewise, this box contains two internal 9 volt batteries to amplify the detector signal, and a single 15 volt battery to provide the bias. The main difference between the amplifier box for the photo-conductor and the bolometer comes from how the bias is adjusted. Rather then using a 10-turn potentiometer (essentially a knob on the side of the box) like the photo-conductor, the bolometer amplifier box utilized a toggle switch to select a gain of either 200 or 1000. Another difference between the two detector setups is the wiring codes. For the Bolometer the wiring code is as follows:

Pin A → Drain (pin 8, wire with red tape, note: no longer used)

Pin C → Load Resistor (pin 6, wire with orange tape)

Pin D → Source (pin 10, wire with black tape)

Pin E → Ground (pin 4, wire with blue tape)

Finally, a few words about the internal structure of both detectors should be mentioned as well as a guide as to how the detectors are mounted on their corresponding vacuum cans. The detector unit consists of a Winston Cone [20] and a cold amplifier (currently disabled) which is placed close to the detector. The detector unit is sealed to the vacuum can using Indium wire. Before making the Indium seal, the surface of the flange on the vacuum can as well as the flange on the detector should be cleaned using Methanol. A small amount of vacuum

grease is used on the Indium wire before putting it in the Indium grove. The eight 4 – 40 screws should be tightened in a symmetric star pattern in order to make the seal between the detector unit and the vacuum can. The assembly should then be check for any leaks using a leak detector.

Chapter 3

Cyclotron Resonance

Spin resolved cyclotron resonance was first observed in InAs quantum wells with AlSb barrier layers [21, 22]. The observations were explained by using a modified Pidgeon Brown bulk band structure model [23, 24, 25, 26] that takes into account non-parabolicity. Spin split cyclotron resonance due to many body effects has also been observed in GaAs-AlGaAs heterostructures [31, 32]. The purpose of this chapter is to discuss the spin-split cyclotron resonance experiments conducted for this work at the National High Magnetic Field Lab (NHMFL) in Tallahassee, Florida. The sample's layer structure as well as its energy profile will be reviewed. The experimental setup at NHMFL will be discussed as well. The fan diagram / Landau level plots will then be touched upon again, but derived in a less rigorous fashion than previously. Then, some representative data of both the cyclotron resonance data as well as intensities will be examined and an interpretation of the data will be looked at in light of the established theoretical backdrop. Finally, some concluding remarks will be made.

3.1 The Samples

As discussed in previous chapters, the samples used in these experiments are triple delta-doped, InSb quantum wells, with $Al_xIn_{1-x}Sb$ barrier material, grown on (001) GaAs substrates [33]. As a review, the layer structure for sample s499 is given in Figure 3.1. The majority of the data discussed in this chapter was gathered using this sample.

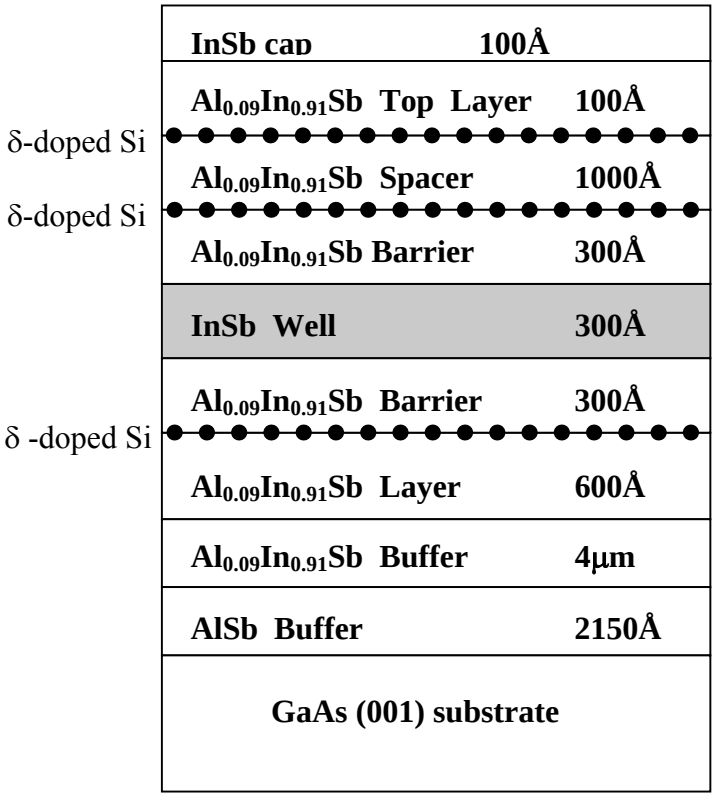

$n = 2.0 \times 10^{11}$ cm^{-2} μ = 130,000 cm^2/Vs @ 4.2K

Figure 3.1: Layer structure for sample s499

As shown in Figure 3.1, s499 is a symmetrically doped sample. Therefore it is expected that the energy profile will also be symmetric in nature. This

symmetric profile can be seen in Figure 3.2. At this point, one may wonder why InSb is chosen instead of some other, more common III-V semiconductor, such as GaAs or InAs. The answer to this question is three-fold. First, InSb has the smallest effective mass of all the III-V semiconductors. This fact can result in high electron mobilities.

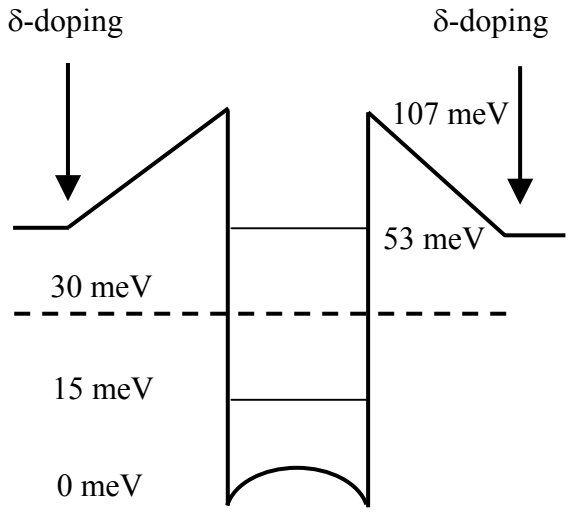

Figure 3.2: Energy profile for sample s499. The sample density is $n = 2.0x10^{11}$ cm^{-2} as measured by Shubnikov-de Haas.

Second, InSb also possess a very large g-factor, -51 in fact. This results in a large energy difference in the allowed states for electrons of different spins (either up or down) when the sample is placed in a magnetic field. This fact will be very important in the spin-split cyclotron resonance discussion to follow. And finally, although GaAs, InAs, and InSb all possess non-parabolic dispersion relations, the dispersion relation for InSb is the most non-parabolic of the three. This will also

play a key role in the experiments discussed in this chapter. These important characteristics are summarized in Table 3.1.

	m^*/m_o	g-factor	E(k)
GaAs	0.067	-0.5	Least non-parabolic
InAs	0.023	-15	More non-parabolic
InSb	0.014	-51	Most non-parabolic

Table 3.1: Characteristics of some III-V semiconductors. Notice that InSb is the most advantageous for spin-split cyclotron resonance experiments.

3.2 The Experimental Setup

The setup at the NHMFL is not unlike the setup used at The University of Oklahoma (OU), but there are some important differences. Like at OU, the sample sits inside a light pipe at the center of a superconducting magnet. However, at the NHMFL the magnet is much larger and stronger, with a maximum field of approximately 18 Tesla. The light transmitted through the sample is detected using a Far Infrared Labs Bolometer detector. The sample, magnet, and detector are again all held at 4.2 K by being immersed in a liquid helium filled dewar. The incident radiation is directed from the source to the sample again by means of a mirror and light pipe. However, instead of a CO_2 laser like at OU, at the NHMFL, the source of the incident radiation is a Bruker Fourier Transform Infrared Spectrometer (FTIR), model number 113V. The

FTIR can utilize either a glowbar or a Hg lamp as its source, depending on the spectral range needed. In addition to these two sources, there are two different

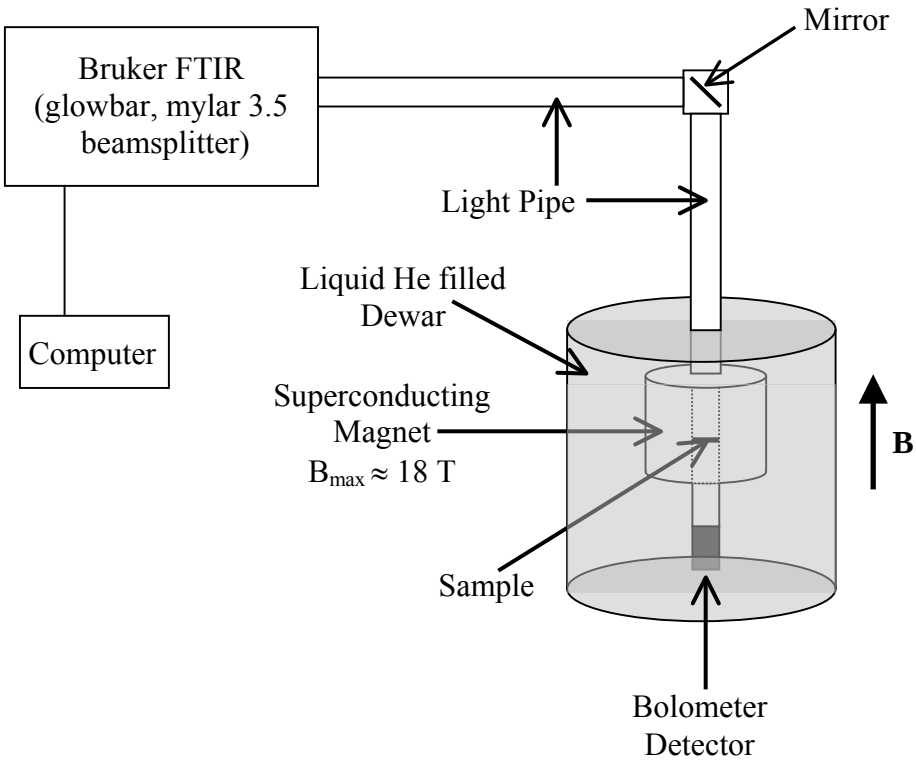

Figure 3.3: Experimental setup used at the National High Magnetic Field Laboratory in Tallahassee, Florida.

beamsplitters used, a mylar 3.5 and a mylar 12. These numbers refer to the thickness of mylar on the surface of the glass of the beamsplitter. Typically, a source / beamsplitter combination of Hg lamp/ mylar 12 is used to study features seen below 100 wavenumbers and a the combination of glowbar / mylar 3.5 is used to study features above 100 wavenumbers. Finally, the FTIR is connected to a computer, which records all the important data. Typically, background scans are taken for at least one hour and individual CR scans are taken for 15 to 20 min

and have a resolution of approximately 1 cm^{-1}. A schematic of the NHMFL setup is given in Figure 3.3.

3.3 Fan Diagram / Landau Level Plot

Referring to Figure 3.3, one will notice that the sample orientation inside the magnet is such that the direction of the magnetic field is perpendicular to (or very nearly so) the plane of the QW in the sample. This fact will cause the electrons in the well to move in closed cyclotron orbits with a classical cyclotron radius given by:

$$r = \frac{v_F}{\omega_c} = \frac{\hbar k_F}{m^*}\frac{m^*}{eB} \tag{3.1}$$

Next, quantum mechanics dictates that the energy states for these orbiting electrons must be quantizied, and will take on the form of simple harmonic oscillators:

$$E_n = \hbar\omega_c\left(n + \tfrac{1}{2}\right) \tag{3.2}$$

where $\omega_c = eB/m^*$ and n = 0, 1, 2, 3… This, however, is not the complete story. Recall that since the electrons possess spin, and the magnetic field direction determines a "preferred direction", the electron's spins will either be aligned (called "spin up") or anti-aligned ("spin down") with this preferred direction. This alignment (or anti-alignment) will also affect the energy of the electrons. Therefore, this additional effect needs to be included in order to get a more

complete picture of the total energy of the electrons in the well. This additional "spin energy" is included in equation (3.3):

$$E_n = \hbar\omega_c(n + \tfrac{1}{2}) \pm \tfrac{1}{2} g\mu_B B \qquad (3.3)$$

where B is the magnetic field, $\mu_B = eh/4\pi m$ and g is the electron g-factor discussed above. Equation (3.3) indicates that for a given magnetic field there are multiple allowed electron energies for the different values of n. In addition, for each value of n, the energy levels are further split by the spin energies of the electrons. The size of this splitting depends on the material's g-factor. Plotting E_n vs. B produces what is typically called a Landau level plot, also known as a fan diagram. An example is shown in Figure 3.4.

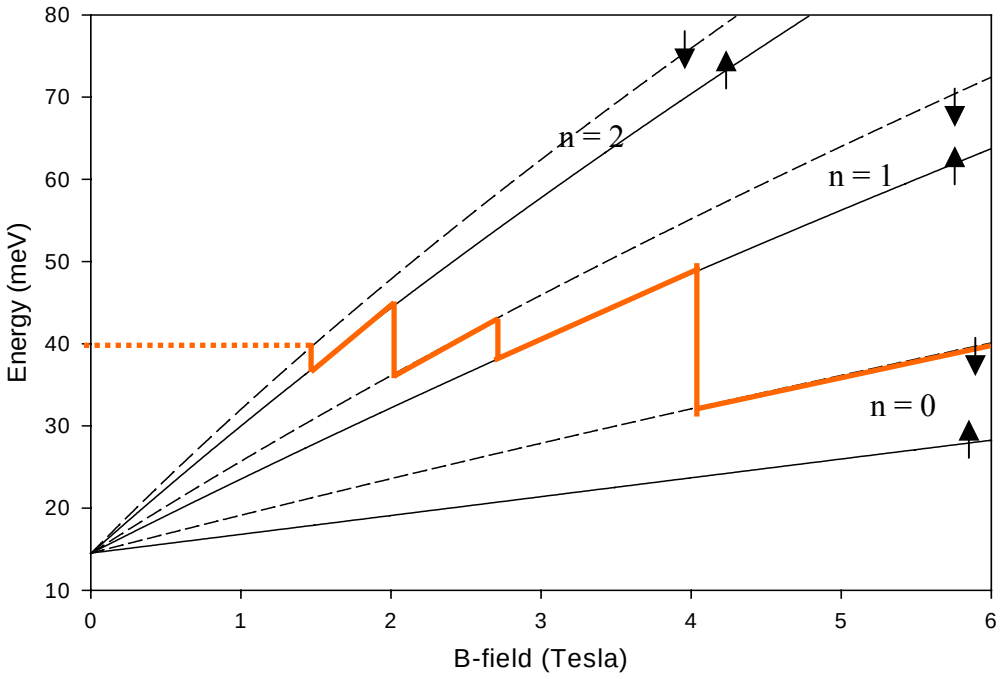

Figure 3.4: Example of a Landau Level Plot (Fan Diagram) for sample s499. The orange line indicates the Fermi Level of the electrons.

Taking a closer look at Figure 3.4, one notices that there are two "spin-split" energy levels for each value of n, one for spin-up and another for spin-down. Also included in this figure is the Fermi level for the electrons in the well. The Fermi level makes the "steps" between the allowed energy levels because the degeneracy of the energy levels increases linearly with increasing magnetic field. Therefore, as the magnetic field is increased, each level is capable of holding more electrons (see Equations (1.62) and (1.63)). The number of allowed states below each step is known as the "filling factor". For example, the step that occurs at approximately 4 Tesla would be filling factor 2. Likewise, the step at approximately 2.6 Tesla would be filling factor 3, etc.

Also, referring back to equation (3.3), one would expect that the energy levels on the fan diagram should be linear in nature and that the splitting due to spin should be the same for all values of n at a given magnetic field. However, looking closely at Figure 3.4 it can be seen that this is not the case. The reason for both is the non-parabolic nature of the dispersion relation for InSb. Recall that of all the III-V semiconductors, InSb has the most non-parabolic dispersion relation. And, although not thoroughly discussed in this chapter, this in fact leads to the effective mass m^* and the g-factor being dependent on energy (i.e. $m^*(E)$ and g(E), see Chapter 1). This causes the fan diagram to be non-linear in nature as shown in Figure 3.4. If one looks closely at the figure, one will noticed that each line, or Landau Level, has a slight curve to it, and that the gap due to the g-

factor (i.e. the splitting of different spin states for a given value of n) decreases as the energy increases. All these features of the fan diagram will be critically important in the data analysis to follow.

Now, with a more through understanding of the Landau level fan diagram, it is now more feasible to look at what this diagram predicts. Assume the sample is placed inside the light pipe and the light pipe is inside the magnet and everything is cooled down to 4.2 K. Also, assume the magnet is held at some steady B-field, say somewhere between 2.5 and 4 Tesla. Further, recall that the source of the incident radiation for this experiment is an FTIR, so the energy, or frequency, or wavenumber, of this incident radiation is what is varied as the B-field is held constant. Note, however, the B-field can be changed, of course, and additional frequency sweeps can be taken at the new B-field. But for now, assume the B-field is fixed. For a fixed B-field, there are fixed energy differences between the Landau Levels that contain electrons (i.e. the Landau levels at or below the orange line in Figure 3.4) and the Landau levels with empty, or partially empty states (i.e. the Landau levels at or above the orange line). These differences define allowed electron transitions in the well for that particular B-field. Thus, if the light incident on the sample is at the same energy as one of these fixed energy differences, then the light will be absorbed by the electrons in the well, resulting in the transmitted light intensity detected by the bolometer to decrease. Therefore, for a sweep of incident light frequency, a drop of transmitted

intensity will be seen for certain photon energies. This is the heart of cyclotron resonance. An example of some of these transitions is shown in Figure 3.5.

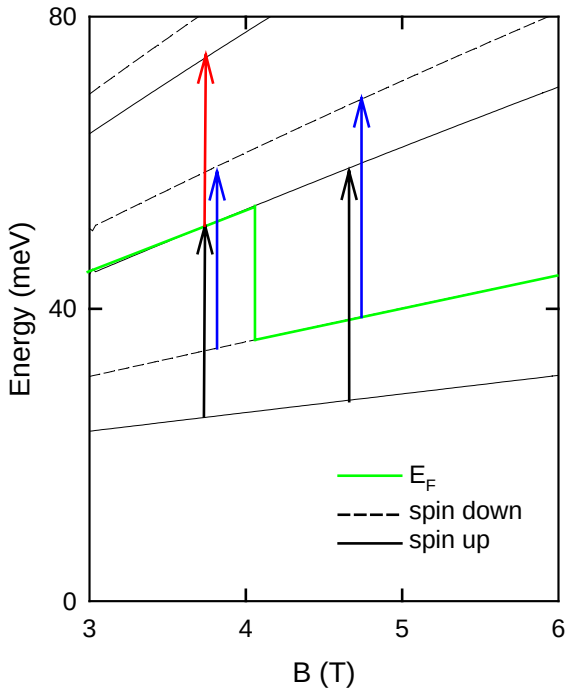

Figure 3.5: Example of some allowed electron transitions between Landau Levels. Note: For a given B-field there can be as many as three allowed transitions, all of different energies and intensities.

For a given magnetic field, various possible transitions occur. For example, notice that for B-fields where the filling factor is 2 or greater, three transitions are predicted. On the other hand, if the B-field is such that the filling factor is between 1 and 2, only 2 transitions are allowed. Also, due to the non-parabolicity considerations discussed above, the different transitions, even for the same B-field, should occur at different energies. In addition to different energies, the

transitions should also have different intensities. The reason for these different intensities is as follows. Recall that as the B-field is increased the degeneracy of the Landau levels also increases. This is what creates the "steps" in the Fermi level shown in both Figures 3.4 and 3.5. Therefore, only when exactly on top of a step is the Landau level **AT** the Fermi energy completely filled with electrons. Of course, all the Landau levels below the Fermi energy are completely filled and all those above the level are completely empty. So, if the B-field such that the Fermi level is "in-between" steps, the Landau Level at the Fermi energy is only partially filled with electrons. Therefore, this Landau Level is capable of both receiving electrons from a lower level, as well as sending electrons to a higher level through transitions.

So with a more complete understanding of "completely-filled, completely-empty, partially-filled, partially-empty" Landau levels, a reexamination of the intensity variations mentioned above is in order. Refer to the triple transition on the left of Figure 3.5. The red transition is from a partially filled state to a completely empty state. The blue transition is from a completely filled state to a completely empty state. And finally, the black transition is from a completely filled state to a partially empty state. Furthermore, since the transitions of interest are so close to the "step" to the right, they are only slightly above filling factor 2. This means that the Landau level that black transitions into and red transitions from has more empty states than filled states. Armed with all this information, a

prediction can now be made as to the relative intensities of these three transitions. Since blue is from completely full to completely empty, it should be the strongest transition of the three. Black should be the next strongest because it goes from completely full level to an "almost" empty level. Finally, red should be the weakest transition since it goes from a "not very full" level to a completely empty level.

3.4 The Experiment

Before considering a comparison of the experimental and predicted results, one needs to look at what type of data the experiment generates, and what needs to be done to this data in order to get it into a meaningful format. Recall that the result of this experiment is essentially a measure of the transmitted light intensity vs. wavenumber. An example of some raw data gathered using the glowbar source and the mylar 3.5 beamsplitter is given in Figure 3.6.

A few things should be noted when looking at the raw data. First, notice that the transmitted intensity varies greatly over the wavenumber range of interest. This is combination of the fact that the source does not transmit equal light intensities at all wavelengths, and that the polyethylene windows inside the FTIR and light pipe also do not transmit equally at all wavelengths. Second, notice the two "blind spots" that occur at approximately 180 to 190 cm^{-1} and 260 to 310 cm^{-1}. These are due to optical phonon absorption in the $Al_{0.09}In_{0.91}Sb$ buffer

layers and GaAs substrate respectively. For reference, the phonon frequencies for various semiconductors are given in Table 3.2.

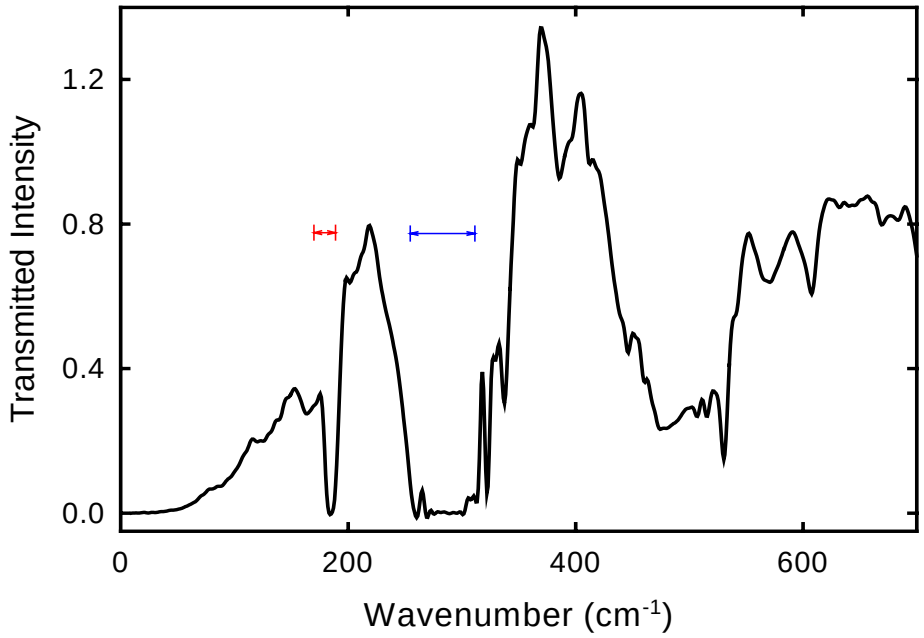

Figure 3.6: Background Transmitted Intensity for sample s499 at B = 0.
Note the following blind spots: ~180 to 190 cm^{-1}, $Al_{0.09}In_{0.91}Sb$ optical phonon absorption (buffer layer)
~260 to 310 cm^{-1}, GaAs optical phonon absorption (substrate)

More specifically, the absorption region at 180 cm^{-1} is due to the InSb-like phonons in the AlInSb buffer layer [42]. Also, AlSb-like phonons are present at approximately 320 cm^{-1}, however, the effect of these phonons is small since the concentration of Al in the buffer layer is small (typically 9 – 15 %). A more detailed picture of the relevant absorption regions is shown in Figure 3.7.

Semiconductor	ω_{LO}	ω_{TO}	ω_{LA}	ω_{TA}
Si	420 cm^{-1}	489 cm^{-1}	378 cm^{-1}	145 cm^{-1}
SiC	831 cm^{-1}	760 cm^{-1}	640 cm^{-1}	373 cm^{-1}
GaP	403 cm^{-1}	367 cm^{-1}	197 cm^{-1}	115 cm^{-1}
AlSb	344 cm^{-1}	323 cm^{-1}	232 cm^{-1}	64 cm^{-1}
GaAs	293 cm^{-1}	269 cm^{-1}	203 cm^{-1}	62 cm^{-1}
GaSb	205 cm^{-1}	216 cm^{-1}	153 cm^{-1}	45 cm^{-1}
InSb	196 cm^{-1}	184 cm^{-1}	127 cm^{-1}	37 cm^{-1}
ZnS	367 cm^{-1}	274 cm^{-1}	215 cm^{-1}	91 cm^{-1}
ZnSe	206 cm^{-1}	201 cm^{-1}	158 cm^{-1}	64 cm^{-1}

Table 3.2: Phonon frequencies for various semiconductors. [11, 34-41]

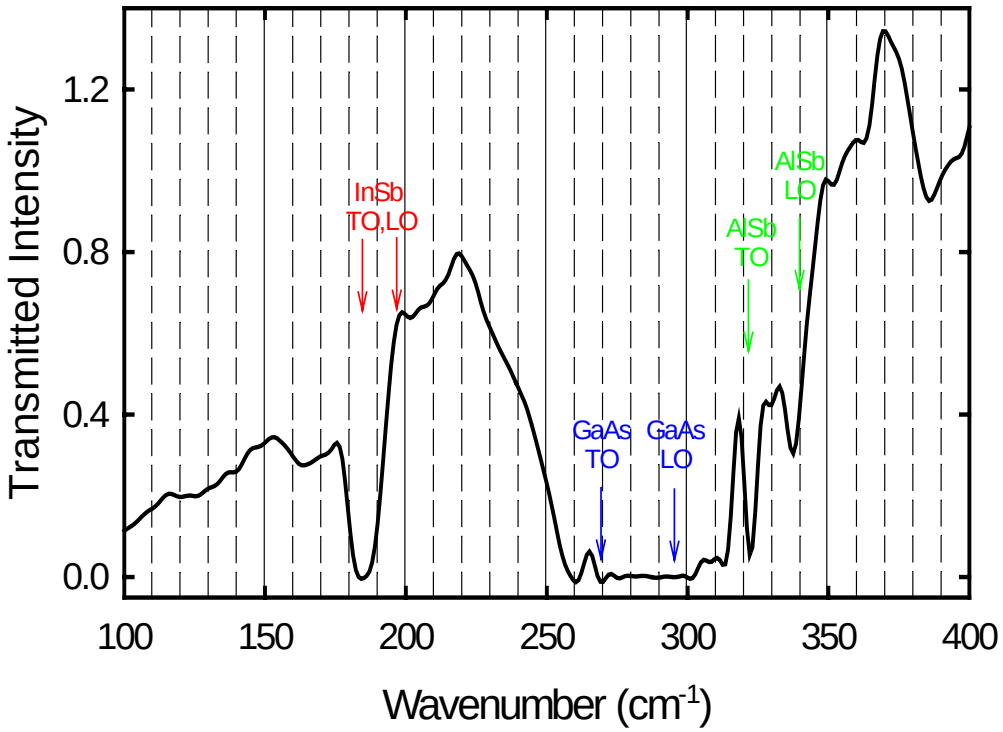

Figure 3.7: Close up of the raw data showing the relevant phonon absorption regions.

As can be seen in Figure 3.7, there are several regions of phonon absorption. Begin by considering the region between the TO and LO phonons of GaAs. This region is sometimes referred to as the reststrahlen region for GaAs. The reason for the low signal strength in this region is due to the fact that waves do not propagate in the frequency region for which the dielectric function is negative. In this case, the wavenumber is imaginary for real ω. Thus, incident electromagnetic waves of frequency $\omega_T < \omega < \omega_L$ will not propagate in the medium, but will be reflected at the boundary. This same effect is seen to a lesser extend between the LO and TO region of InSb in the figure.

Returning to Figure 3.6, it would be extremely difficult to spot a slight decrease in the transmitted intensity due to cyclotron resonance if one only looked at the raw data. In order to overcome this, what is done is to take a background scan, when the magnet is at zero B-field, and then divide the non-zero B-field cyclotron resonance scans by this "baseline" in order to see the cyclotron resonances more clearly. Figure 3.6, is, in fact, one of these background scans. Dividing the CR scans by the background produces "normalized scans" in which the drops in transmitted intensity due to the cyclotron resonances are much more pronounced. Several examples of these "normalized" CR scans are given in Figure 3.8.

There are several important things to notice in Figure 3.8. First, due to the normalization discussed above, the traces are relatively flat, except at the location

of a cyclotron resonance (marked by the colored arrows). The colors of these arrows correspond to the transitions shown in Figure 3.5. Also, notice the "noise" feature at approximately 180 cm^{-1}. This feature is due to the optical phonon absorption of the buffer layer seen in Figure 3.6. Second, notice that, for a given B-field, there is more than one cyclotron resonance. This is due to the "spin-splitting" as predicted by the Landau level plot. Third, observe that the position

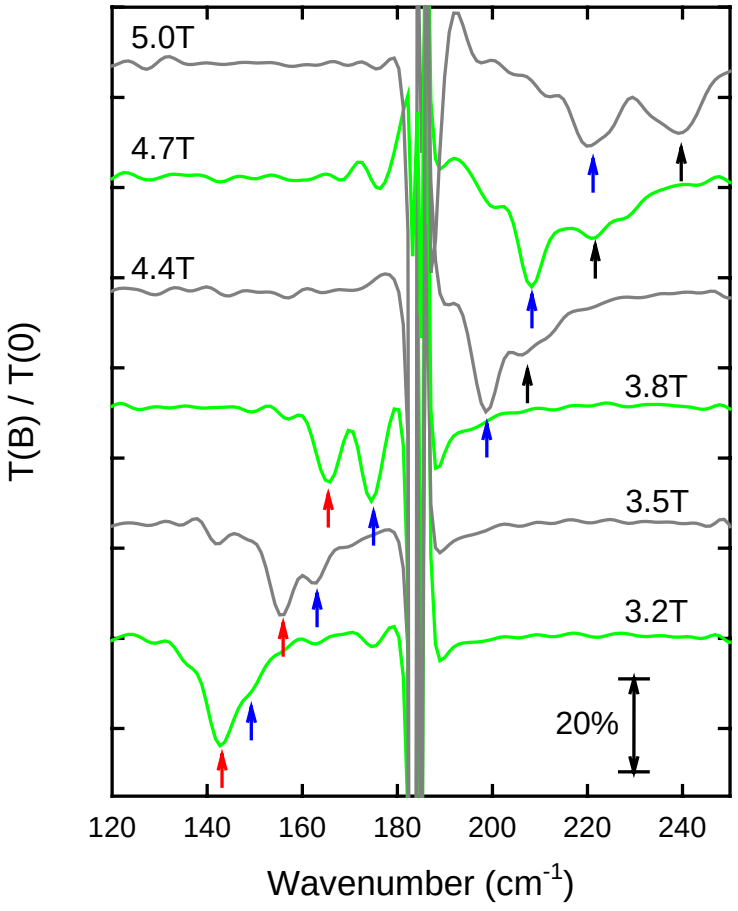

Figure 3.8: Example of several normalized CR scans. Notice that the absorption are spin-split and that both the position and intensity of the resonances change with changing B-field [43]. The scans are offset in the vertical direction for clarity.

of the cyclotron resonances move with changing B-field. The Landau level plot, again, predicts this. Finally, notice how the intensity of the different cyclotron resonances change as the B-field changes, again, predicted by the fan diagram. It should also be noted that in the initial interpretation of the data, the dips at 5.0 Tesla in the above figure were interpreted as only two absorptions, one for the blue transition and one for the black. However, as will be discussed in the next section and the following chapters, it is now believed that there are, in fact, 4 absorptions in this scan, two in the blue transition and two in the black, indicating the presence of an avoided level crossing. This will be expanded upon in the pages to follow.

Although the data gathered for this experiment can look quite clean, as Figure 3.8 indicates, there are several possible sources of noise that can complicate the interpretation of the data. The first, which has already been mentioned, are regions of the spectra where there is a strong absorption of the sample at all magnetic fields. For example, the optical phonon regions shown in Figure 3.6 exist at all magnetic fields and produce the type of noise seen in Figure 3.8 at approximately 180 cm^{-1}. There, of course, can also be electrical noise in the experimental setup. This type of noise, however, can be moved in wavenumber by changing the mirror speed on the inside of the FTIR. For our experiments this electrical noise was seen mainly at approximately 150 cm^{-1} and 525 cm^{-1} (see Figure 6.11). Also, when light passes through a sample with polished, plane-

parallel sides, multiple internal reflections can result. This interference phenomenon, known as Fabry-Perot interference, produces a wavelength-dependent intensity modulation, which is superimposed on the transmitted spectrum. In many cases, these oscillations partially or wholly obscure weak absorption features. This problem can be reduced by wedging the sample so its surfaces are no longer parallel. For our samples with a thickness of approximately 500 μm, this type of interference would produce periodic oscillations in the 5 – 10 cm^{-1} range.

3.5 Experimental Results

At this point hopefully a good understanding of the Landau Level diagram and what it predicts has been established, in addition to a good comprehension of the experimental data. Now a comparison between the actually results of the experiment and what is predicted is in order. First, let us consider the positions, or energies, of the cyclotron resonances. These positions are given in terms of the wavenumber at which the resonance occurs, and should vary as the B-field is changed. A plot of these resonance positions vs. B-field for sample s499 is shown in Figure 3.9.

A closer look should be taken at Figure 3.9. The first thing to notice is the colored lines black, blue and red. These lines correspond to the colored transition arrows in Figure 3.5. It is imperative to understand, however, that although these

colored lines look similar to the lines in the fan diagram (Figure 3.4), and are derived from that plot, they are, in fact, different. The colored lines in Figure 3.9 are the DIFFERENCES in the energies of the lines in Figure 3.4. Recall that it is these differences that determine the energies (or wavenumbers) of the allowed transitions between the different Landau levels, and it is these differences that the colored lines of Figure 3.9 represent. Second, the dots in Figure 3.9 represent the

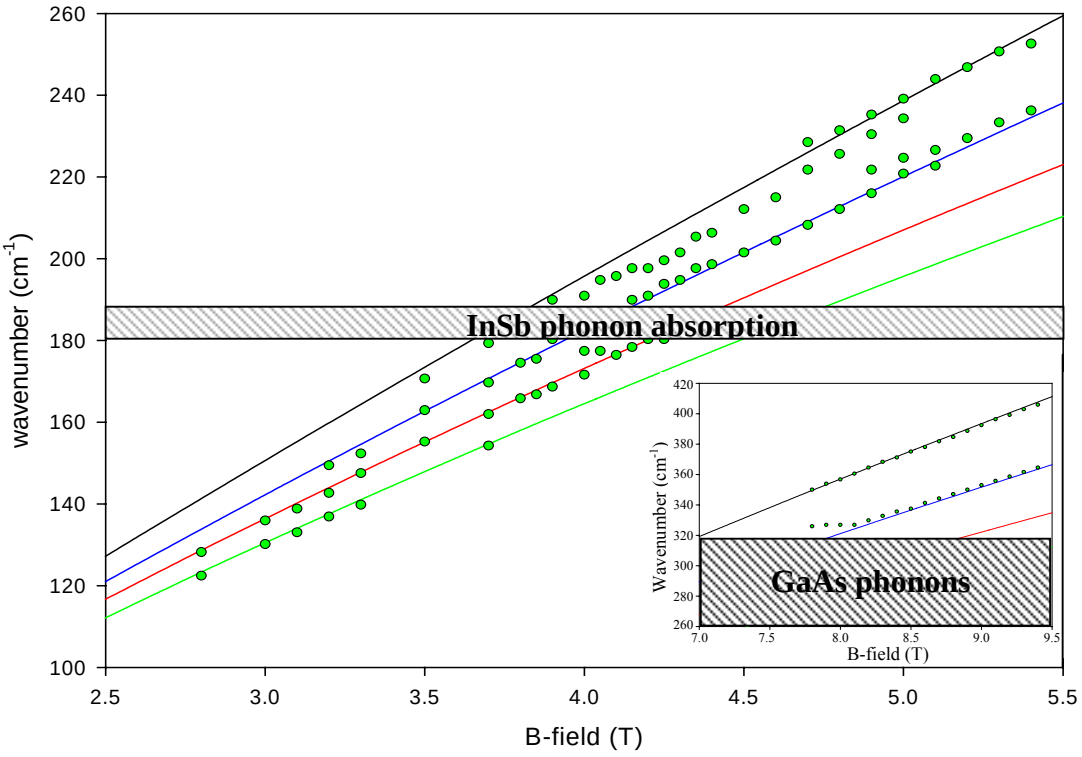

Figure 3.9: Plot of cyclotron resonance position vs. B-Field for sample s499 [43].

experimentally determined cyclotron resonance positions. Notice that these positions correspond quite well with the colored lines, indicating good agreement with our theory and experiment. Third, observe how the red transition disappears

below filling factor 2 (approximately 4.5 Tesla), again, as predicted by the theory. And finally, again a "blind spot" is seen in the data caused by the buffer layer and substrate phonon absorption. In addition, there are magneto-polaron effects at approximately 180 cm^{-1} and 320 cm^{-1}. A magneto-polaron is a coupling of the cyclotron resonance motion of the electrons to the phonon lattice vibrations of the host crystal. This coupling results in an avoided level crossing occurring in the cyclotron resonance trace near the point where the cyclotron resonance energy equals the InSb LO phonon energy. In addition, the AlSb magneto-polaron at approximately 316 cm^{-1} causes the avoided level crossing seen in the inset of Figure 3.9. Also shown in the figure is a green transition. Although not discussed previously, this green line corresponds to the n = 1 to the n = 2, spin down transition. Also in the figure is an apparent avoided level crossing in both the blue and black transitions at about 4.9 Tesla and 5.05 Tesla respectively. The possible origin of these avoided level crossings will be explored in the next few chapters.

Further evidence that our one electron theory can accurately predict the positions of the cyclotron resonances is shown in Figure 3.10. This figure is along the same vein as Figure 3.9, but for two additional samples, s702 and s716. Clearly, as the above figure shows, there is good agreement between our theory and experimental results. Also, any apparent discrepancy seen in the above figures

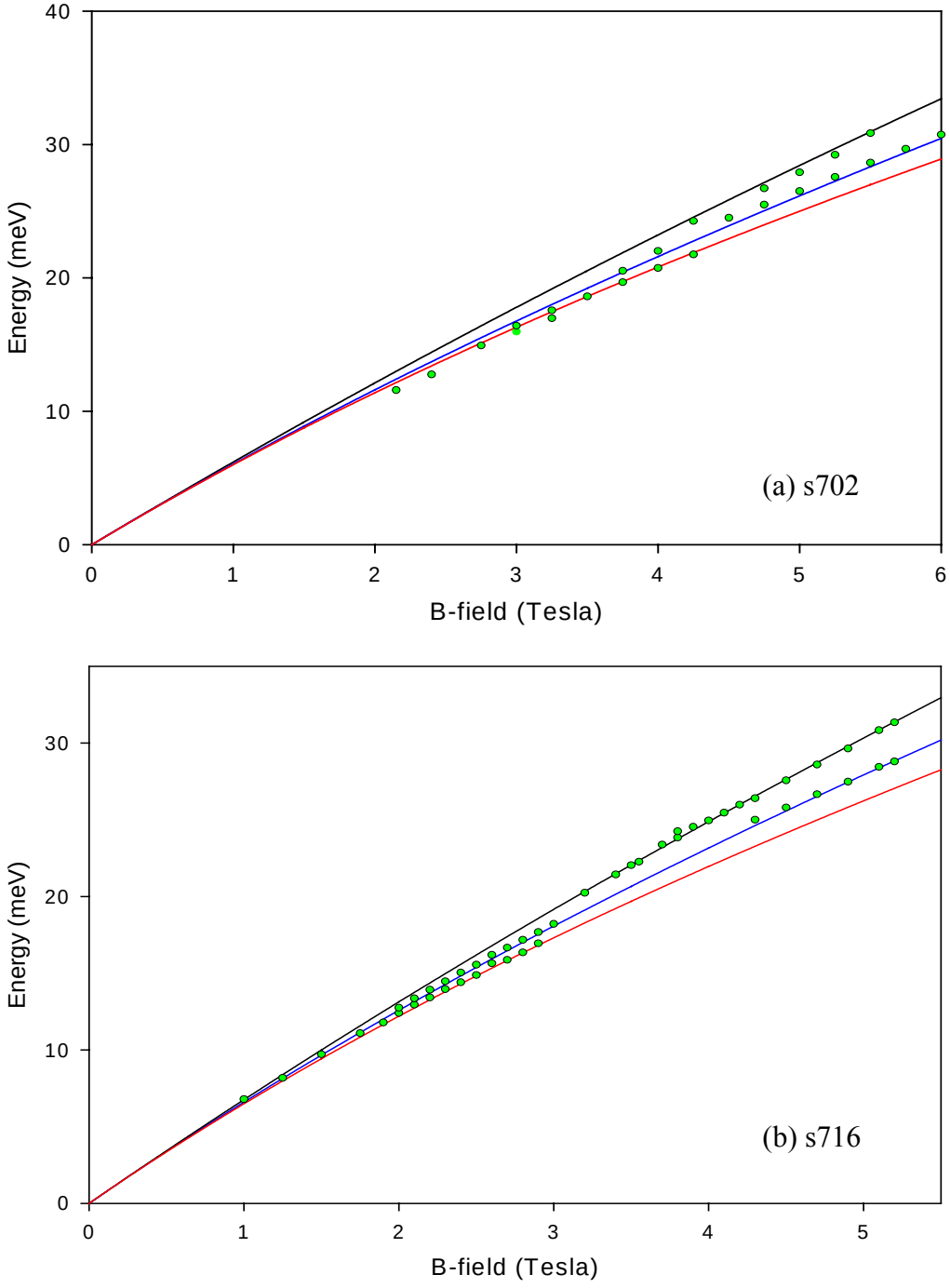

Figure 3.10: Additional evidence that our theory accurately predicts the position of the cyclotron resonances for (a) s702 and (b) s716.

is within the error bars of the measurement (anywhere from 2 cm^{-1} to 4 cm^{-1}, or 0.25 meV to 0.5 meV, depending on the sample).

A similar analysis to the one discussed above was done by Yang *et al.* [22] on InAs quantum wells. As in our study, Yang also saw clear splitting in the cyclotron resonance and the positions of these traces fit the theoretical predictions well. Their results are shown in Figure 3.11.

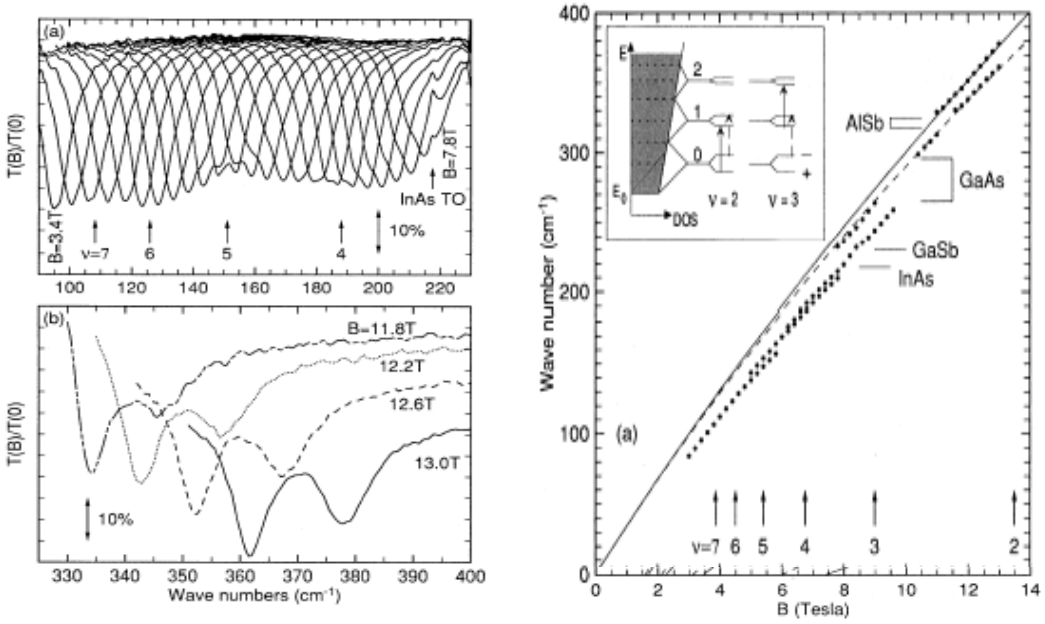

Figure 3.11: Clear CR splitting seen in InAs quantum wells [22]. Notice how, like our study, the positions of the CR traces agree well with experiment.

As a practical aside, the data for sample s702 merits further discussion. Unfortunately, of the three samples s499, s702, and s716, the data for s702 possess the most noise, as Figure 3.12 shows. Fabry-Perot oscillations with a period of approximately 5 cm^{-1} are evident. Because of this noise, it is often difficult to determine which dips in the normalized transmission spectra are due to

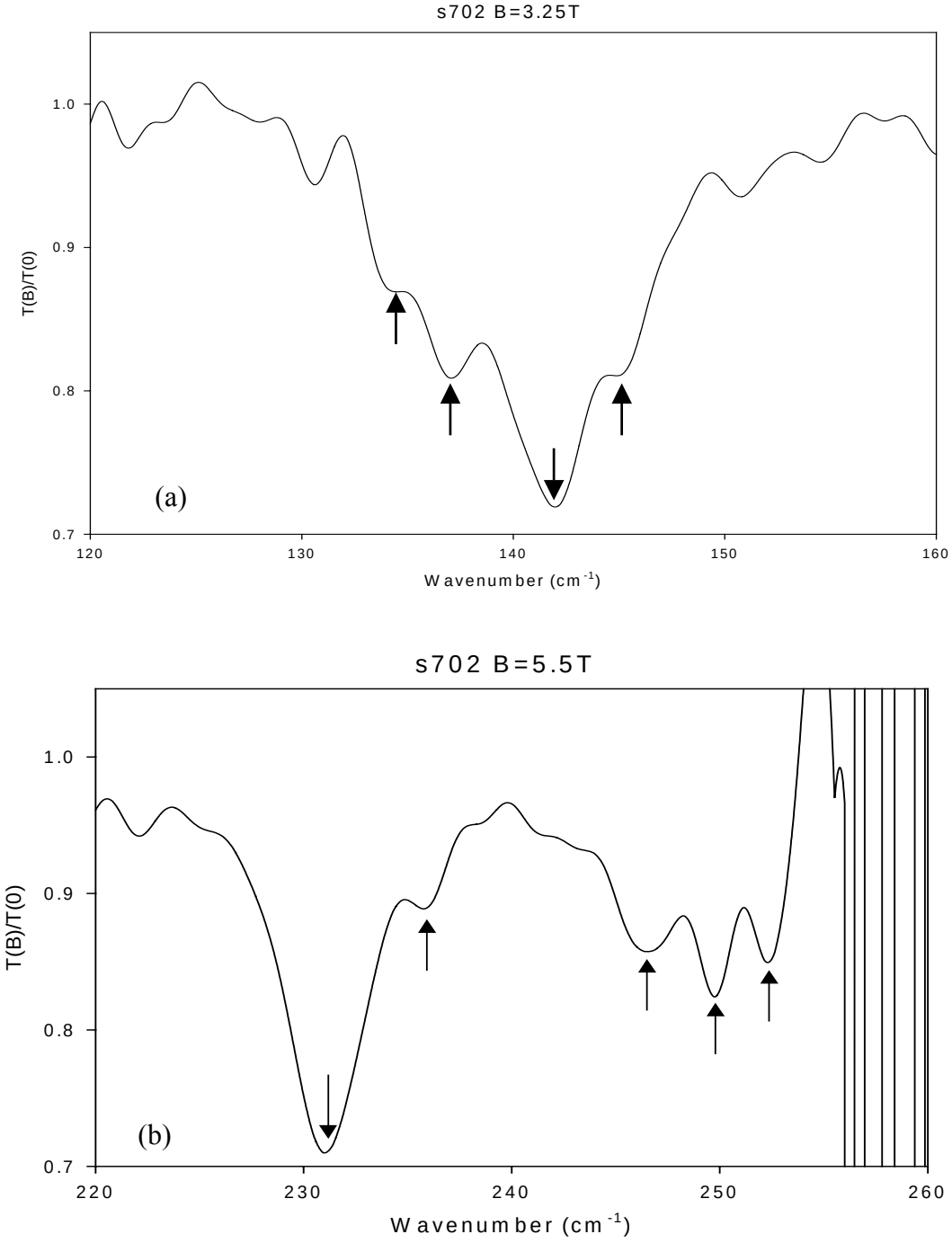

Figure 3.12: Normalized transmission spectra for sample s702 at magnetic fields of (a) 3.25T and (b) 5.5 T. Arrows indicate the positions of *possible* CR signals.

cyclotron resonance and which are due to the noise in the measurement. Indicated by the arrows in Figure 3.12 are all dips flagged as *possible* cyclotron resonance signals. If one plots the positions of these possible resonances vs. magnetic field along with the colored transition lines, Figure 3.13 is the result. Clearly, some of these potential resonances are real and others are simply noise, so how does one sort out which is which? Referring back to Figure 3.12, clearly several of these "possible" transitions are real, such as the second dip from the right at 3.25 Tesla and the far left dip at 5 Tesla. Also, dips that lie on the predicted transition lines would seem to be real as they move in wavenumber as the magnetic field is

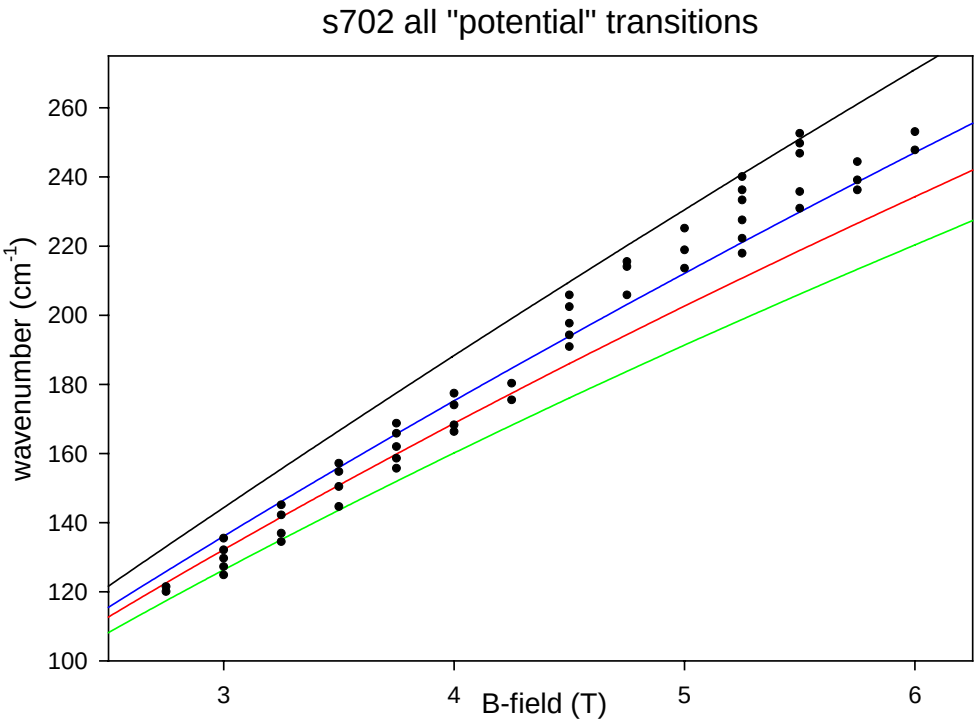

Figure 3.13: Graph of all *potential* resonances (dots) for sample s702 along with the predicted resonances (colored lines).

varied as predicted by theory. The other dips, on the other hand, could be due simply to noise, or a result of possible avoided level crossings as was seen in sample s499 (refer to Figure 3.9). However, as will be discussed further in chapter 6, it has been determined that we do not see any avoided level crossings for sample s702 at these magnetic fields. So these other dips are simply noise in the measurement. With this in mind, a revised figure showing the positions of the true cyclotron resonances for sample s702, along with the predicted positions is given in Figure 3.14.

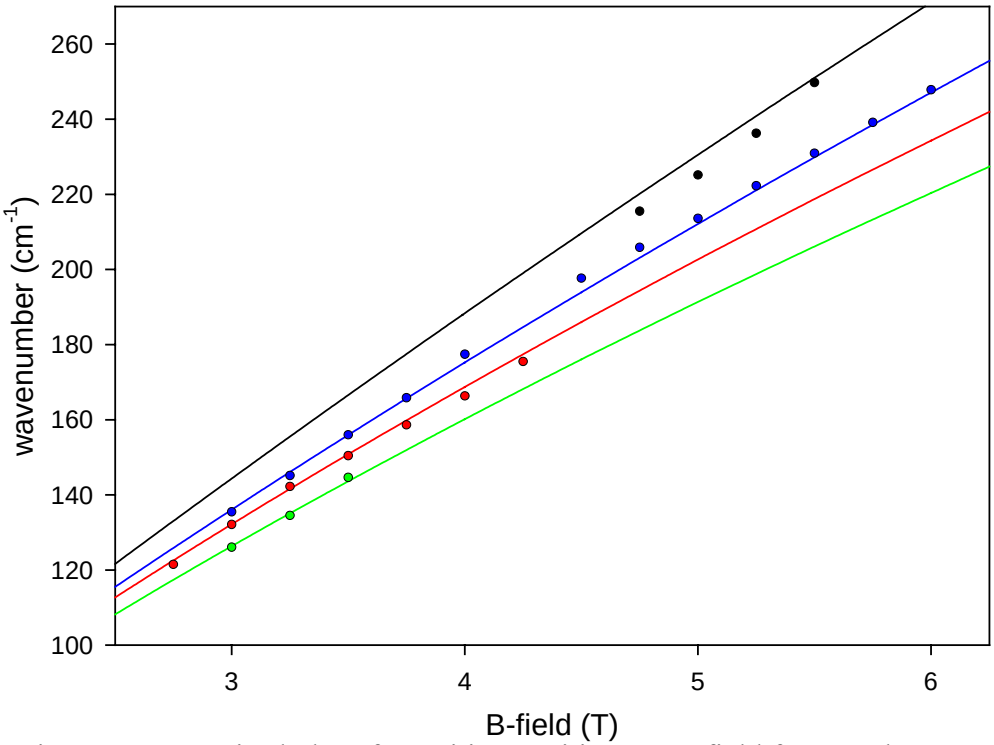

Figure 3.14: Revised plot of transition position vs. B-field for sample s702. The colors of the dots representing the experimental transitions correspond to the color of the predicted transition lines.

Due to the periodic nature of the noise present in sample s702 (a period of approximately 5.4 cm^{-1}) the most likely source of this noise is the Fabry-Perot interference mentioned previously. Further increasing the wedge angle for the sample piece used in the experiment could reduce this noise.

Figures 3.9 and 3.10 show us that the Landau level theory can accurately predict the positions of the cyclotron resonances. Can the same be said about the cyclotron resonance INTENSITIES discussed above? Recall that the size, or value, of the predicted intensities should be a function of both the fraction of the initial state that is filled with electrons, as well as the fraction of the final state that is empty. Thus, a formula for the predicted intensities should look something like: Intensity ~ $f_{filled}(E_{initial})$ * [1 - $f_{filled}(E_{final})$]. If we plot the measured intensities vs. B-field for s499 along with theoretical lines derived from the equation given, Figure 3.15 is produced. Note that for this figure, an electron density of $2.0x10^{11}$ cm^{-2} is assumed. This value comes from Hall and Shubnikov-de Haas measurements done on the sample as mentioned in Chapter 2.

Looking at Figure 3.14 one see that there is some rough agreement in the general shape of the curves and the way that the experimentally determined intensities change with changing B-field. For example, the red dots decrease in intensity and fall to zero at filling factor two and the black dots are at zero intensity, then steadily increase in intensity after filling factor two. Blue, on the other hand, is more of a mystery as the experimental data increases up to filling

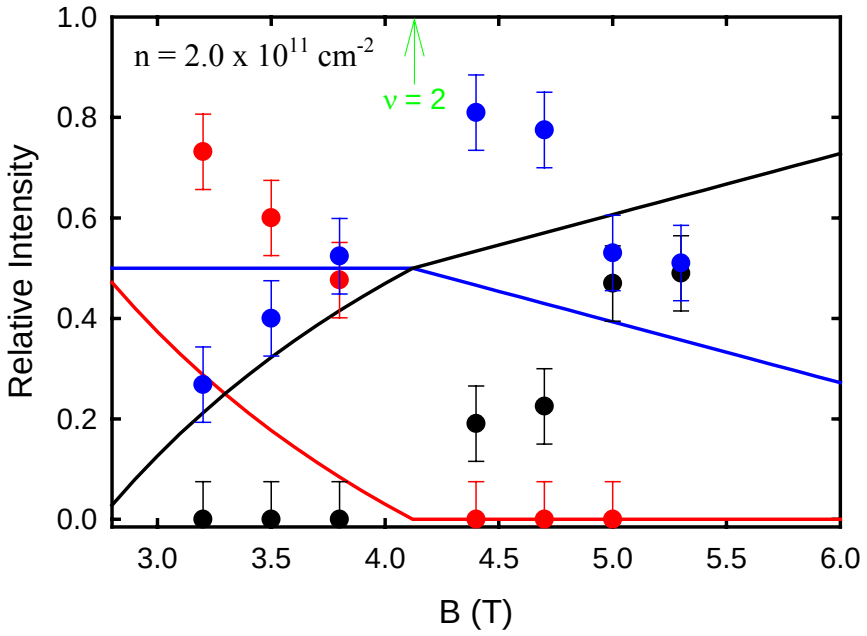

Figure 3.15: Relative CR Intensity vs. B-field for s499. The dots represent the experimentally determined intensities while the lines represent theoretical intensities.

factor two, then decreases after. So, after some initial considerations, the theory thus far can only somewhat explain the CR intensity variations.

However, this is not the entire story for the CR intensities. Improvements can be made on the theory explained above. The first of which is to more accurately determine an equation that describes the intensities of the different resonances. This is accomplished by once again turning to quantum mechanics. Recall that the Hamiltonian describing the interaction of an electron with an electromagnetic field is:

$$H = \frac{[p + (e/c)A(r,t)]^2}{2m} + V(r) \qquad (3.4)$$

where V(r) is the static potential and A(r,t) is the vector potential. This leads to a transition rate given by **Fermi's Golden Rule:**

$$R_{i->f} = \frac{2\pi}{h}\left|M_{fi}\right|^2 \rho(E) \tag{3.5}$$

where ρ(E) is the density of states and M_{fi} is the matrix element of the perturbation between the initial and final states. It is this matrix element M_{fi} that will play the most important role in the effort to more accurately describe the CR resonances, so it should be examined closer.

In general, M_{fi} is of the following form:

$$M_{fi} = \left\langle \phi_f \left| e^{-ik.r}\, \varepsilon \cdot p \right| \phi_i \right\rangle \cong \left\langle \phi_f \left| \varepsilon \cdot p \right| \phi_i \right\rangle = im\omega\varepsilon \cdot \left\langle \phi_f \left| r \right| \phi_i \right\rangle \tag{3.6}$$

However, this experiment deals with a purely one dimensional case, so this simplifies to:

$$M_{nm} = im\omega\varepsilon \left\langle \phi_n \left| \hat{x} \right| \phi_m \right\rangle \tag{3.7}$$

where

$$\hat{x} = \frac{\lambda}{\sqrt{2}}(\hat{a}^+ + \hat{a}) \tag{3.8}$$

Therefore,

$$\left\langle \phi_n \left| \hat{x} \right| \phi_m \right\rangle = \frac{\lambda}{\sqrt{2}}(\sqrt{m+1}\,\delta_{n,m+1} + \sqrt{M}\,\delta_{n,m-1}) \tag{3.9}$$

However, for this experiment, interest only lies in transitions from a lower to a higher Landau Level, so the second term in equation (3.9) drops out. This leaves an n (or m+1), which is the quantum number of the final state. Refer to this state as N_{final} from now on.

The result of this analysis is that in order to more accurately predict the transition intensities the n-value of the final state of the transition should be included in the equation for the transition intensities. In other words, the equation for the transition intensities should be of the form:

Intensity ~ $f_{filled}(E_{initial})$ * [1 - $f_{filled}(E_{final})$] * N_{final}. Now, if Figure 3.15 is redone considering the above discussion, Figure 3.16 is the result.

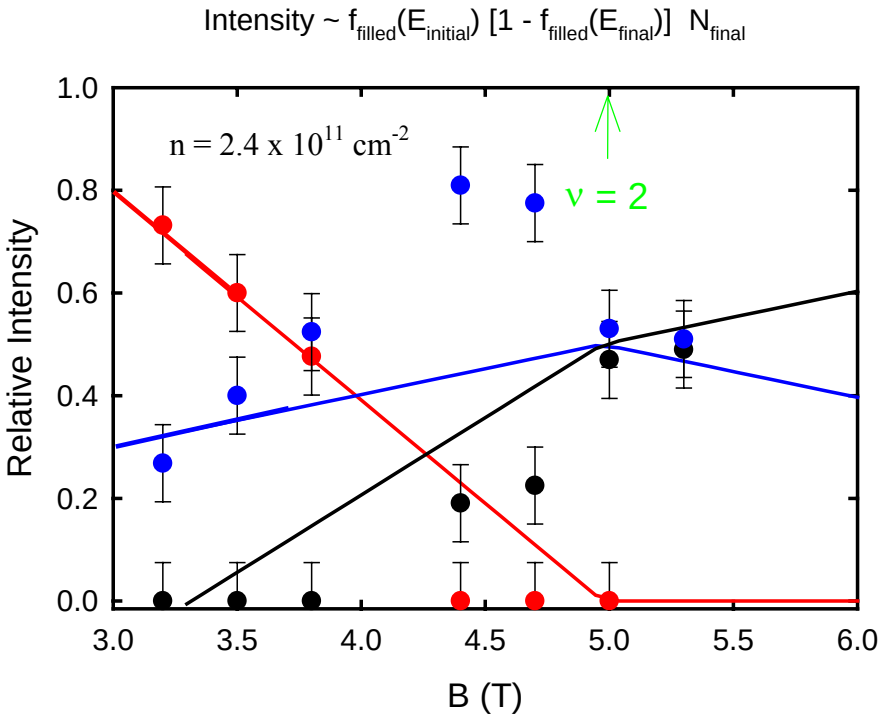

Figure 3.16: Relative CR Intensity vs. B-field for s499 with inclusion of final Landau Level value and increased electron density.

Notice also in Figure 3.16 that the density has been increased to 2.4 x 10^{11} cm^{-2}, thus producing a shift of the position of $\nu = 2$ to the right. These changes bring our experimental and theoretical data into much closer agreement then seen previously.

However, the presence of spin split cyclotron resonance in sample s499 extends to higher magnetic fields than 6 Tesla. Although these resonances also lie along the colored transition lines shown in Figure 3.9, the position of the relative intensities behaves in a somewhat unusual manner, as can be seen in Figure 3.17.

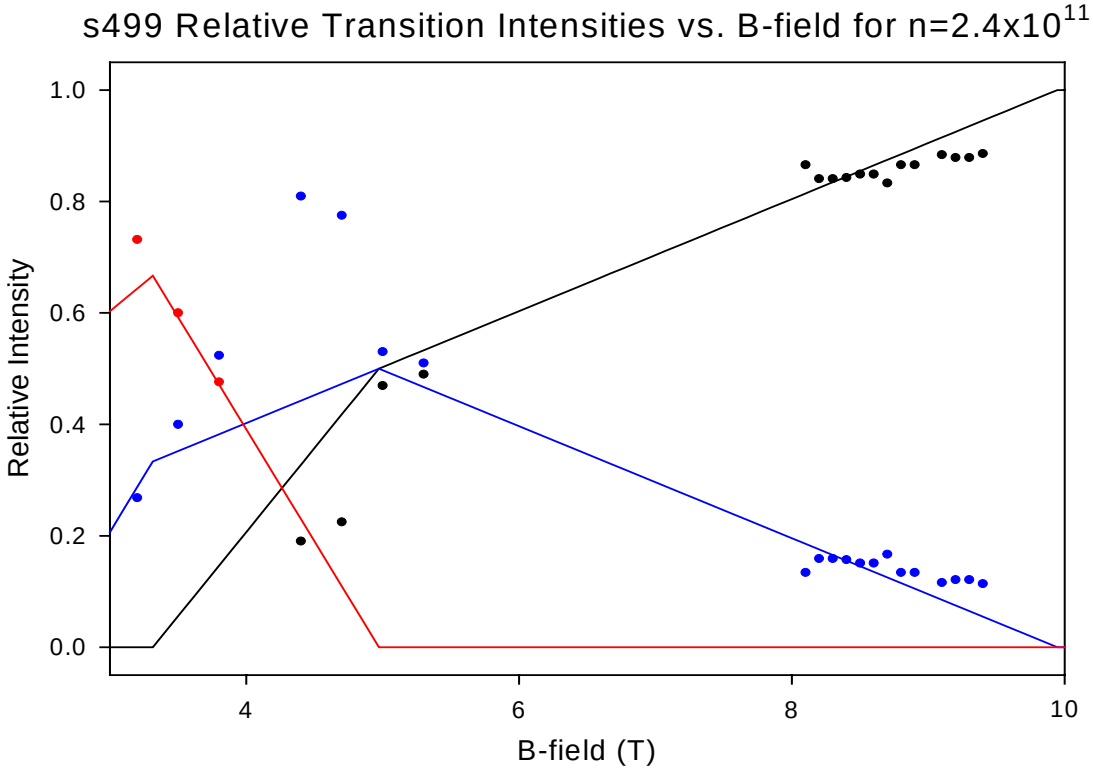

Figure 3.17: Extension of the relative transition intensity vs. B-field plot for s499 shown above. Notice how the black and blue transition intensities appear to become constant at higher B-field. SdH density for s499 is 2.1x10^{11} cm^{-2}.

Clearly, for the transitions that lie above the optical phonon window that is due to the sample's substrate layer (5.5 T < B < 8 T for this sample, refer back to Figure 3.6), the transition intensities appear to maintain a constant value, rather than the black transition increasing intensity while the blue transition loses intensity, as predicted by theory. Also, consider a similar analysis applied to sample s716, as shown in Figure 3.18. Again, like in sample s499, although the black and blue

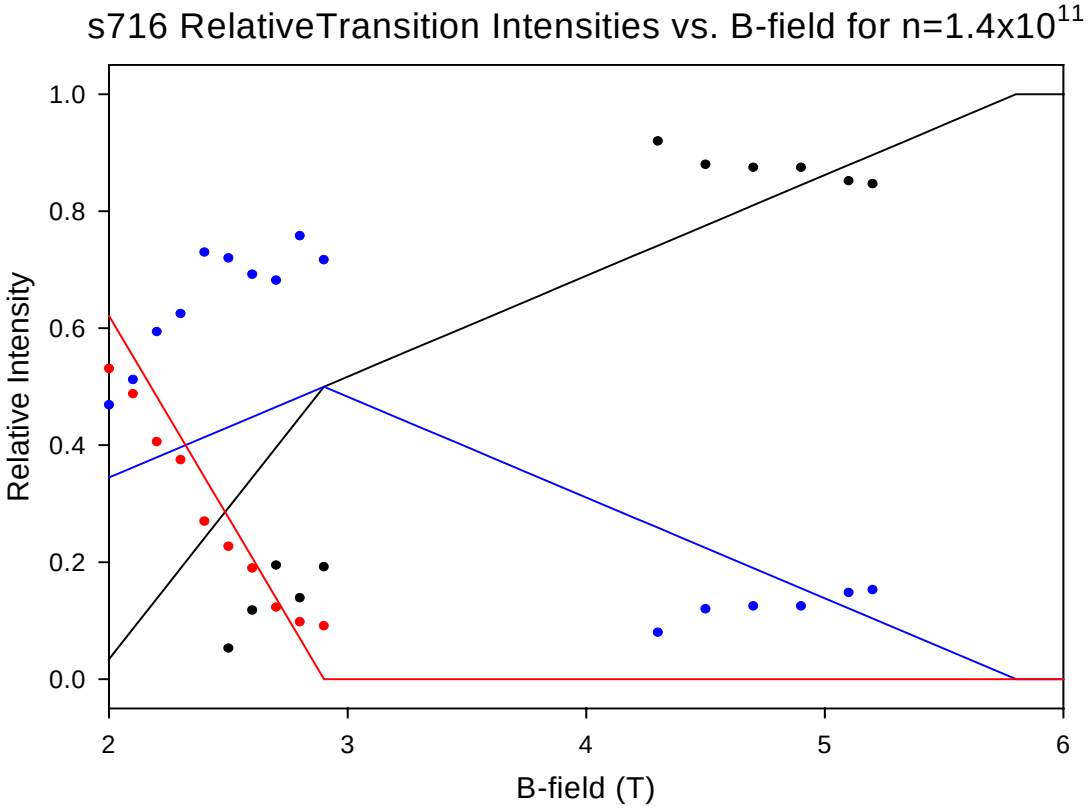

Figure 3.18: Relative transition intensity vs. B-field for sample s716. SdH density for s716 is 1.4×10^{11} cm^{-2}. See Figure 6.11 for related spectra.

transitions have approximately the predicted relative intensity values (0.1 for blue and 0.9 for black), both transitions appear to maintain a relatively constant value

in the higher magnetic field region. However, unlike s499, the higher field transitions in sample s716 are above the phonon region due to the $Al_xIn_{1-x}Sb$ buffer layer (3 T < B < 4 T in this sample), not the optical phonon window of the substrate layer. In fact, the proximity of these transitions to the optical phonon window of the InSb may lead one to conclude that the constancy of these transition intensities in sample s716 is due to some magneto-polaron effect. Recall that a magneto-polaron is a coupling of the cyclotron resonance motion of the electrons to the phonon lattice vibrations of the host crystal. This coupling results in an avoided level crossing occurring in the cyclotron resonance trace near the point where the cyclotron resonance energy equals the LO phonon energy (approximately 180 cm^{-1} for InSb). However, since the same constancy was seen in s499 for transition intensities above the substrate absorption region, it must be concluded that the constancy of the higher field transition intensities is not due to a magneto-polaron effect. For further reading on magneto-polarons see Ref. [27 – 30].

In addition to the unpredicted constancy of the transition intensities for higher fields for both s499 and s716, Figures 3.17 and 3.18 also share another unusual feature. Specifically, the deviation in the intensity of the blue transition from the theoretical prediction between filling factors 2 and 3. For both samples, the experimental transition intensities are significantly above the predicted values in this region.

Also, included in Figure 3.19 is the relative transition intensity vs. magnetic field plot for sample s702. Unfortunately, as seen before, the noise associated with this sample was quite large, making an accurate determination of transition intensity quite difficult. For this sample, the above mentioned anomaly in the blue transition is not seen because of the presence of the magneto-polaron region.

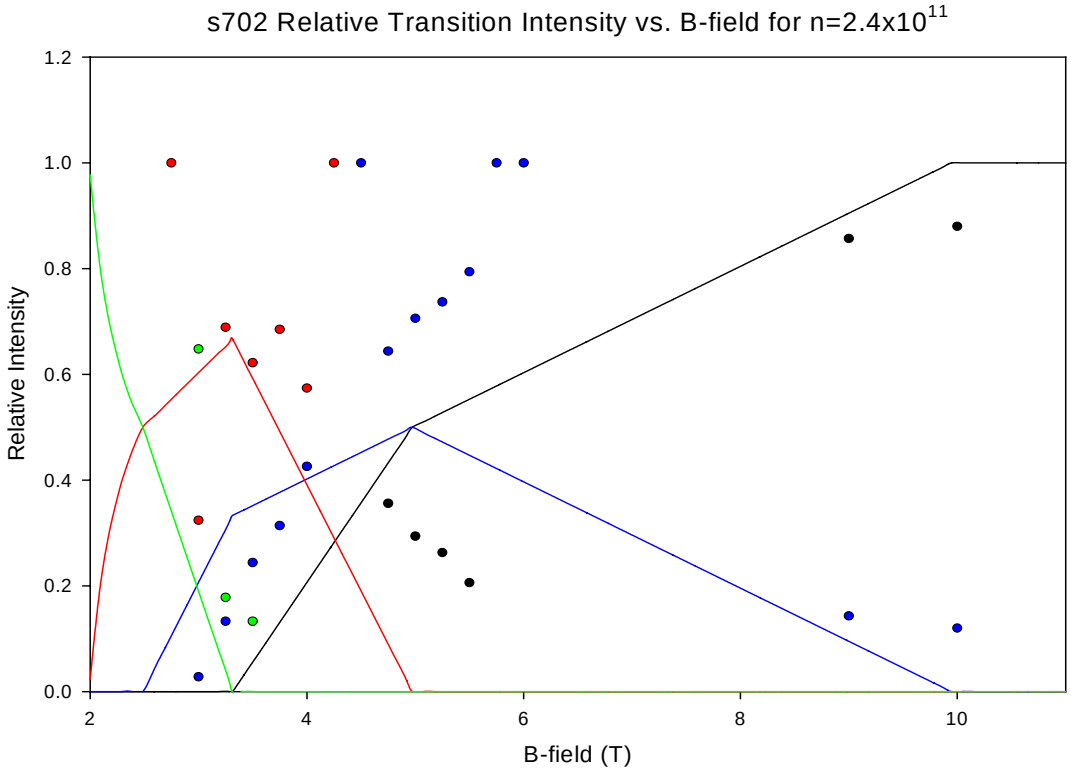

Figure 3.19: Relative transition intensity vs. B-field for sample s702. SdH density for s716 is 2.4×10^{11} cm^{-2}.

As the discussion above concluded, there exist intensity anomalies in the experimentally observed cyclotron resonance transitions in our InSb samples. Also mentioned above, spin split cyclotron resonance has been seen in other

semiconductors. As mentioned in the introduction to this chapter, Scriba *et al.* [21] also saw a splitting in the cyclotron resonance traces in the non-parabolic quantum well system of InAs/AlSb. As can be seen in Figure 3.20, no intensity anomaly was present, possibly due to the fact that this experiment was carried out at lower electron densities and higher filling factors.

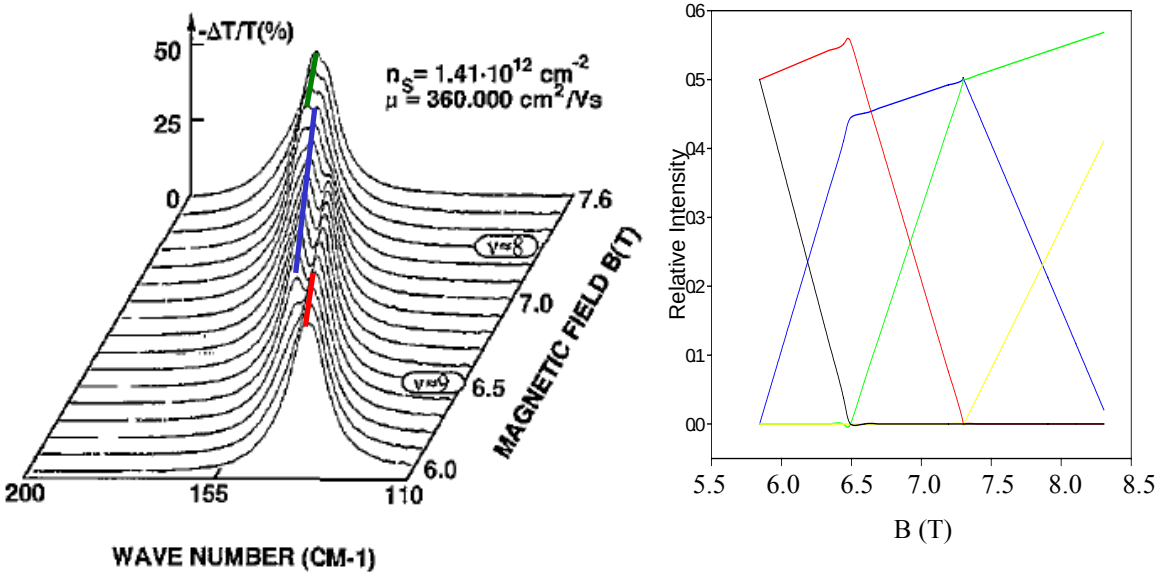

Figure 3.20: Data obtained from InAs quantum wells by Scriba *et al.* [21] showing no intensity anomaly in the CR transition intensities.

In addition to InAs/AlSb, spin split cyclotron resonance has also been observed in GaAs-AlGaAs heterostructures [31, 32, 44]. However, unlike in the InSb/AlSb case, Wu *et al.* [44] did indeed see an intensity anomaly, as shown in Figure 3.21.

This study found that when $\omega_c \geq \omega_{LO}$ in high density 2DEGs, the frequency ordering of the spin-resolved CR lines was reversed. This reversal of the CR

intensities is explained in these samples by polaron and many-body effects. However, as was discussed earlier in relation to Figures 3.17 and 3.18, an explanation involving magneto-polarons will not explain the intensity anomaly observed in our study.

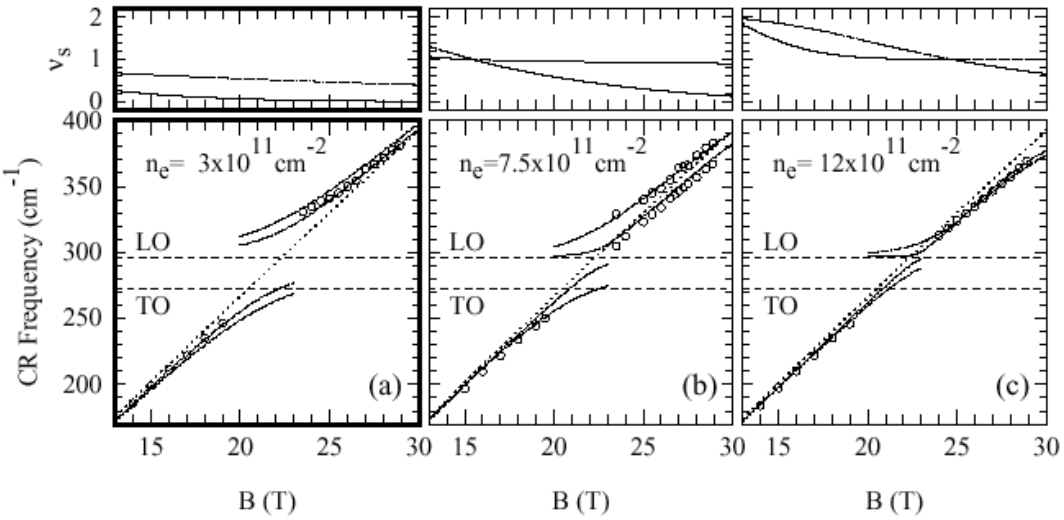

Figure 3.21: Plots of spin split CR data gathered using GaAs-AlGaAs heterostructures. The upper panels show the Landau-level occupancy of the spin-down (solid curve) and spin-up (dash-dotted curve) electrons, respectively. The lower panels show the measured CR frequency vs. B-field for three samples of different densities. [44].

Before this section on the experimental results is concluded, a few words need to be said about the method used to experimentally determine the CR intensities. This is accomplished by fitting the experimental CR traces with the matrix method described in Ref. [45] and Ref. [46]. Using this method, the complex index of refraction and the transmittance can be calculated using:

$$t_{\pm} = \frac{2}{[(1+n_0)\cos\Theta_{\pm} + i(n_{\pm} + n_0/n_{\pm})\sin\Theta_{\pm}]} \qquad (3.10)$$

$$T(B) = \frac{n_0(|t_+|^2 + |t_-|^2)}{2} \tag{3.11}$$

$$n_\pm = [\varepsilon - i\sigma_\pm(B)/\omega\varepsilon_0]^{1/2} \tag{3.12}$$

$$\sigma_\pm = \frac{n_s e^2}{z m^*_{CR}} \frac{1}{1/\tau_{CR} + i(\omega \pm eB/m^*_{CR})}. \tag{3.13}$$

Here, the $\pm$ sign refers to the right and left circularly polarized light, ε is the dc dielectric constant, and $n_\pm$ is the complex index of refraction. Further, $\Theta_\pm = (\omega/c)n_\pm z$ where z is the thickness of the two dimensional electron gas, $n_0 = \sqrt{\varepsilon} = 4.2$ for InSb, and finally σ(B) is the Drude conductivity.

On a more practical note, the above model was used to write a *Mathematica* notebook that performed the necessary calculations. The best fit was obtained by altering three input variables per CR transition until a good visual fit was achieved. These input variables are the number of electrons involved in the transition, n_s, the effective electron mass as a fraction of the electron rest mass, m_{frac}, and finally, the CR lifetime, τ_{CR}. In practice, n_s controls the overall area of the theoretical CR transition, m_{fac} controls the position of the transition, and τ_{CR} controls the FWHM. An example of a theoretical fit to some of the experimental data for sample s499 is given in Figure 3.22. Once a good fit to the experimental data is obtained, the densities for the individual transitions are

divided by the total density, and the result is the experimental relative transition intensities shown in Figure 3.15 - 3.18.

A careful look at Figure 3.22 does indicate a possible problem however. Notice how the total density for the theoretical fit in Figure 3.20 is 3.4×10^{11} cm^{-1}

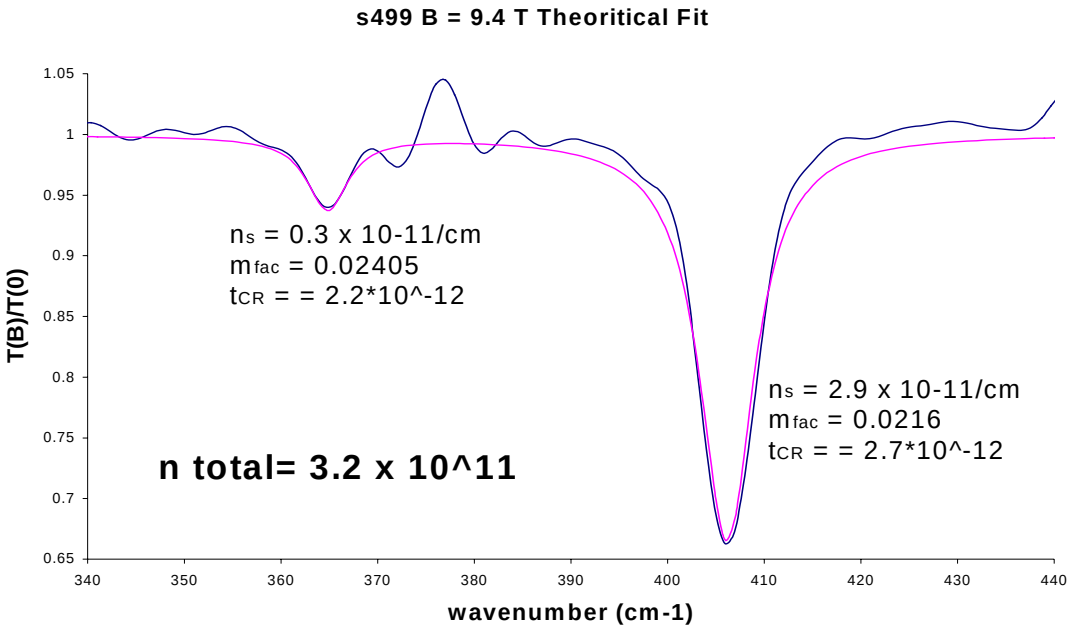

Figure 3.22: Theoretical fit to the experimental data for sample s499 at 9.4T. The density values obtained are then used to determine the experimental intensity for each transition.

rather than a density of 2.4×10^{11} cm^{-1} used in Figure 3.16 for sample s499. Upon a first consideration, this would appear to be a major problem. However, recall that the theoretical fitting is used to determine the *relative* intensity of the transitions in question. In other words, the method discussed above is used to get a measure of the intensity of one transition relative to another. Therefore, the total calculated intensity is of little concern. Rather, it's the relative size of one

transition to another that matters and it is this relative size that is plotted in Figures 3.15 – 3.18.

This result is interesting however, since in Ref [46] this model was used in conjunction with the sample's Shubnikov-de Haas (SdH) determined density to fit the experimental data, using only τ_{CR} as the fitting parameter. The results of this are shown in Figure 3.23. As one can see in the figure, good agreement is achieved using the sample's SdH density and only varying τ_{CR}.

A possible short coming of this method of line fitting is the fact that it is based on a classical model. Other fitting methods based on quantum mechanical models do exist and some can be found in Ref. [47 – 50]. In addition, a more detailed look was taken at this classical model and it was found that the area under the theoretical curve was not directly proportional to the density used to produce that curve. For example, the ratio of area under the curve to density for a curve generated using a density of 2.0×10^{11} was found to be 1.14. However, the same ratio for a curved generated using a density of 4.0×10^{11} was 0.977. Thus, it would seem that the deduced electron density can depend on the model chosen.

3.6 Conclusions

In this chapter the cyclotron resonance experiments carried out at the NHMFL have been explored. It has been seen that spin-resolved cyclotron

resonance is indeed observed in InSb quantum well samples with electron densities of $n \approx 2.0 \times 10^{11}$ cm^{-2}. Also, it has been seen the transition energies can

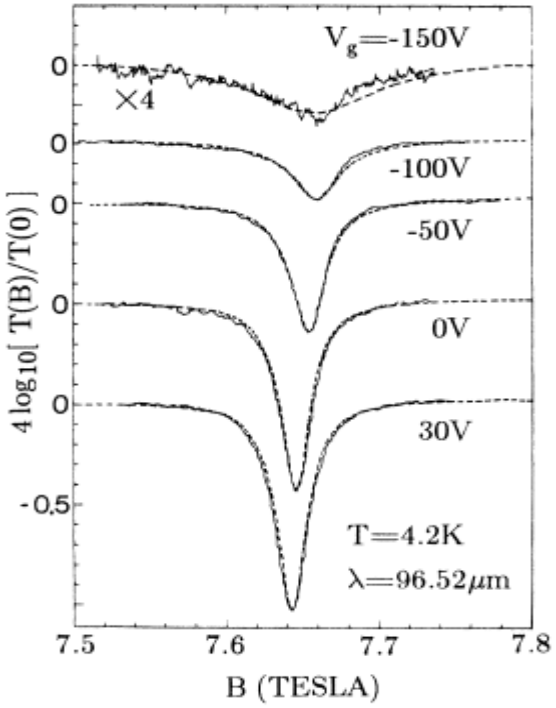

Figure 3.23: Theoretical fittings for the data gathered in [46], using the matrix method described above. Solid curves are the experimental traces of cyclotron resonance as a function of B for different back gate voltages. Dashed curves are the fits of the transmittance using τ_{CR} as the fitting parameter.

be explained by a relatively simple Landau level plot, derived from a single electron model [51], and non-parabolic E(k). The transition intensities can be somewhat explained by this same model, at least at lower magnetic fields. However, at higher magnetic fields, the experimental transitions appear to maintain constant intensities, in contrast to what the theory predicts.

Chapter 4

Same Spin Anti-Crossings

Two dimensional electron systems in various GaAs structures in a magnetic field have been shown to exhibit coupling between the Landau levels of the various subbands within the system [52 – 61]. However, in these studies spin-splitting was not resolved. This chapter will focus on using cyclotron resonance to probe anti-crossings that occur between Landau levels of different subbands within the same quantum well. Specifically, this chapter will discuss anti-crossings that occur between same spin states. Chapter 5 will consider opposite spin anti-crossings. To begin, we will review the sample structure once more in order to understand how the fan diagram changes with the inclusion of different subbands in the well. We will then touch on previous experiments done using GaAs [62, 63, 64,] where the first evidence of anti-crossings was observed. Next, a theoretical foundation will be look at to explain the anti-crossings and a comparison will be made between the theoretical and experimental results for the same spin crossings.

4.1 Review of Sample Structure

Once again, the samples used for this experiment are triple δ - doped InSb quantum well samples with AlInSb barrier material. For reference, the sample structure for sample s842 is given in Figure 4.1. This sample was used to gather

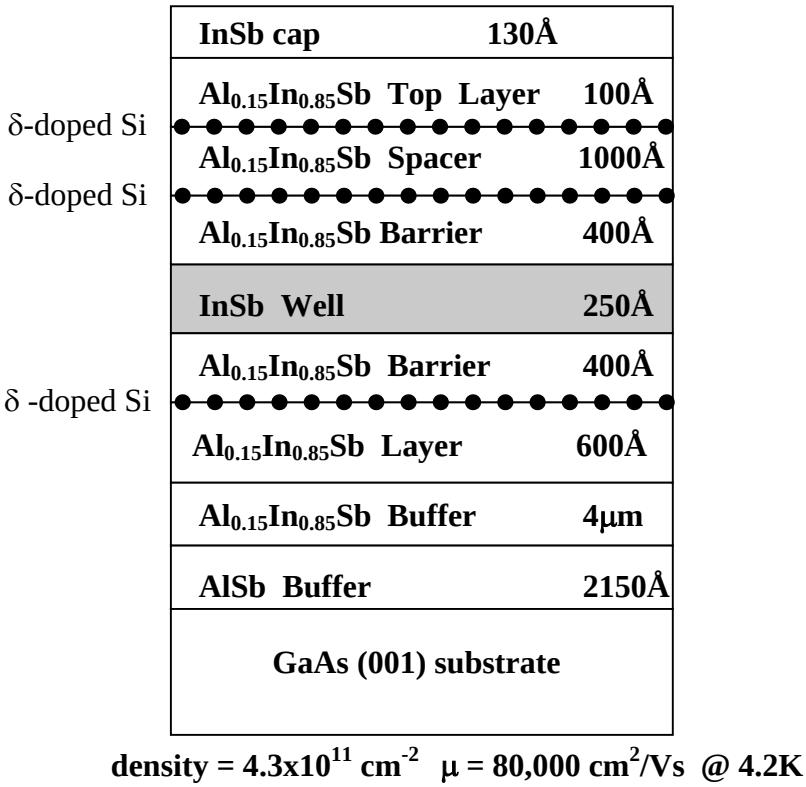

Figure 4.1: Layer structure for sample s842. Notice the large 15% barrier. This will generate a much deeper well with more bound subbands.

the majority of the data that will be discussed in both this chapter and the next. Notice that for this sample, a 15% barrier was used. This creates a much deeper well, resulting in multiple bound states, or subbands, in the well. Also, notice that

the well itself is somewhat more narrow (250Å) than seen previously. This causes these bound states to have a greater energy separation in the well. The results of the larger barrier and more narrow well are more clearly seen when looking at the energy diagram for s842, shown in Figure 4.2. As can be seen in

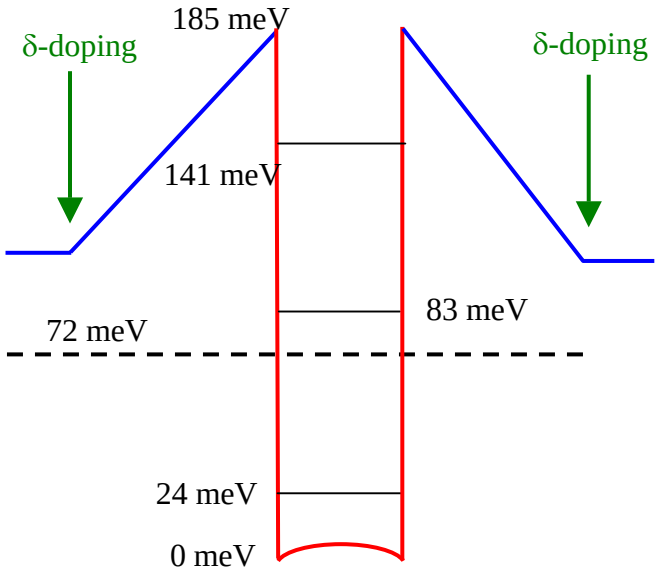

Figure 4.2: Energy diagram for sample s842. Notice the large depth of the well resulting in multiple subbands being bound in the well.

the figure, the calculated well height is 185 meV, and there are three bound states contained in the well at calculated energies of 24 meV, 83 meV, and 141 meV. Also, notice that the Fermi level is 72 meV. This means that only the lowest subband is populated with electrons. Also notice that this sample is again symmetrically doped. Therefore, the electrons in the well will feel no net electric field from the dopants. This fact will be important in Chapter 5.

4.2 Multiple Fan Diagrams

In the previous section we discovered that for a deep enough well, multiple bound states are contained in the well. How does this fact affect the fan diagram discussed previously? Referring back to the derivation of the electron energy in chapter 3, recall that the allowed energy states for an electron bound in the well was given by:

$$E_n = \hbar\omega_c(n + \tfrac{1}{2}) \pm \tfrac{1}{2} g\mu_B B \tag{4.1}$$

where the first term is due to the quantized orbits and the second term is due to the Zeeman spin splitting. However, with multiple bound states in the well, we also need to take into account the energy of the different subbands. This additional subband energy has been included in Equation 4.2 [66]:

$$E_n = E_m + \hbar\omega_c(n + \tfrac{1}{2}) \pm \tfrac{1}{2} g\mu_B B \tag{4.2}$$

Therefore, for electrons bound in the well, in addition to the previously discussed spin-split Landau levels for the lowest bound state, there are also allowed spin-split Landau levels for the higher bound states. What this means is that each bound state in the well has its own associated fan diagram, and these different "bound state fan diagrams" sit on top of one another, with a separation in energy determined by the energy separation of the bound states in the well. A simple schematic of this situation is given in Figure 4.3. For simplicity, Figure 4.3 only shows the n = 0,1,2 spin-split levels of the lowest bound state and only the n = 0 spin-split level for the next highest bound state. Notice in the figure that when the

Landau levels from the second subband are included, multiple crossings occur between the Landau levels of the two subbands. Four of these crossings are indicated in Figure 4.3. Further, consider that these crossings fall into one of two categories: A) crossings where the states involved are of the same spin, or B) crossings where the states involved are of opposite spin. Looking at the figure, one notices that crossings 2 and 3 are of the same spin variety, while crossings 1 and 4 are of the opposite spin type. The remainder of this chapter will focus on these same spin crossings (crossings 2 and 3).

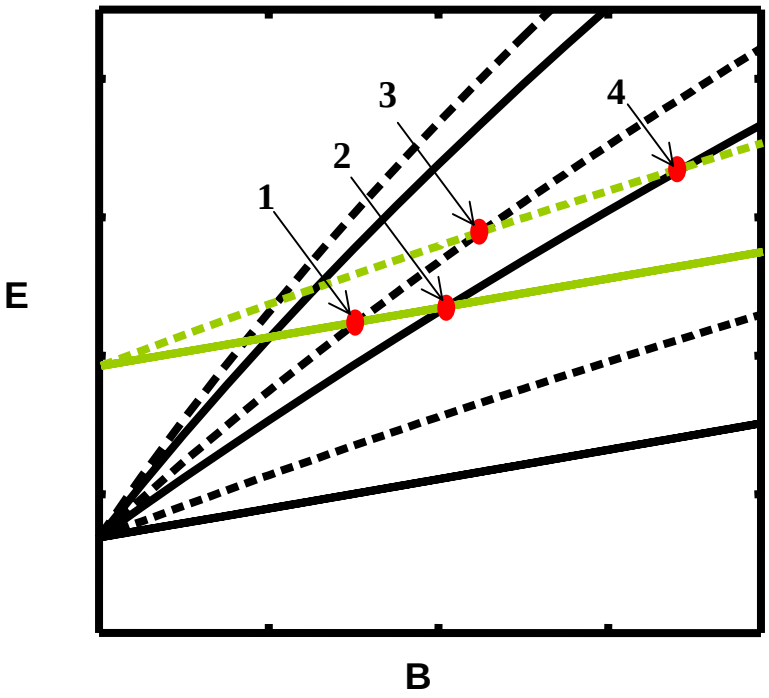

Figure 4.3: Schematic diagram of Landau levels from multiple subbands. Notice that multiple crossings occur between the Landau Levels of the two bands. These crossings can be either same spin crossings (2 and 3) or opposite spin crossings (1 and 4).

4.3 Previous Evidence of Anti-Crossings

As mentioned in the introduction to this chapter, the first observation of subband Landau level coupling was reported by Schlesinger *et al*. [62] approximately twenty years ago using GaAs/AlGaAs heterostructures. This coupling was observed as a splitting in the cyclotron resonance transition from level n to n + 1 in the ground state subband. A schematic of the levels involved and the resulting anti-crossing in the cyclotron resonance is shown in Figure 4.4.

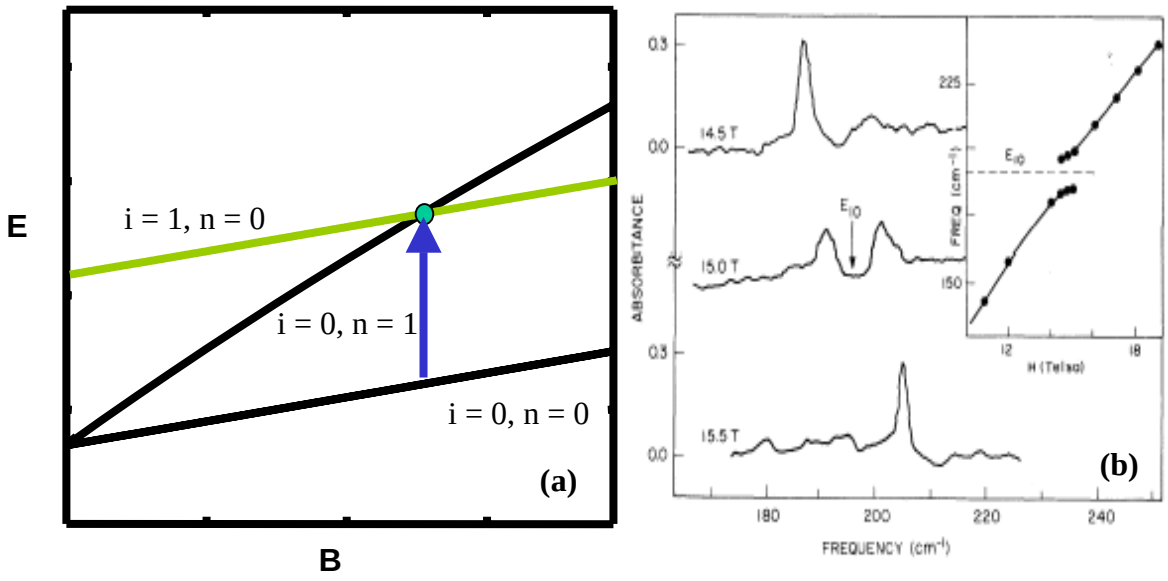

Figure 4.4: Previous evidence of anti-crossings that occurred in GaAs/AlGaAs heterostructures. (a): Schematic of the Landau Levels and transition involved in the anti-crossing. (b): CR data showing the anti-crossing. [62]

Due to weak band non-parabolicity and a small g-factor for GaAs (g = -0.5), the spin splitting of the cyclotron resonance is small. Therefore, spin splitting was not included in Figure 4.4(a). This means that in these previous studies, crossings

between the various spin states could not be observed, and therefore only one crossing was seen instead of four.

For InSb, however, the spin splitting is much stronger (g = -51), as indicted in Table 3.1. Therefore, in our study using InSb quantum wells, we were able to look at both same-spin and opposite spin crossings. However, before discussing our results, we need to establish a theoretical basis describing coupled Landau levels.

4.4 Theory of Coupled Landau Levels

The theory of coupled Landau levels was established by Wieck *et al.* in 1989 [64]. This theory is as follows. Consider the one electron Hamiltonian for a 2D electron gas in a magnetic field given in Equation 4.3:

$$H_0 = -\frac{\hbar^2}{2m^*}\frac{\partial^2}{\partial x^2} + \frac{e^2 B_\perp^2}{2m^*}x^2 - \frac{\hbar^2}{2m^*}\frac{\partial^2}{\partial z^2} + V(z) \tag{4.3}$$

Here the vector potential has been taken in the Landau Gauge:

$$\vec{A} = (0, xB\cos\theta - zB\sin\theta, 0) \tag{4.4}$$

and the orbit center transformation $x \rightarrow x - hk_y/eB_\perp$ has been applied. Now, if the sample is tilted slightly with respect to the magnetic field then the Hamiltonian given in Equation 4.3 becomes:

$$H = H_o + H_{tilt}, \tag{4.5}$$

where

$$H_{tilt} = \frac{e^2 B_{\|}^2}{2m^*} z^2 - \frac{e^2 B_{\perp} B_{\|}}{m^*} xz \tag{4.6}$$

For small tilt angles, this additional Hamiltonian, H_{tilt}, can be treated as a perturbation on H_o and first-order degenerate perturbation theory can be applied.

Begin by considering the first term in Equation (4.6). Because of the z^2 term this expression contains, it will not couple the necessary Landau Levels together to produce the desired anti-crossings. Referring back to Figure 4.3, one will notice that we are looking for a perturbative term that will couple Landau levels together that differ by one in both subband index and Landau level index. The second term in Equation (4.6) is more promising however. When this term is applied as a perturbation between degenerate levels $\left| i+1, n-1, s' \right\rangle$ and $\left| i, n, s \right\rangle$ where *i* is the subband index, *n* is the Landau Level index, and *s* is the spin state (up or down), the result is the following:

$$\left\langle i+1, n-1, s' \left| \frac{e^2 B_{\perp} B_{\|}}{m^*} xz \right| i, n, s \right\rangle = \frac{e^2 B_{\perp} B_{\|}}{m^*} \left\langle n-1 \left| x \right| n \right\rangle \left\langle i+1 \left| z \right| i \right\rangle \left\langle s' \middle| s \right\rangle \tag{4.7}$$

Now, for the matrix element $\left\langle n-1 \left| x \right| n \right\rangle$ we have:

$$\left\langle n-1 \left| x \right| n \right\rangle = \left(\frac{n}{2} \right)^{1/2} l_{\perp} \tag{4.8}$$

where $l_{\perp}$ is the magnetic length $\left(\hbar / eB_{\perp} \right)^{1/2}$ [64]. Applying this to Equation (4.7) and making the substitution $B_{\|} = B_{\perp} \tan\theta$ we get:

$$\left\langle i+1, n-1, s' \left| H_{tilt} \right| i, n, s \right\rangle = \frac{e^2 B_{\perp} B_{\perp} \tan\theta}{m^*} \left(\frac{n}{2} \right)^{1/2} \left(\frac{\hbar}{eB_{\perp}} \right)^{1/2} \left\langle i+1 \left| z \right| i \right\rangle \left\langle s' \middle| s \right\rangle \tag{4.9}$$

Finally, after some algebra and using the fact that $\omega_c = eB_\perp/m^*$ and $E_{i+1} - E_i = \hbar\omega_c$ we arrive at the predicted level splitting for this perturbation:

$$\Delta E = 2\langle i+1, n-1, s' | H_{tilt} | i, n, s \rangle = \sqrt{\frac{2neB_\perp}{\hbar}} (E_{i+1} - E_i) \tan\theta \langle i+1 | z | i \rangle \langle s' | s \rangle \qquad (4.10)$$

However, before an analysis of what Equation 4.10 predicts, a few words about the wavefunctions $|i\rangle$ is warrented. Recall from Chapter 1, the Kane model was used to solve the Schrödinger equation for the wavefunctions of electrons confined in a square well potential self-consistently. It is these wavefunctions that are represented by the $|i\rangle$ term used above.

Returning to Equation 4.10, there are a number of characteristics to notice about this energy splitting. First, with the inclusion of the tan θ term, the size of the energy gap should have roughly linear dependence on tilt angle, for small tilt angles. Also, there should only be coupling between levels with an odd index change of one, if the quantum well is assumed to be symmetric. This is a result of the parity of the individual components of $\langle i+1 | z | i \rangle$ (odd, odd, and even, respectively). Furthermore, coupling should only occur between levels that have a difference of Landau level index of one ($\Delta n = 1$) due to the raising and lower operator characteristics of *x*. Finally, due to the last term in Equation 4.10, this theory predicts that only levels with the same spin should couple together.

4.5 Our Results

Now that an understanding of the theory and expected results for same spin crossings has been established, let's turn to the results we obtained using InSb quantum well samples. Utilizing cyclotron resonance as a probe on sample s842, in the vicinity of the predicted same-spin crossings (i.e. crossings 2 and 3 in

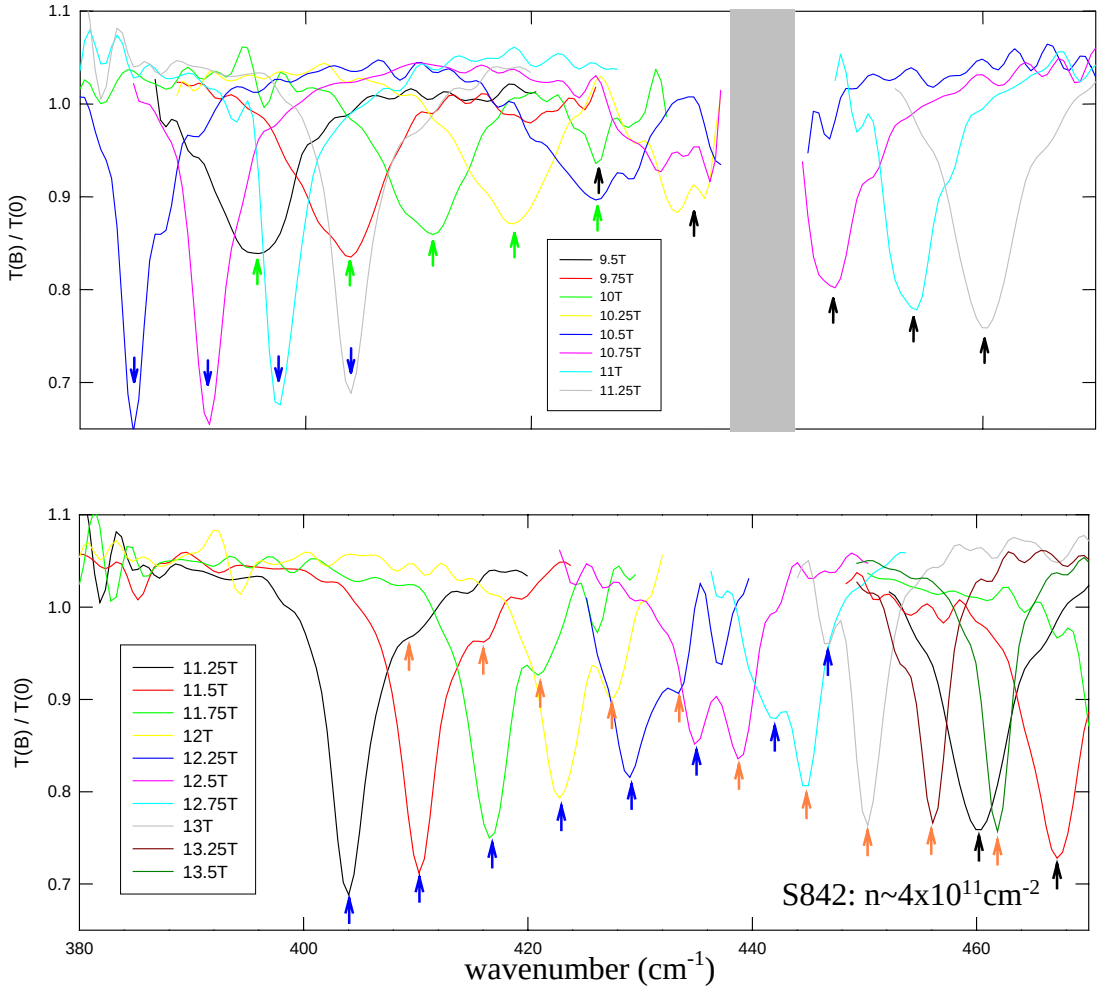

Figure 4.5: CR traces in the vicinity of the predicted same-spin crossing for sample s842 at a tilt angle of 4°. Notice the clear presence of the gap predicted by the theory.

Figure 4.3) we did indeed see a clear anti-crossing in the CR traces as can be seen in Figure 4.5. As can be seen in the figure, the anti-crossings is characterized by a splitting in a single cyclotron resonance peak. Also, as the magnetic field is swept, the intensity of one of the split peaks should decrease, while the other increases. This produces the characteristic "mound" shape in the traces as seen in Figure 4.5.

Plotting the positions (i.e. energies) of these CR absorptions as a function of magnetic field allows us to better see the resulting energy gap in our samples, as was seen in the GaAs experiments before. The Landau levels and transitions involved, as well as the a plot of E vs. B for the transitions is shown in Figure 4.6.

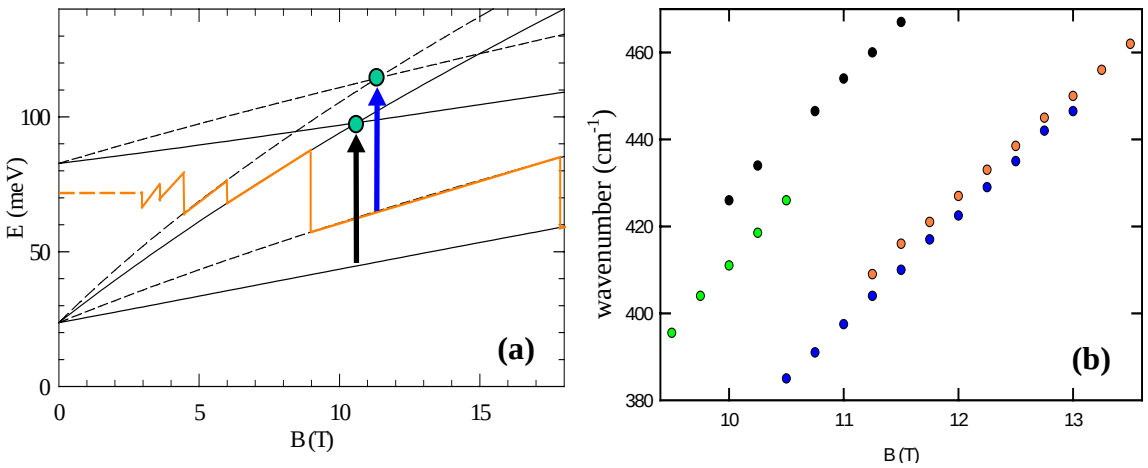

Figure 4.6: (a): Landau Levels and transitions involved in the same-spin crossings for sample s842 at a tilt angle of 4°. (b): E vs B for the CR transitions for sample s842 showing the expected energy gap.

As can be seen in the figure, for the black transition occuring at crossing 2, an energy gap of approximately 1.7 meV (14 cm^{-1}) is present at a sample tilt angle

of 4^0. Likewise, for the blue transition occuring at crossing 3, a gap of approximately 0.5 meV (4 cm^{-1}) occurs for the same tilt angle. The gap size is taken as separation in the two peaks when the intesity of the peaks is equal.

So we do indeed see the energy gaps opening up for the same-spin crossings that occur between the Landau Levels of the i = 1 and the i = 2 subbands (so Δi is odd) as predicted by the theory. Also, the transitions involved are from the n = 0 to the n = 1 Landau Levels of the lowest subband (so $\Delta n = 1$), again in agreement with the theory. And finally, to reiterate, these crossings are of the same-spin variety.

Next, let us turn our attention to the tan θ term found in Equation 4.10. This term predicts that the size of the energy gap due to an anti-crossing between same spin states should be roughly linear with respect to sample tilt angle, for small tilt angles. Using wedged sample mounts, we measured the size of the resulting energy gap for sample s842 at various tilt angles ranging from approximately zero tilt to 11^0. These results are summarized in Figure 4.7. Notice that the resultant splitting is roughly proportional to tilt for these same spin crossings. However, also notice that the experimentally measured gap for these same spin anti-crossings increases much more slowly with θ than the prediction of Equation 4.10. Also, note that the experimental slope of ΔE vs. B in Figure 4.7 depends on spin. In other words, the resulting energy gap that occurs between two spin-up Landau Levels (anti-crossing 2) has a greater slope versus B-field

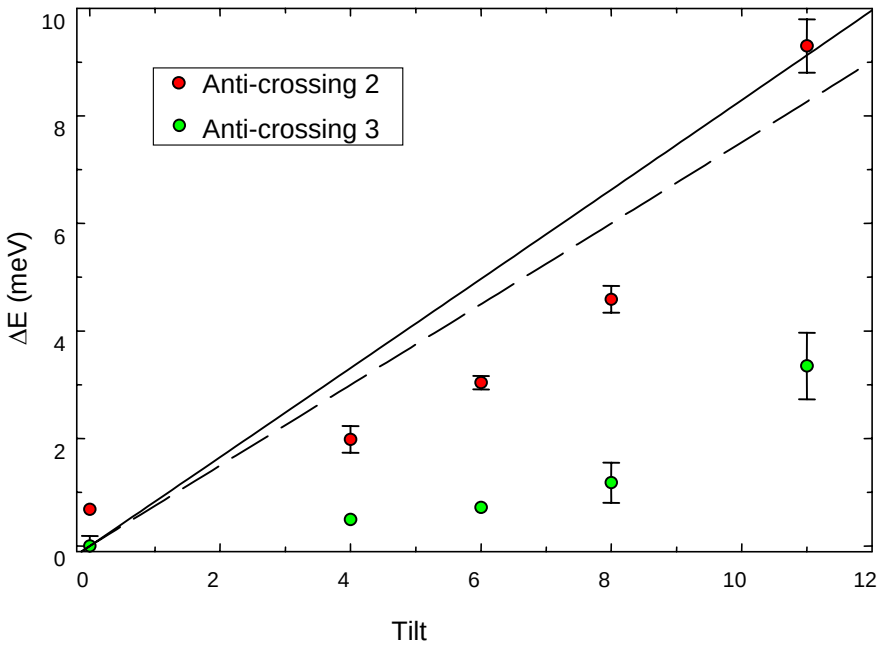

Figure 4.7: Theoretical and experimental results for the energy gap at same-spin anti-crossings for sample s842. The solid line indicates the theoretical energy gap for anti-crossing 3 and the dashed for anti-crossing 2.

than the energy gap for two spin-down Landau Levels (anti-crossing 3). The difference in the theoretical lines for anti-crossings 2 and 3 is due to the non-parabolicity in InSb and the fact that the two anti-crossings occur a slightly different magnetic fields. Also, the theory was calculated using an infinite square well assumption. Finally, although the size of the energy gap for anti-crossing 3 does indeed go to zero for zero tilt angle, as predicted by the theory, the same cannot be said for anti-crossing 2. See Appendix A for data on anti-crossing 2 in sample s702.

4.6 Conclusions

This chapter dealt with the theoretical and experimental results concerning avoided-level crossings that occur between Landau Levels of different subands, but with the same spin. It was observed that the size of the energy gap, ΔE, increases with tilt angle θ, as was previously observed in spin degenerate GaAs experiments [64], whose results agree with Equation 4.10. However, unlike the theoretical predictions and previous experiments, the experimentally determined slope of ΔE vs. θ for us depends on the spin states involved in the avoided-level crossing. Further, again deviating from theory, ΔE did not equal zero for zero tilt for crossing 2, but did seem to for crossing 3. With these considerations in mind, we must conclude that the standard coupling mechanism alone does not accurately describe these crossings. It seems that there is an additional, as yet unknown, effect that influences the characteristics of these anti-crossings.

Chapter 5

Opposite Spin Anti-Crossings

As a complement to the previous chapter on same spin anti-crossings, this chapter will focus on anti-crossings that occur between opposite spin Landau levels from different subbands. Again, in order to study these opposite spin anti-crossings, cyclotron resonance was employed as a probe in the predicted vicinity of the crossings. The analysis of these anti-crossings will consist of a discussion of the size of the resulting energy gap as a function of sample tilt angle. Then, since the theoretical basis discussed in the previous chapter clearly cannot explain coupling between Landau Levels of opposite spin (recall the last term in equation 4.7 requires same spin states), an analysis of some possible coupling mechanisms such as Rashba, Dresselhaus, as well as band non-parabolicity, will be examined. Next, an additional observed splitting, possibly the result of a third subband will be touched upon. Finally, some concluding remarks will be made.

5.1 A Quick Review

Since this chapter is a continuation of the discussion begun in Chapter 4, the sample of interest is again s842. Refer to Figure 4.1 for the sample's layer structure and Figure 4.2 for the resulting energy profile. Of particular interest will

be Figure 4.3, which shows the predicted crossings of interest when the Landau levels from the second subband are considered. However, unlike in the previous chapter, now the concern lies with the opposite spin crossings (crossings 1 and 4 in Figure 4.3).

5.2 Evidence of Spin-Mediated Avoided Level Crossings

As was used to probe the same-spin anti-crossings, cyclotron resonance was again employed as a probe in the predicted vicinity of the opposite spin crossings. The results of this are shown in Figure 5.1. As was seen in the same spin case, and in spite of the theoretical foundation developed in the previous chapter, we again see a clear splitting in the cyclotron resonance traces at the predicted location of opposite spin crossings from the different Landau Levels. This gap can again be more clearly seen by looking at a plot of CR transition position versus B-field. The transitions involved in both same-spin anti-crossings as well as the opposite-spin anti-crossings are shown in Figure 5.2(a). The resulting energy gaps for both anti-crossing types are shown in Figure 5.2(b). For the sample tilted 4^0 with respect to the normal to the B-field direction, a resulting energy gap of approximately 1.5 meV (12 cm^{-1}) is seen for the black transition and a gap of approximately 1.0 meV (8 cm^{-1}) is seen for the blue transition for the opposite-spin anti-crossings. (Note: refer back to Figure 3.5 for a review of which transition was blue and which was black). Also, for now, ignore the anti-

crossing indicated by the yellow circle and arrow. This transition will be discussed in greater detail later in this chapter. For right now, the anti-crossings of interest are indicted by the black and blue arrow and circles in Figure 5.2 (i.e. crossings 1 and 4 from Figure 4.3).

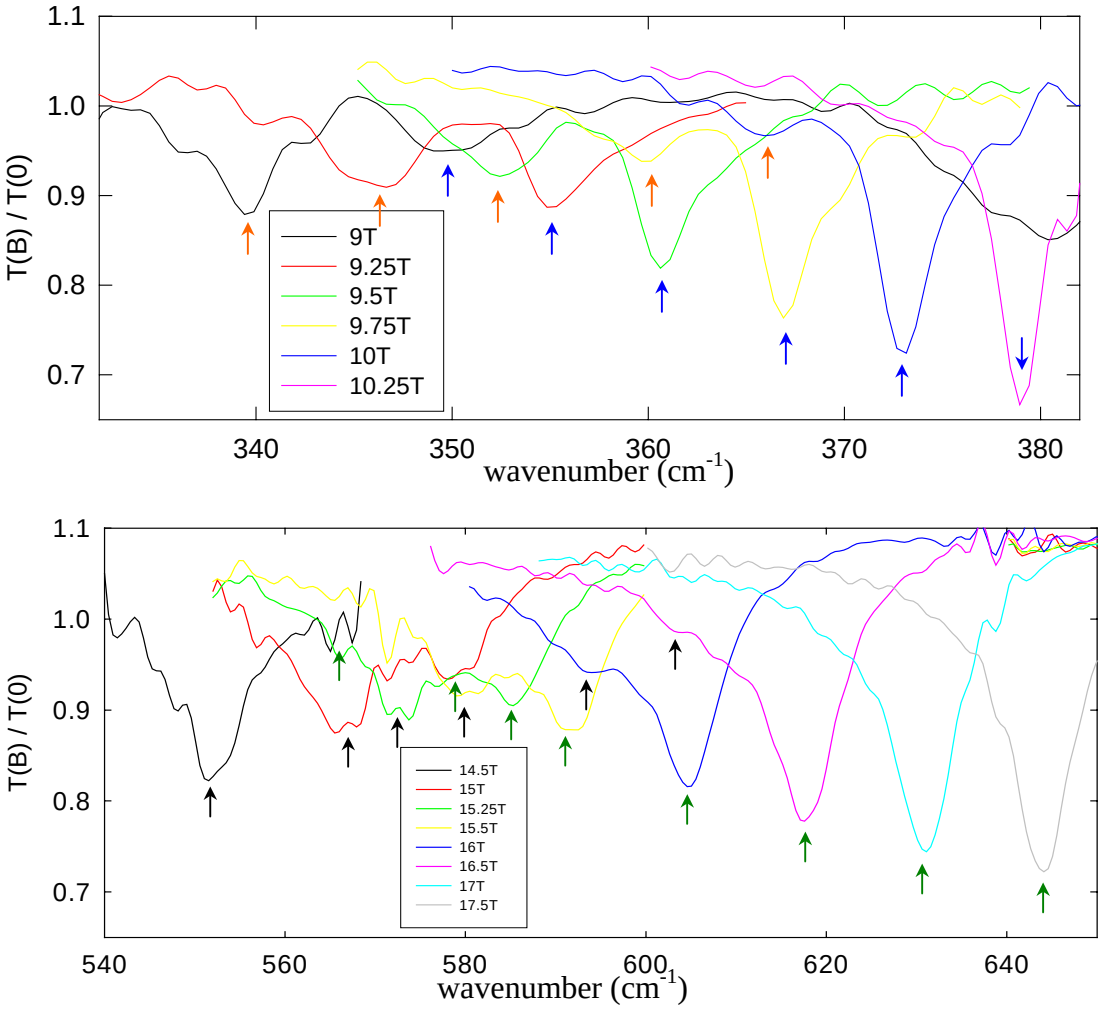

Figure 5.1: Cyclotron resonance traces in the vicinity of the predicted opposite spin crossings for sample s842 at a tilt angle of 4^{o}. Notice that like in the same spin case, a gap in the CR traces is again observed.

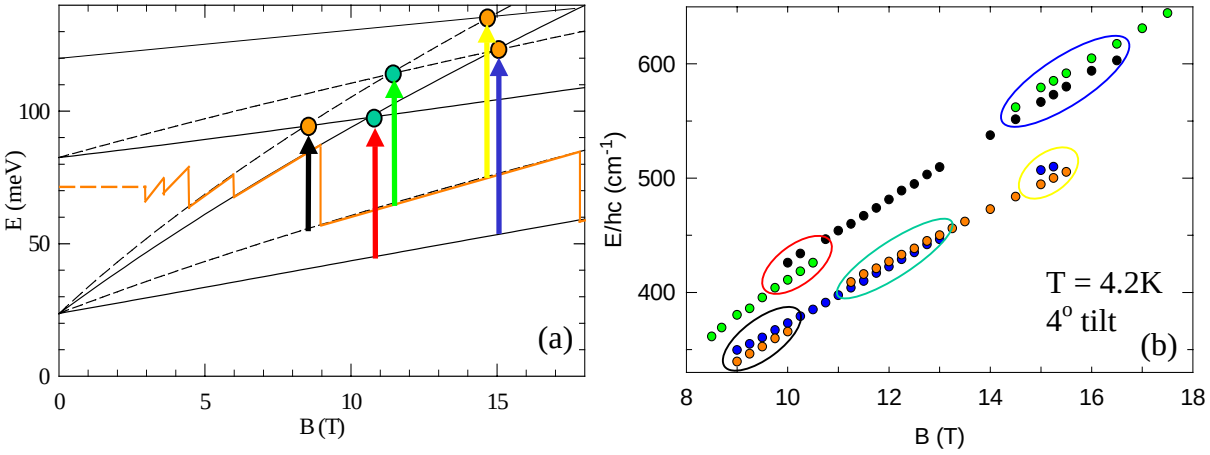

Figure 5.2: (a) CR transitions involved in both the same-spin and opposite-spin anti-crossings for sample s842 at a tilt angle of 4°. (b) Plot of CR transition position vs. B-Field for s842. Notice the clear energy gaps for both same-spin and opposite-spin anti-crossings.

5.3 Tilt Characteristics

In the previous chapter it was observed that the energy gap size for the same-spin anti-crossings was roughly proportional to the sample tilt angle as predicted by the theory. For the observed opposite-spin anti-crossings, however, the same cannot be said. Figure 5.3 shows the tilt dependence of the energy gap for all 4 anti-crossings. From the figure it can clearly be seen that the splitting for the opposite-spin crossings is far less dependent on the tilt than the same-spin crossings. This insensitivity of ΔE on tilt angle for crossings 1 and 4 is consistent with a spin-spin interaction however. In addition, Figure 5.4 shows the positions of the observed anti-crossings in both magnetic field and wavenumber as a

function of sample tilt angle.

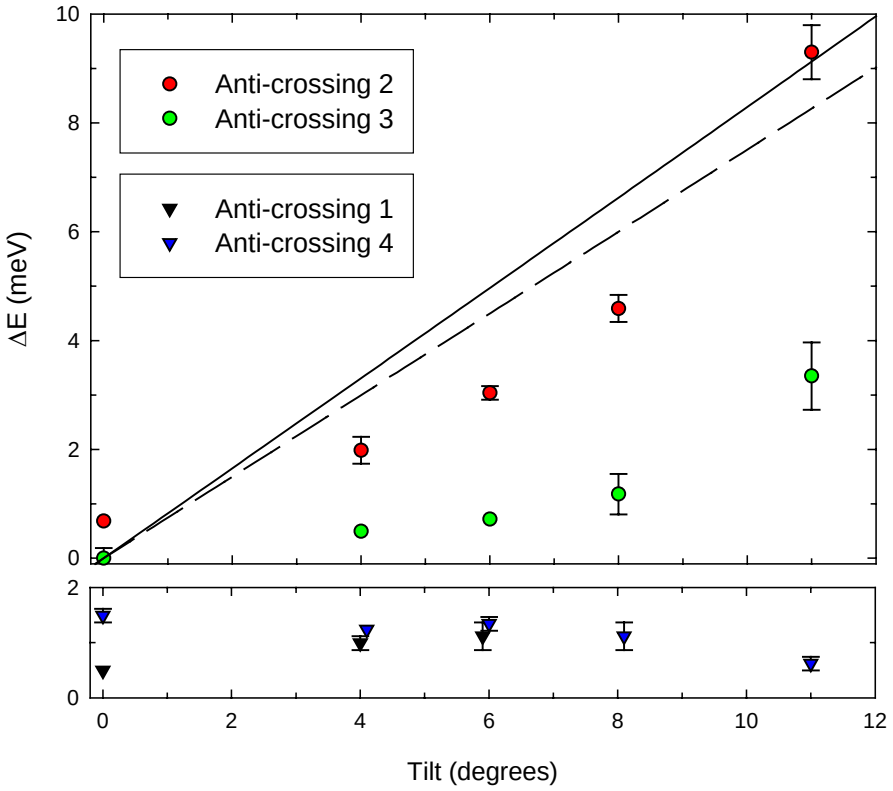

Figure 5.3: Theoretical and experimental results for the energy gap at same-spin and opposite spin anti-crossings for sample s842. Notice how the opposite spin anti-crossings are much less tilt dependent then the same spin anti-crossings.

Taking a closer look at Figure 5.4, one will notice a few interesting features. The first is the unusual behavior of crossings 2 and 3 at a tilt angle of 11^0. This behavior is the result of both anti-crossings growing in size to the point that they begin to overlap and interfere with one another. Second, for anti-crossing 1, only two data points are present due to the AlInSb-like magneto-polaron present at 320 cm^{-1} (see Chapter 3).

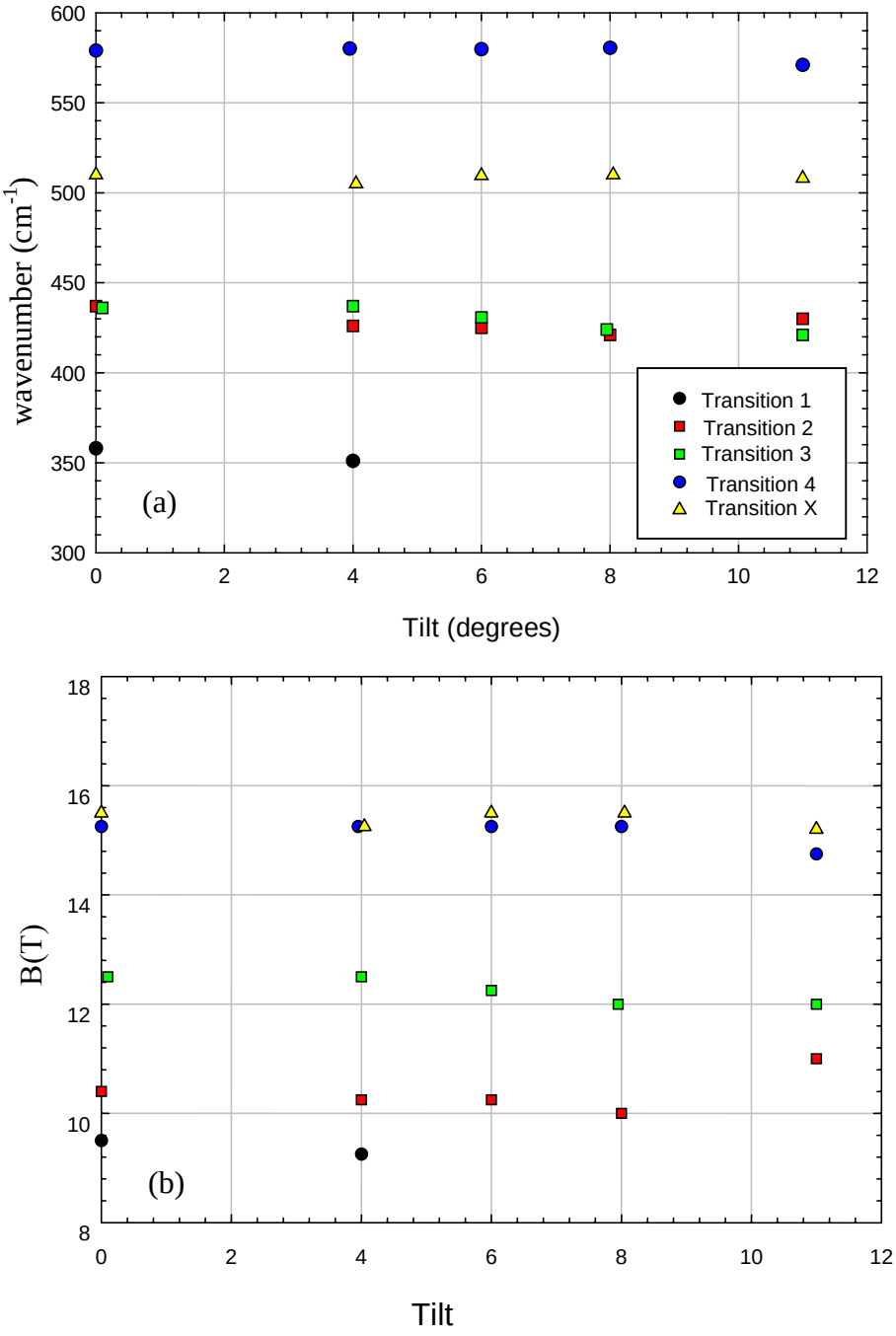

Figure 5.4: Positions of observed anti-crossings for sample s842 in wavenumber (a) and magnetic field (b) versus sample tilt angle.

If one now considers the remaining data points of Figure 5.4, one will notice an overall decrease in the anti-crossing positions as the tilt angle is increased. This shift is explained by Wieck in GaAs [64] as being caused by the diamagnetic shift due to the parallel magnetic field component $B_{\|}$ from Equation 4.6. For reference, the calculated shifts (in meV) for our experiment, as a function of sample tilt angle and magnetic field (in Tesla) are:

$$\left\langle i=1\left|z^2\right|i=1\right\rangle = (4.657x10^{-3})B^2\sin^2(\theta) \tag{5.1}$$

$$\left\langle i=2\left|z^2\right|i=2\right\rangle = (1.0074x10^{-2})B^2\sin^2(\theta) \tag{5.2}$$

However, for our experiment these shifts move the crossings to higher magnetic field, rather than to lower magnetic field, as seen by Wieck. Though, it should be noted that the shift in magnetic field for our crossings was less than 1%.

5.4 Possible Explanations

Clearly, in order to explain the "spin-flip" anti-crossings 1 and 4 that are observed, one needs an additional mechanism to those laid out in the previous chapter. In order to produce these anti-crossings, according to first order perturbation theory, what is needed is a perturbation term that contains three specific components. Those components are: 1) a z or k_z term to couple the subbands together (where **k** is the wavevector), 2) a x or k_x term to couple the Landau levels together, and finally, 3) a σ_x or σ_y term to couple the opposite spin

states. Note, that to explain the opposite-spin anti-crossings, ALL THREE of these terms are necessary. So clearly, the perturbative term given in Equation (4.6) is insufficient.

5.4.1 Rashba and Dresselhaus

As an initial consideration, one should contemplate the usual suspects involved in spin-orbit interactions, the Rashba and Dresselhaus perturbation terms [67, 68, 69]. The Rashba term, H_R arises from the structural asymmetry in the quantum well, while the Dresselhaus term, H_D, has its origins in the lack of inversion symmetry in the structure of the InSb crystal. In the gauge **A =** (0, xB, 0) and with relative strengths α and β, these two terms take on the form:

$$H_R = \alpha\left(\sigma_x k_y - \sigma_y k_x - \frac{e}{\hbar}\sigma_x xB\right) \tag{5.3}$$

and
$$H_D = \delta\left(\sigma_x \kappa_x + \sigma_y \kappa_y + \sigma_z \kappa_z\right) \tag{5.4}$$

where
$$\kappa_x = \frac{1}{2}\left[k_x\left[\left(k_y - \frac{e}{\hbar}Bx\right)^2 - k_z^2\right] + \left[\left(k_y - \frac{e}{\hbar}Bx\right)^2 - k_z^2\right]k_x\right] \tag{5.5}$$

$$\kappa_y = \frac{1}{2}\left[\left(k_y - \frac{e}{\hbar}Bx\right)\left(k_x^2 - k_z^2\right) + \left(k_x^2 - k_z^2\right)\left(k_y - \frac{e}{\hbar}Bx\right)\right] \tag{5.6}$$

and
$$\kappa_z = \frac{1}{2}\left[k_z\left[k_x^2 - \left(k_y - \frac{e}{\hbar}Bx\right)^2\right] + \left[k_x^2 - \left(k_y - \frac{e}{\hbar}Bx\right)^2\right]k_z\right]. \tag{5.7}$$

As can be seen in Equation (5.3), the Rashba term contains the needed x and/or k_x terms, so that neighboring Landau Levels will be coupled, as well as the needed σ_x and/or σ_y terms, coupling opposite spin states. However, the Rashba term clearly lacks the necessary z or k_z terms in order to couple the different subbands.

In order to understand why the Dresselhaus term given in Equation (5.4) fails to satisfy all three necessary conditions one needs to look closely at Equations (5.4) through (5.7). Considering that the expressions for κ_x and κ_y both contain a k_x term but neither possesses a k_z term, it can be seen that the $\sigma_x\kappa_x$ and $\sigma_y\kappa_y$ terms given in Equation (5.4) couple opposite spin states and neighboring Landau levels, but not neighboring subbands. In a similar fashion, since Equation (5.7) for κ_z does possess a k_z term, but does not contain an x or k_x term, the third term in the Dresselhaus term, $\sigma_z\kappa_z$, couples neighboring subbands but not opposite spins nor neighboring Landau Levels. Therefore, one must conclude that neither the Rashba term nor the Dresselhaus can sufficiently explain the observed splitting at crossings 1 and 4.

In addition to the above theoretical considerations concerning the Rashba effect on opposite spin anti-crossings, there also exists experimental evidence that this structural asymmetry effect is not important. By looking at the size of the splittings for both symmetrically and asymmetrically doped samples we observed no increase in the size of splitting 4. This evidence is shown in Figure 5.5.

Clearly, the structural asymmetry built into sample s707 had little to no effect on the size of the energy gap for anti-crossing 4 over its size in the symmetric sample s702. The details of the layer structure for s702 and s707 can be found in Table 5.1. This reinforces the belief that the Rashba effect cannot account for anti-crossings 1 and 4.

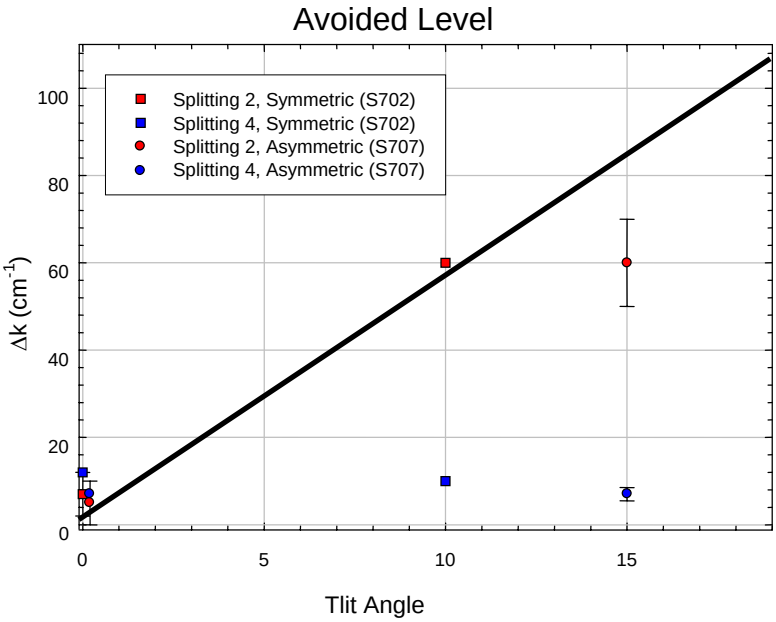

Figure 5.5: Experimental evidence that the Rashba Effect is not important. Notice how the structural asymmetry does not increase splitting 4. The solid line represents the theoretical splitting for crossing 2 in s702.

5.4.2 Band Non-Parabolicity

In addition to the Rashba and Dresselhaus perturbation terms, one should also consider the effects of band non-parabolicity on the Hamiltonian. It has been

shown by Das *et al.* that with the inclusion of band non-parabolicity, several perturbative terms get added to the Hamiltonian [70]. This expanded Hamiltonian is given in Equation 5.8:

$$\begin{aligned} H = {} & a_{11} + a_{12}\,k^2 + a_{13}\,k^4 + a_{14}\left([k_y^2, k_x^2] + [k_z^2, k_x^2] + [k_x^2, k_y^2] \right) + a_{15}\,B^2 + \\ & a_{41}\mu_B\, \boldsymbol{\sigma} \bullet \mathbf{B} + a_{42}\, \boldsymbol{\sigma} \bullet \boldsymbol{\kappa} + a_{43}\, \boldsymbol{\sigma} \bullet \mathbf{B}\, k^2 + a_{44}\, [\boldsymbol{\sigma} \bullet \boldsymbol{\kappa}, \boldsymbol{\sigma} \bullet \mathbf{B}] + \\ & a_{45}\left(\sigma_x B_x k_x^2 + \sigma_y B_y k_y^2 + \sigma_z B_z k_z^2 \right) + a_{46}\, (\boldsymbol{\sigma}\ \mathbf{x}\ \mathbf{k}) \bullet \hat{z} \end{aligned} \tag{5.8}$$

Clearly, the only term of this rather imposing Hamiltonian that will couple opposite spin states, neighboring Landau Levels , as well as subbands is the $a_{44}\,[\boldsymbol{\sigma} \bullet \boldsymbol{\kappa}, \boldsymbol{\sigma} \bullet \mathbf{B}]$ term. This term describes the anisotropic contribution to the g-factor and contains a $k_z(\sigma_x k_x + \sigma_y k_y)$ term. Using a value from the literature for the constant a_{44} for InSb [71, 72], we calculated energy gaps for anti-crossings 1 and 4. These values were 0.022meV for anti-crossing 1 and 0.050meV for anti-crossing 4. Recalling that the observed energy gaps had values of 1.0 meV and 1.5 meV for anti-crossings 1 and 4 respectively, we conclude that band non-parabolicity is not responsible for our observed anti-crossing behavior since the calculated gaps are at least an order of magnitude lower than the observed gaps.

5.5 Third Subband Anti-Crossing

Referring back to Figure 4.2 one will notice that in addition to the second subband at 83meV that has been discussed above, there is also a third subband

bound in the well at 141 meV. If, like before, the Landau levels associated with this third subband are considered, additional crossings will once again be generated. These crossings are shown schematically in Figure 5.6. As can be seen in the figure, the inclusion of the Landau levels from the third subband introduces crossings X and Y and 5 and 6. Like crossings 2 and 3, crossings Y and 5 are same spin crossings, but have a $\Delta i = 2$. Also, like crossings 1 and 4, crossings X and 6 are opposite spin crossings, but also have $\Delta i = 2$. As a reference, crossing X is the same crossing associated with the yellow transition

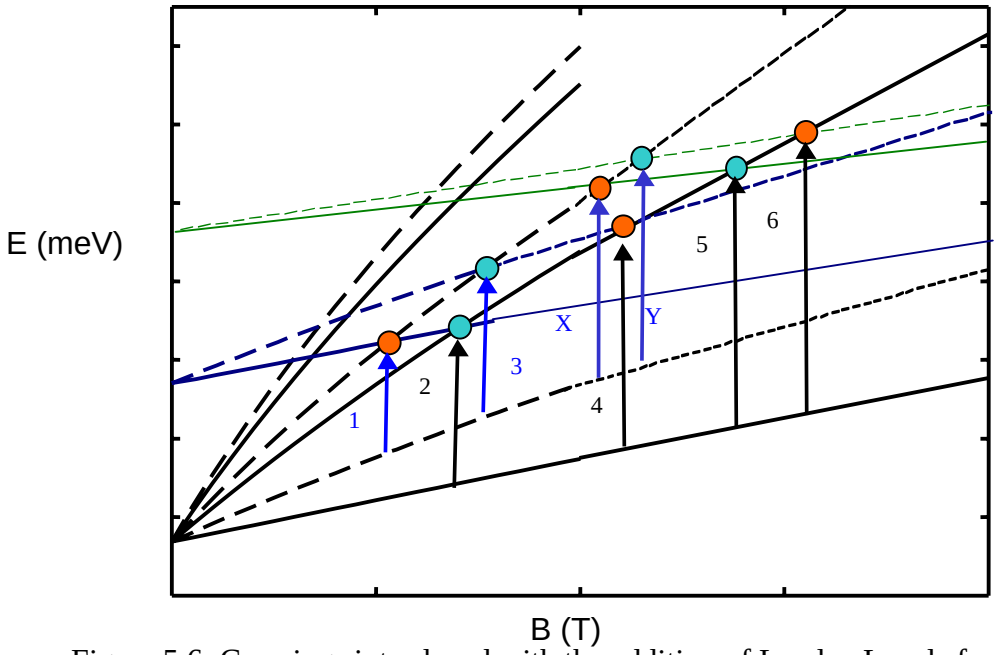

Figure 5.6: Crossings introduced with the addition of Landau Levels from both the second and third subbands. Notice the crossings labeled X, Y, 5 and 6 due to the third subband.

arrow shown in Figure 5.2(a). If one recalls the theory developed back in Chapter 4 (specifically equation 4.7) for same-spin crossings, no anti-crossings are

expected for crossings 5 and Y due to the fact that Δi is even. However, referring back to Figure 5.2(b), an anti-crossing energy gap consistent with crossing X is indeed observed (indicated by the yellow circle in the figure). However, at this point it should be noted that in order to get a proper theoretical fit to the B-field position for crossing X, the subband separation between ground and second excited subband was reduced by 16%. In other words, the ground to second excited subband separation required to fit anti-crossing X is 16% lower than the calculated subband separation for sample s842. Since Δi = 2 for this anti-crossings, a k_z^2 term will be required in the perturbation to explain this observed

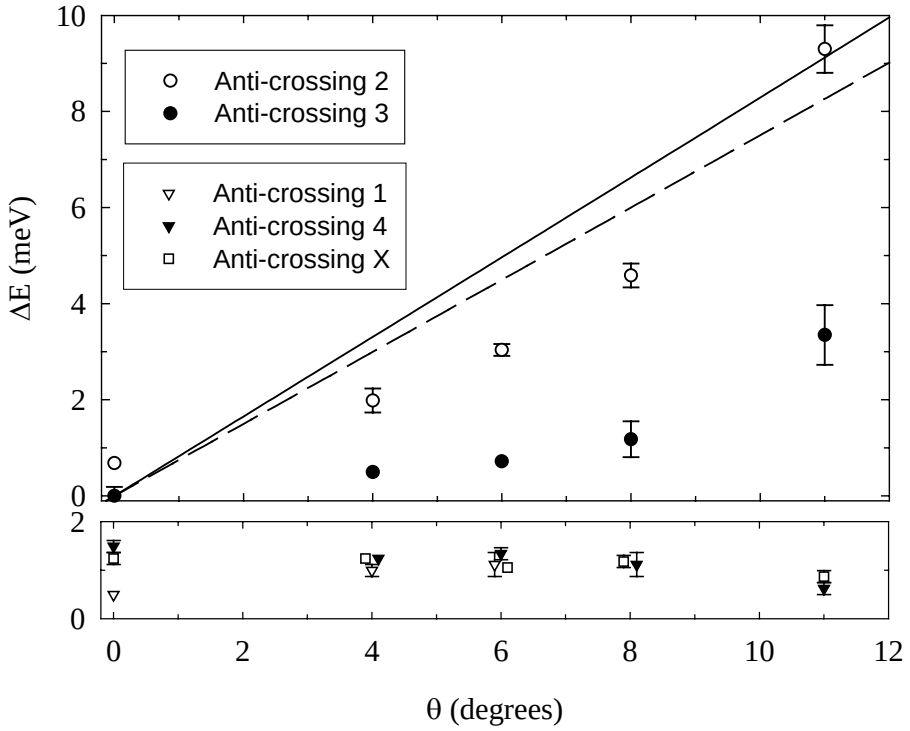

Figure 5.7: Tilt dependence of all five observed anti-crossings. Note how anti-crossing X displays the same apparent tilt independence as the two opposite spin anti-crossings 1 and 4.

energy gap. Clearly, no theory discussed includes such a term. In addition, this X anti-crossing also exhibits the same apparent tilt independence of anti-crossings 1 and 4 as indicated in Figure 5.7. It should also be mentioned that an unusual feature seen high magnetic field in sample s716 might be associated with crossing 6. This feature will be discussed more thoroughly in chapter 6.

5.6 Conclusion

This chapter dealt with the theoretical and experimental results concerning avoided-level crossings that occur between Landau Levels of different subands as well as opposite spin. Clear experimental evidence for such anti-crossings was given. Unlike the observed same spin anti-crossing, it was observed that the size of the energy gap, ΔE, is essentially independent of the tilt angle up to 11^0. Also, it was seen that this energy gap is essentially independent of the structural asymmetry of the sample. Various phenomeon were looked at in an effort to explain these observed opposite spin anti-crossings such as the Rashba and Dresselhaus terms, as well as band non-parabolicity. However, upon looking further at the theory associated each of these, it was determined that none of them can sufficiently explain the observed anti-crossings. Further, an anti-crossing believed to be associated with the Landau levels of the third subband was also

observed. The samples used in this study, along with the relevant sample parameters, and the observed anti-crossings are summarized in Table 5.1. With all of this in mind, we are left wondering what the mechanism is that couples states with opposite spin.

One *possible* mechanism is as follows. In narrow gap semiconductors with large spin-orbit coupling, the strong interaction between the conduction and valence bands leads to a mixing of the electronic states. As a result, the wave functions (with nominal spin polarity and Landau quantum number *n*) contain

Sample Number	Well Width (nm)	Barrier Height (meV)	Tilt (deg)	n_s ($10^{11}cm^{-2}$)	Anti-crossing 1	Anti-crossing 2	Anti-crossing 3	Anti-crossing 4	Anti-crossing X
S707	20	103	0	≈ 2.1	*	6 cm^{-1}	*	8 cm^{-1}	*
S702	20	100	0	≈ 2.8	9 cm^{-1}	4 cm^{-1}	*	11 cm^{-1}	*
S839	25	149	4	≈ 3.9	*	33 cm^{-1}	3 cm^{-1}	11 cm^{-1}	*
S842	25	149	4	≈ 4.3	10 cm^{-1}	14 cm^{-1}	4 cm^{-1}	12 cm^{-1}	10 cm^{-1}
S912	23	154	4	≈ 6	16 cm^{-1}	22 cm^{-1}	6 cm^{-1}	12 cm^{-1}	2 cm^{-1}

Table 5.1: Summary of the samples used in this study. A "*" indicates that the electron density was too low for the i=0, n=0, spin down state to be populated at the B predicted for an anti-crossing. The calculated values for the barrier heights take the $Al_xIn_{1-x}Sb$ composition and strain effects into account.

both spin orientations as well as Landau Level indices *n* and *n*+1 [73, 74, 75]. This mixing of electronic states could account could account for the observed coupling. However, due to the difficulty this type of calculation would entail, it

has not yet been explored. Theoretical investigation of this phenomenon, however, would be a logical next step in the continuation of this work.

Chapter 6

Summary and Future Work

The purpose of this chapter is to summarize the data and results of the previous two chapters and to discuss future improvements on the OU light pipe assembly in order to reduce previous signal-to-noise problems with the OU FTIR experimental setup and further extend this work. A discussion of the positions of both the same spin and opposite spin anti-crossings in B-field for sample s842 will be covered. Specifically, the adjustment of various parameters in the calculated fan diagrams in order to bring the theory more in line with the observed positions will be discussed. This discussion can then be extended to other samples of this study. Also, some possible anti-crossings seen in the data in samples s499, s702, and s716 will be discussed.

6.1 Anti-Crossing Positions in B-field for s842

As was covered throughout chapters 4 and 5, sample s842 clearly showed both same spin and opposite spin anti-crossings. Recall that the growth parameters for sample s842 were a 250 Å well width with a 15% barrier and the sample showed crossings at the following B-field positions:

Crossing 1 → 9.50 T (± 0.25T) Crossing 2 → 10.675 T (± 0.25T)

Crossing 3 → 12.50 T (± 0.25T) Crossing 4 → 15.25 T (± 0.25T)

Note, the crossing position is taken at the B-field where the cyclotron resonance traces on either side of the splitting are of equal intensity (refer to Figure 4.5 and 5.1). However, when the same growth parameters (well width = 250 Å, x = 15%) are used in the creation of a theoretical fan diagram as discussed in Chapter 1, the crossings of interest occur at somewhat different positions in B-field:

Crossing 1 → 7.12 T Crossing 2 → 8.95 T

Crossing 3 → 9.48 T Crossing 4 → 12.50 T

Clearly, the observed and calculated positions for the crossings do not agree within the given uncertainty. However, the question arises as to whether or not the particular growth parameters given are indeed representative of the actual parameters of the sample. In fact, there does exist some uncertainty in the flux rate of the various growth materials in the MBE chamber. This uncertainty in the flux rate is a result of the RHEED calibration technique used in the MBE growth process. This uncertainty could result in a deviation in both the expected well width and barrier concentration of the sample in question. As further evidence of this, x-ray diffraction measurements done on sample s842 indicated an aluminum concentration of 12% in the barrier region rather than the expected 15%.

The result of these considerations is that, in the calculation of the fan diagram for a particular sample, there is some uncertainty in both the well width

and aluminum concentration and that these intended growth parameters are not an absolute. So in order to produce a better fit of the calculated crossing positions to those observed, one needs to calculate multiple fan diagrams, each with different well widths and aluminum concentrations, and see which set of growth parameters best fits the observed crossing positions. Table 6.1 shows the results of such an analysis for sample s842.

s842 (250 Å, 15%)	Crossing 1	Crossing 2	Crossing 3	Crossing 4
observed	**9.5 T**	**10.675 T**	**12.5 T**	**15.25 T**
250 Å, x = 15 %	7.12 T	8.95 T	9.48 T	12.50 T
225 Å, x = 15 %	8.51 T	10.62 T	11.32 T	14.71 T
200 Å, x = 12 %	9.37 T	11.65 T	12.46 T	16.10 T
212 Å, x = 12 %	8.58 T	10.71 T	11.42 T	14.87 T
225 Å, x = 12 %	7.83 T	9.81 T	10.43 T	13.68 T
237 Å, x = 12 %	7.21 T	9.08 T	9.62 T	12.71 T
250 Å, x = 12 %	6.63 T	8.37 T	8.85 T	11.76 T

Table 6.1: Observed and calculated crossing positions for sample s842. Notice how the theoretical crossing positions change as the well widths and barrier concentrations are varied.

Clearly, the theoretical crossing positions vary considerably as the input parameters of well width and aluminum concentration are changed. This, of course, makes sense, since changing these parameters will change the inter-subband spacing, which will in turn, change the position of the predicted crossings.

Another way to compare this theoretical data with experiment is to plot the predicted crossing's B-field position vs. well width for a particular aluminum concentration. Such as plot is shown in Figure 6.1.

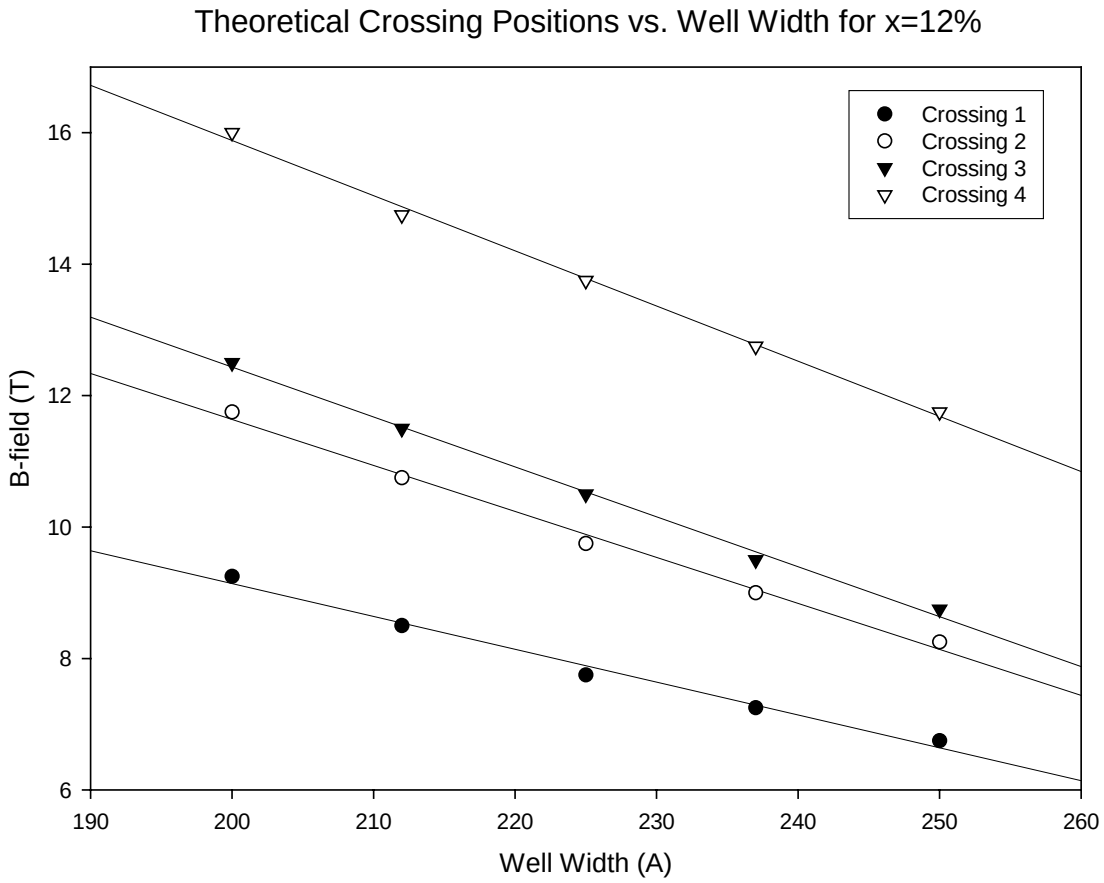

Figure 6.1: Plot of the predicted theoretical crossing positions vs. well width for a sample with an aluminum concentration of 12%.

Note, it is also possible to make a plot of crossing position vs. aluminum concentration for a fixed well width (for example, see such a plot for s702 in Appendix B and the analysis for sample s499 to follow), however, since an x-ray diffraction measurement of x = 12 % was done for s842, the above graph type was

chosen. Extending the idea of Figure 6.1, lines representing the predicted crossings positions can be determined. Now, in order to compare these predicted crossing positions with the observed positions, horizontal lines indicating the observed crossing positions needs to be added to a graph of the lines of the predicted crossings. Such a graph is shown in Figure 6.2.

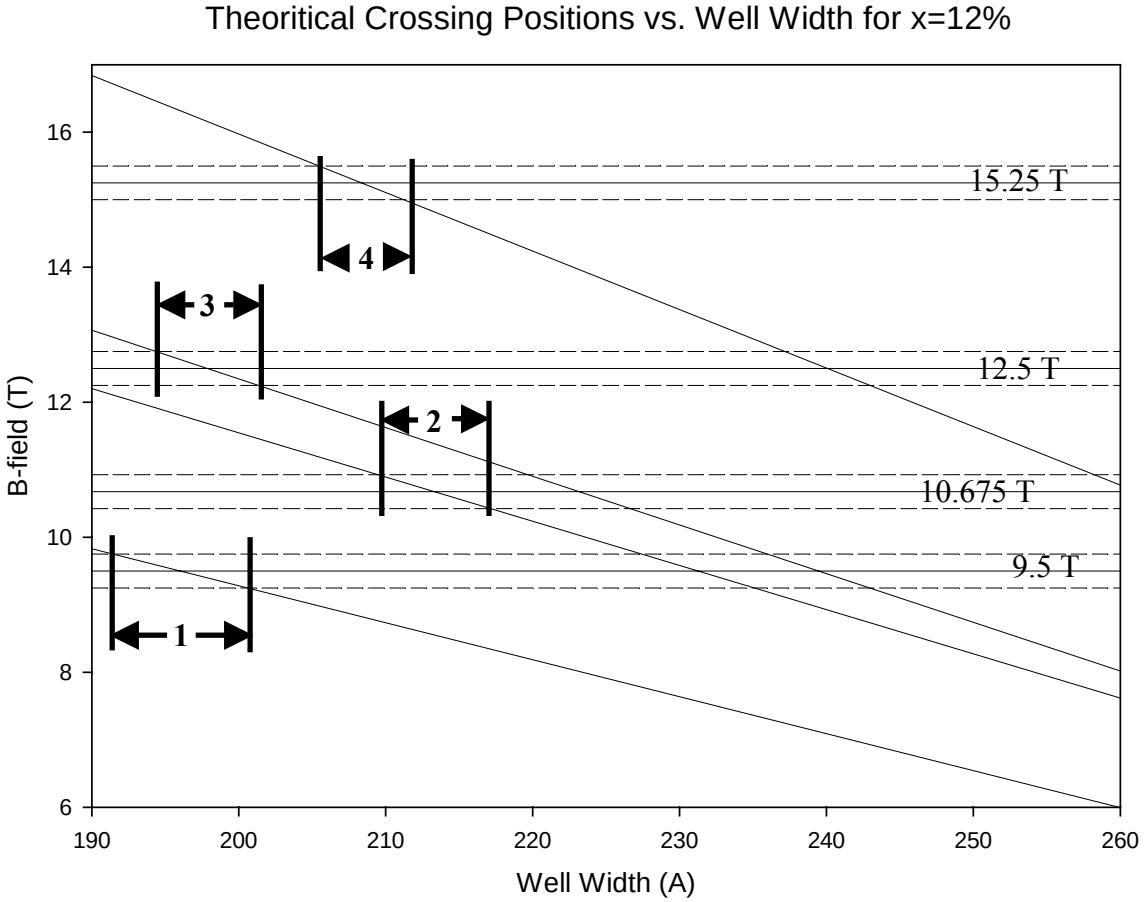

Figure 6.2: Comparison of the theoretical and observed crossing positions for sample s842.

The solid horizontal lines in Figure 6.2 represent the B-fields where the crossings were observed, with the dashed horizontal lines representing the uncertainty. The

angled solid lines represent the theoretical crossing positions one through four (counting from the bottom up) taken from the Landau level calculations. As indicated in the figure, as a result of the ± 0.25T uncertainty in the experimentally determined crossing positions, there exists a range of well widths for which observed and theoretical crossings agree. The bold vertical lines in the figure indicate these regions of agreement for each crossing. Similar table and figures for the other samples studied are given in Appendix B.

As can be seen in Figure 6.2, a theoretical well width of approximately 197 Å will bring crossings 1 and 3 into agreement with the experimental data. However, a well width of approximately 212 Å is required to do the same for crossings 2 and 4. Therefore it must be concluded that, at least for some of the samples of this study, it may not be possible to bring all four predicted crossings into agreement with experiment by only varying the inter-subband spacing (recall that a change in either well width or aluminum concentration affects the inter-subband spacing). So the question arises as to what other theoretical parameters could be adjusted in order to bring the experimental and theoretical results into better agreement. One possibility is the g-factor for InSb.

Previous experiments done here at the University of Oklahoma by G. A. Khodaparast *et al.* [76] show clear electron spin resonance in symmetric samples of both 300 Å, 9% and 200 Å, 9% structures. These results are summarized in Table 6.2.

Sample	Structure	Δ_s (meV)	B-field (T)	n
s644	300 Å, 9 %	6.74	3.35	1
s377	300 Å, 9 %	10.43	6.1	1
s716	300 Å, 9 %	12.86	5.67	0
s716	300 Å, 9 %	7.61	3.95	1
s710	300 Å, 9 %	10.43	4.35	0
s372	300 Å, 9 %	6.74	4.05	2
s704	200 Å, 9 %	6.74	3.35	1
s704	200 Å, 9 %	10.43	4.1	0
s704	200 Å, 9 %	12.86	5.58	0

Table 6.2: Summary of electron spin resonance data for symmetrically doped samples gathered at the University of Oklahoma. n = Landau Level index and Δ_s = spin splitting.

If, however, this data is plotted along with the spin splitting energies calculated and used in the previous theoretical Fan Diagrams one will see that the agreement is less than superb, as can be seen in Figure 6.3. Clearly, the theoretical spin splitting needs to be increased in order to bring the theory into better agreement with the experimental observations. It was found that by increasing the g-factor by approximately 15% for the 300 Å samples and by 23 % for the 200 Å samples, much better agreement between the predicted and experimental spin splitting was achieved, as Figure 6.4 shows.

However, in increasing the spin splitting as discussed above, one might wonder if the previous fittings for the cyclotron resonance positions vs. magnetic field are affected? Recall from Figures 3.8 and 3.9 that good agreement was

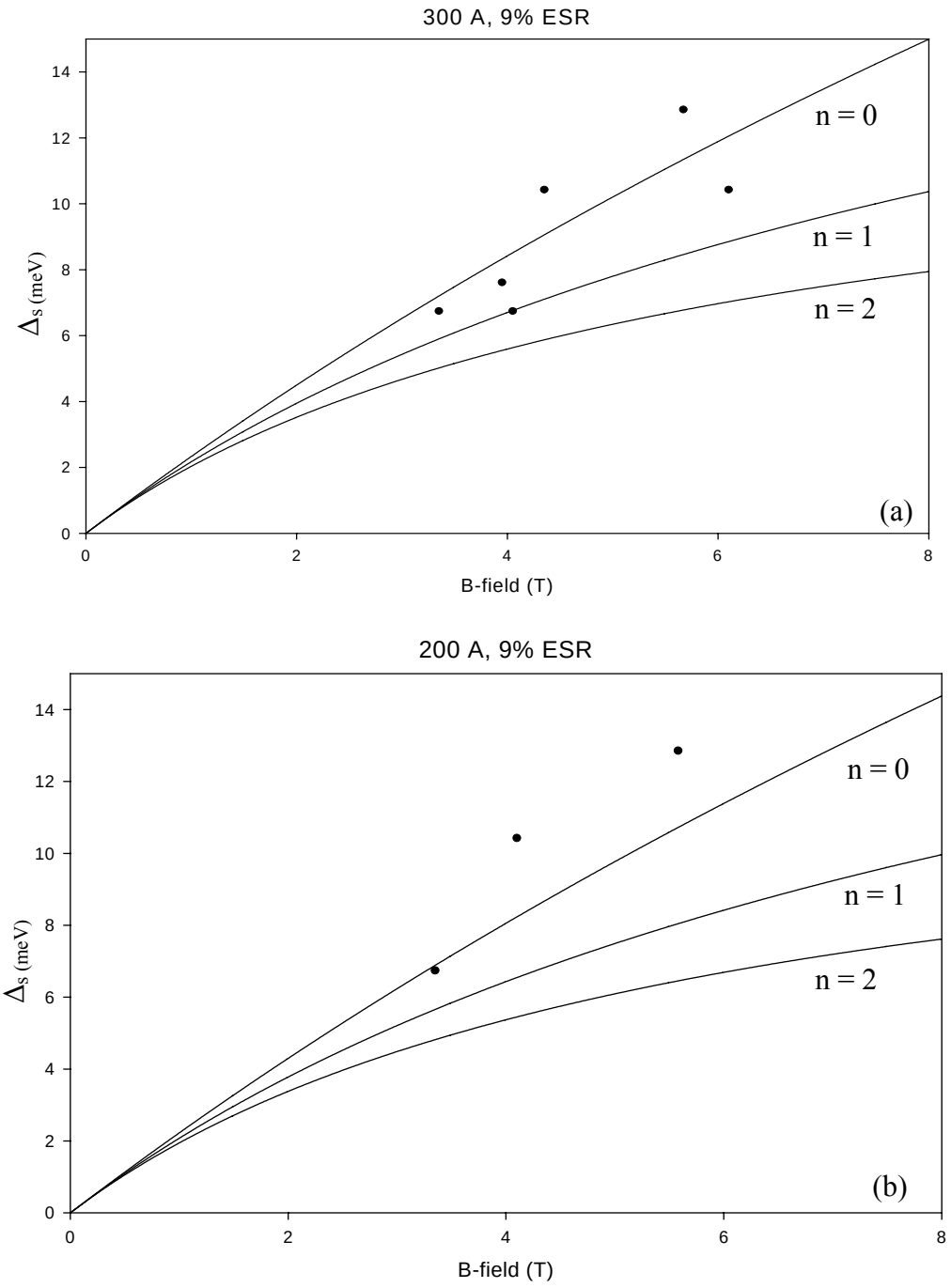

Figure 6.3: Electron spin resonance data for 9% barrier samples with well widths of (a) 300Å and (b) 200 Å. Solid lines represent the theoretical spin splitting for each Landau Level.

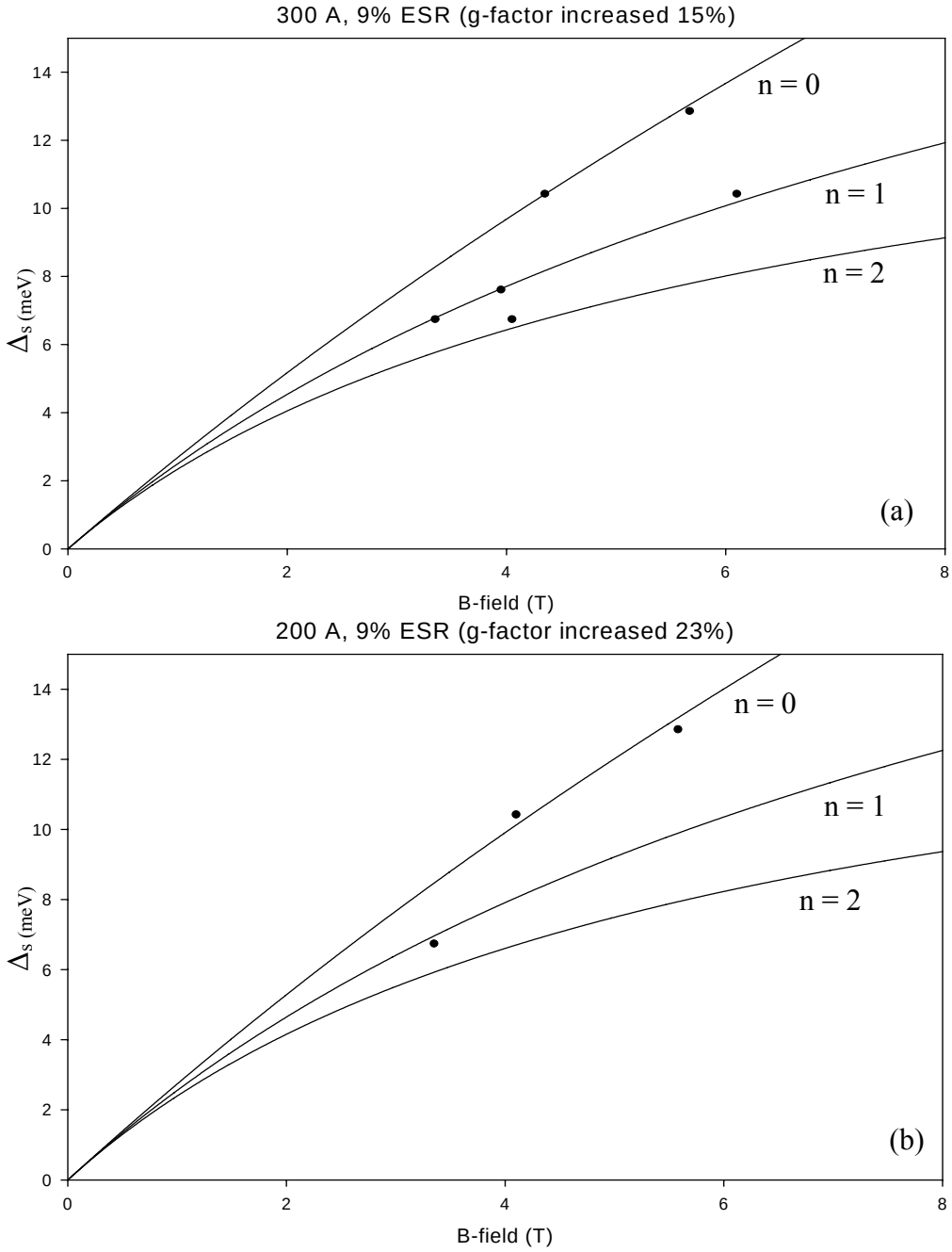

Figure 6.4: Electron spin resonance data for 9% barrier samples with well widths of (a) 300Å and (b) 200 Å. Solid lines represent the theoretical spin splitting for each Landau Level. The g-factor used in the calculation of the theory lines has been increased 15% for the 300 Å samples and 23% for the 200 Å samples.

previously achieved between the theoretical and experimental cyclotron resonance positions vs. magnetic field for all the samples of this study. Is this agreement maintained when the spin splitting is increased in order to bring the experimental and theoretical ESR data into agreement as discussed above? Figure 6.5 shows cyclotron resonance data for sample s716 (300 Å, 9%) both before and after the g-factor was increased by 15%. As one can clearly see in the figure, the positions of the colored theoretical cyclotron resonance lines do indeed change with the change in g-factor, however this change is only minor. Thus, increasing the g-factor, even by as much as 15 %, has little effect on the predicted cyclotron resonance positions, and the previous agreement with the experimental data is maintained.

Finally, will the increase in the g-factor affect the predicted positions of crossings 1 - 4? Before the increase, the theoretical calculation of the Fan diagram for a 300 Å, 9% sample produces the following crossing positions:

Crossing 1 → 4.53 T Crossing 2 → 5.80 T

Crossing 3 → 6.07 T Crossing 4 → 8.32 T

After a 15 % increase in the g-factor, these predicted positions become:

Crossing 1 → 4.37 T Crossing 2 → 5.78 T

Crossing 3 → 6.09 T Crossing 4 → 8.82 T

Interestingly, increasing the g-factor moves crossing 1 down, has essentially no effect on the positions of crossing 2 and 3, and moves crossing 4 up. In order to

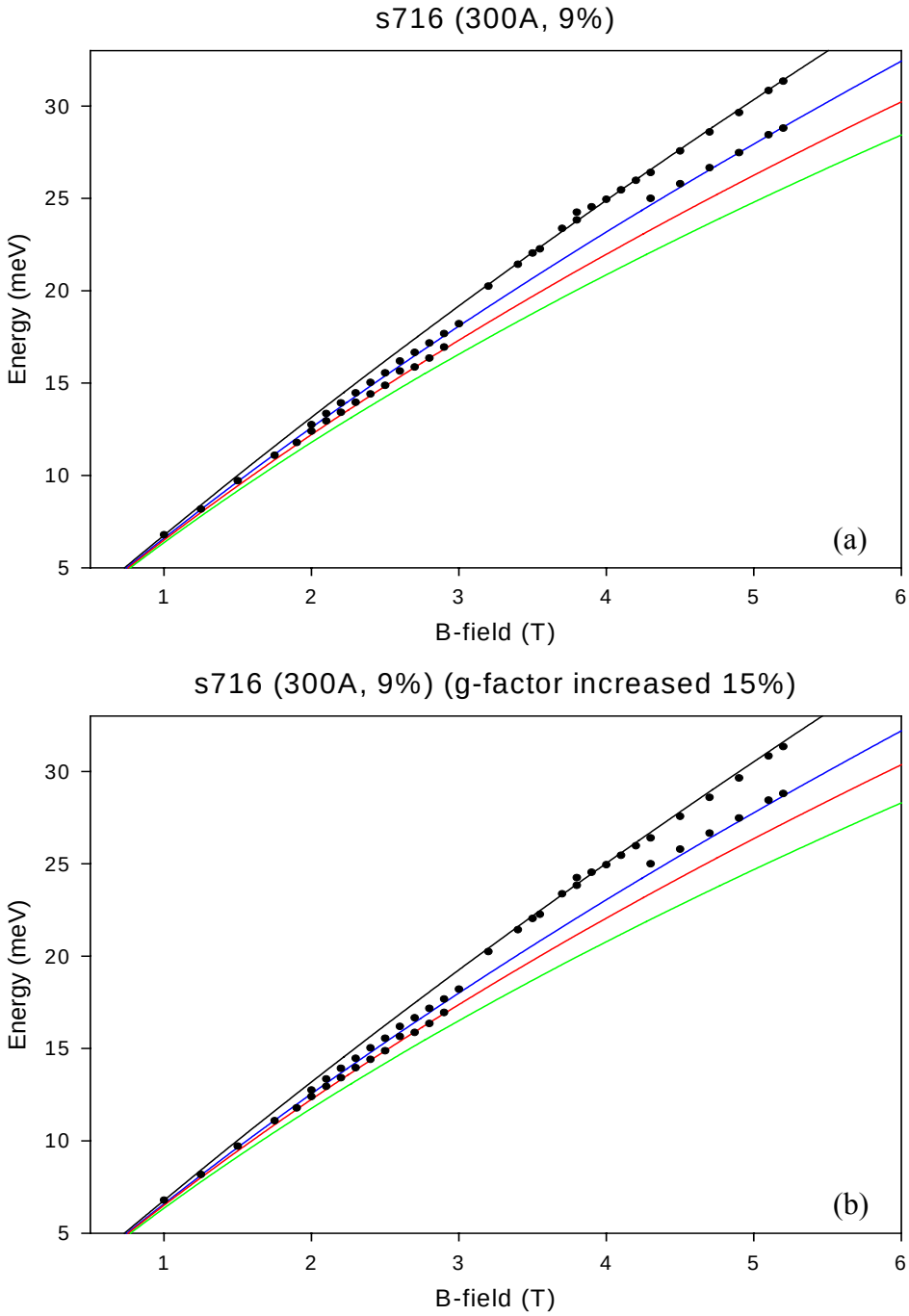

Figure 6.5: Comparison of experimental and theoretical cyclotron resonance data for sample s716 (a) before and (b) after the g-factor was increased 15%. Notice how the colored predicted transition lines change only slightly with this increase.

understand these shifts, it necessary to consider the specific spin-split Landau Levels that define each crossing (refer to Figure 4.3) and how these levels change with an increased g-factor. For example, consider crossing 1. Crossing 1 occurs between (a) the n = 1, spin down Landau Level of the lowest subband and the (b) n = 0, spin up Landau Level of the first excited subband. Thus, increasing the g-factor will move (a) up and (b) down. Both of these changes contribute to moving Crossing 1 to lower magnetic field. In contract, Crossing 2 occurs between (a) the n = 1 spin up Landau Level of the lowest subband and the (b) n = 0, spin up Landau Level of the first excited subband. Increasing the g-factor will move both of these states down, resulting in almost no change in the position for the crossing. A similar line of reasoning can be applied to crossings 3 and 4 to understand their change in magnetic field position as the g-factor is increased.

So with these changes in mind, consider the predicted positions of crossings 1 – 4 for sample s842 with an increased g-factor. Recall that the well width for sample s842 is approximately 250 Å. Further, recall that in order to produce good agreement to the ESR experimental data, the g-factor was increased 15 % for the 300 Å samples and 23 % for the 200 Å samples. Thus, since the well width for sample s842 falls in between these other values, it seems reasonable to average their g-factor increases and reproduce the previous analysis for sample s842 with a g-factor increase of 19 %. The results of such an analysis are summarized in Table 6.3.

s842 (g-factor ↑ 19%)	Crossing 1	Crossing 2	Crossing 3	Crossing 4
observed	**9.5 T**	**10.675 T**	**12.5 T**	**15.25 T**
200 Å, x = 12 %	8.97 T	11.59 T	12.54 T	17.09 T
212 Å, x = 12 %	8.21 T	10.66 T	11.49 T	15.81 T
225 Å, x = 12 %	7.49 T	9.76 T	10.49 T	14.58 T
237 Å, x = 12 %	6.90 T	9.03 T	9.68 T	13.56 T
250 Å, x = 12 %	6.34 T	8.33 T	8.90 T	12.58 T

Table 6.3: Observed and calculated crossing positions for sample s842 after a g-factor increase of 19%. Compare the results to Table 6.1.

As was done before for sample s842, the above table can be used in conjunction with the observed positions for crossings 1 – 4 to produce Figure 6.6.

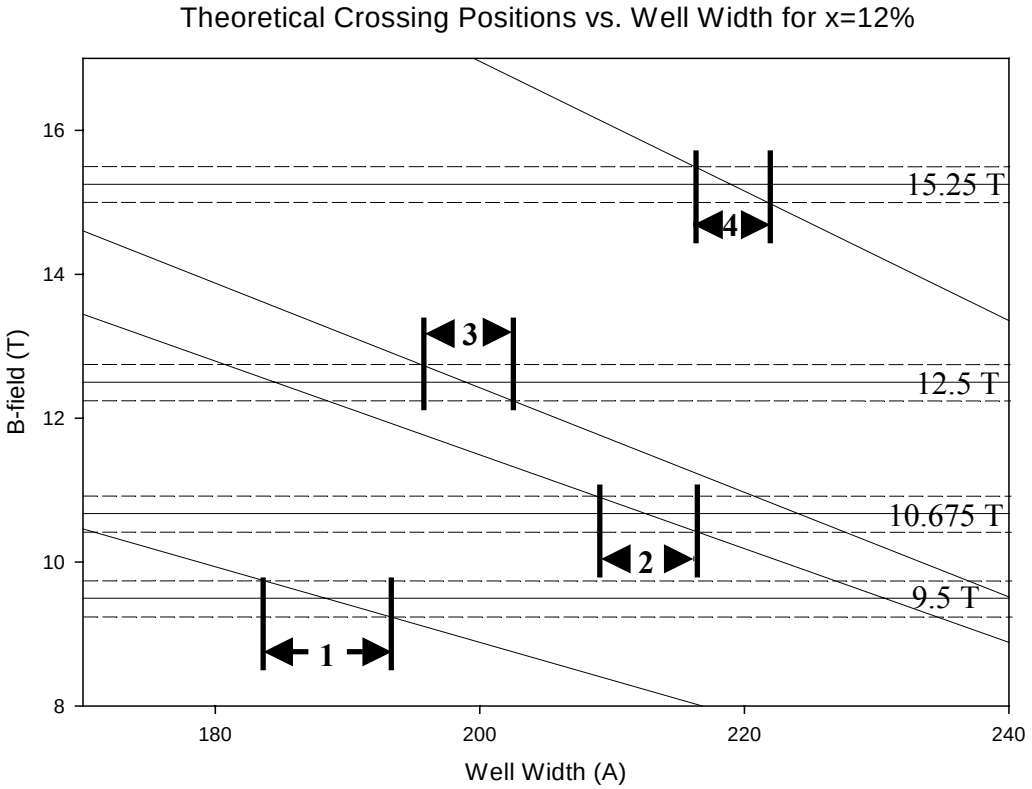

Figure 6.6: Comparison of the theoretical and observed crossing positions for sample s842 after a g-factor increase of 19%.

Unfortunately, as can be seen in the figure, the increase in g-factor actually removes the agreement that was previously seen between crossings 1 and 3 and between crossings 2 and 4. Thus, for sample s842, such an analysis is not successful in bringing the theoretical predictions and experimental data into better agreement.

For the other samples of this study (see Appendix B), the results of increasing the g-factor as was done for s842 are mixed. Recall from the above discussion that increasing the g-factor will move crossing 1 down in magnetic field, essentially leave crossings 2 and 3 where they are, and move crossing 4 to higher magnetic field. So for sample s702 (see Figure B1 and B2 in Appendix B), increasing the g-factor improves the agreement between crossings 2 and 4. However, for samples s839 and s912 (Figures B3 and B4 in Appendix B) increasing the g-factor will degrade the agreement seen in those samples. Thus, it is unclear whether or not increasing the g-factor is an aid in bringing theory and experiment into agreement. However, it can be concluded from this analysis that changing the g-factor is another theoretical parameter that can be used in an effort to bring the theoretical predictions and experimental data into better agreement.

Yet, is increasing the g-factor at all even justified? It has been noted by E. J. Johnson and D. H. Dickey [79] that both the mass and g-factor have remote-band contributions. These contributions have not been taken into account in the previous calculation of the Fan diagrams. These contributions will indeed

increase the g-factor, however, when the calculation is carried out, the remote-band contributions only increase the g-factor by 8 %. This is clearly significantly lower than the 15 – 23% used earlier to bring the previous ESR data into agreement with our calculations.

6.2 Return to Samples s499, s702, and s716

Recall that in Chapter 3 there were some possible avoided level crossings in samples s499 and s702 that, up to this point, remain unidentified.

In the data for sample s702 recall that it was determined that several possible crossings in the low magnetic field region were in fact simply the result of the considerable amount of noise in the measurement for that sample, and not due to any avoided level crossings. The reasoning behind this conclusion will now be explored.

Referring back to Figure 3.12, several possible transitions, which could indicate an avoided level crossing, were identified. However, several of these possible transitions could also be simply artifacts of the noise in the measurement. Nonetheless, if these possible transitions are indeed real and do indicate an avoided level crossing, which crossings could they be? Could the possible avoided level crossings seen in the blue and back transitions in Figure 3.12 be the result of crossings 1 - 4 discussed in Chapters 4 and 5? Referring to Table B1 in Appendix B for sample s702 one will see that by varying the structural parameters

for sample s702 the lowest predicted crossing occurs at 6.52 Tesla, well above the possible avoided level crossings seen in Figure 3.12. Also, for sample s702, crossings 2 and 4 have already been associated with splittings in the cyclotron resonance that occur at 10.875 Tesla and 16.0 Tesla, respectively, as seen in Figure 6.7. Therefore, the possible splittings in the lower magnetic field region

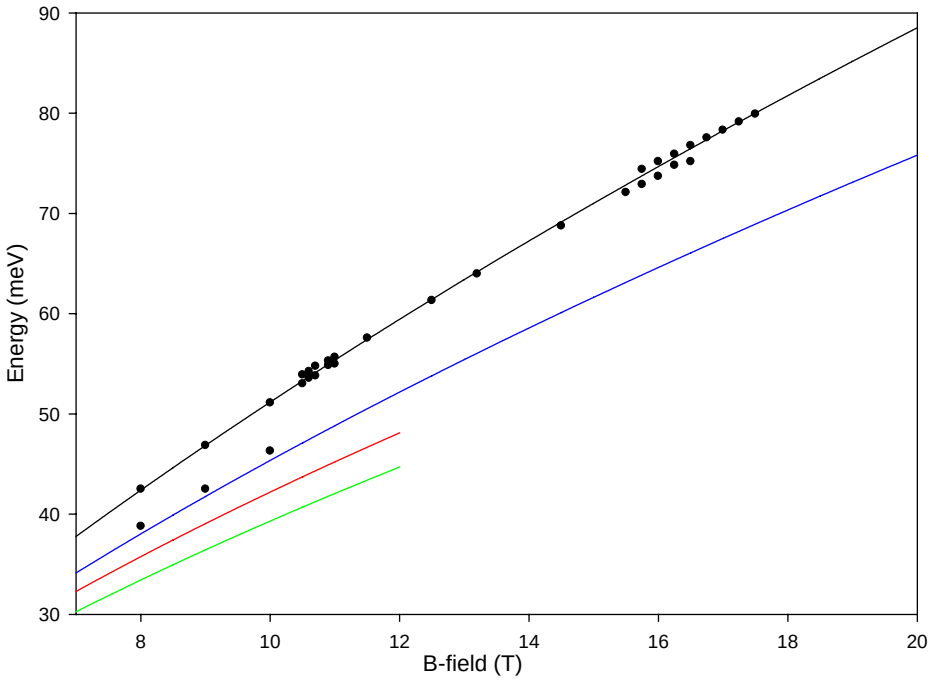

Figure 6.7: Cyclotron resonance data for sample s702 showing crossings 2 and 4 occurring at 10.875 Tesla and 16.0 Tesla respectively.

that occur in the black and blue transitions for sample s702 clearly cannot be the result of crossings 1 – 4.

Although the possible avoided level crossings seen in the low field data for sample s702 are clearly not due to crossings 1 – 4, another possibility exists. Recall that crossings 1 – 4, as identified in Figure 4.3, are the crossings that occur

between the spin split, n = 1 Landau Levels of the lowest subband and the spin split, n = 0 Landau Levels next highest subband. However, again referring to Figure 4.3, one will notice that additional crossings also occur between the spin split, n = 2 Landau Levels of the lowest subband and the spin split, n = 0 Landau Levels of the next subband. These additional crossings are identified by Wieck *et al.* [64, 80] as half-field (or r = 2) crossings because they tend to occur at half the energy of crossings 1 – 4. It is also important to note that, due to the nature of these crossings, they can only produce splittings in the cyclotron resonance traces associated with the red and green transitions.

So can the possible splittings in the red and green transitions as seen in Figure 3.12 be due to these half field crossings? Consider the Landau Level plot for sample s702 shown in Figure 6.8. In this figure it is clear that the half field crossings occur between approximately 4 and 6 Tesla. However, referring back to Figure 3.12, the possible avoided level crossings in the red and green transitions occur between 3 and 4 Tesla. Thus, the previous conclusion in chapter 3 that there are no avoided level crossings in sample s702 at low field seems reasonable. Thus Figure 3.12 becomes Figure 3.13, with the expected non-split cyclotron resonance transitions black, blue, red and green.

Next, consider the apparent avoided level crossings that occur in the black and blue transitions of sample s499 shown in Figure 3.8 (also, see spectra for s499 in Appendix A). Again, identifying the positions of these crossing as the B-field

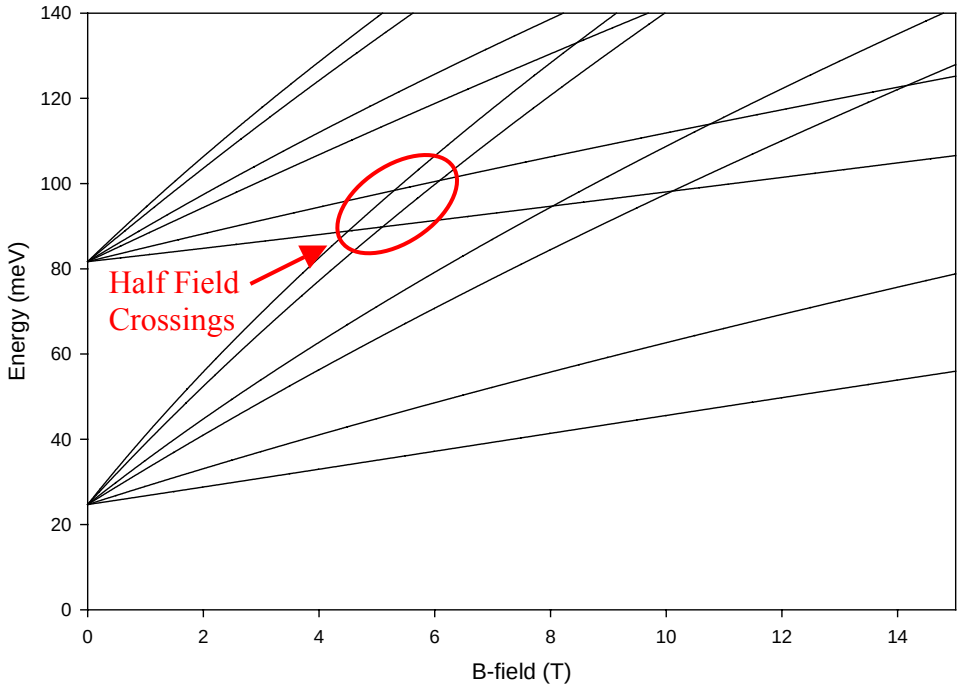

Figure 6.8: Landau Level plot showing the position of the half field crossings for sample s702.

where the cyclotron resonance traces on either side of the splitting are of equal intensity, the crossing in the black transition occurs at 4.9 Tesla and the crossing in the blue transition occurs at 5.05 Tesla. Also, since these crossings occur in the black and blue transitions, as discussed above in the analysis for s702, they cannot be the result of the half field crossings discussed by Weick.

In an effort to identify the origin of these crossings, a Landau Level plot for the growth parameters for s499 was generated. The intended growth parameters for s499 are a well width of 300 Å and an aluminum concentration of 9% in the barrier. This Landau Level plot predicts crossings at the following positions:

Crossing 1 → 4.53 T Crossing 2 → 5.80 T

Crossing 3 → 6.07 T Crossing 4 → 8.32 T

Considering the fact that the crossing in the black transition occurs slightly before the blue crossing, as well as the fact the crossings occur very close to one another in magnetic field, it seems like predicted crossings 2 and 3 are the most likely candidates to explain the experimental results. However, each predicted crossing is about one Tesla too high. Thus, like in sample s842, as well as the other samples of this study, the parameters of well width and aluminum concentration were varied and used to generate multiple fan diagrams for this sample. First consider leaving the well width at 300 Å and varying the aluminum concentration. This type of analysis leads to Figure 6.9. Unfortunately, as can be seen in the figure, in order to fit the predicted crossings to the experimentally observed positions, and aluminum concentration of approximately 5 % is required. This low a level of aluminum concentration is well outside the uncertainty due to the sample growth RHEED calibration mentioned previously. Also, x-ray diffraction measurements done on sample s499 indicate and aluminum concentration of 8.5 – 9 %, so 5% is simply too low to be reasonable.

As the above analysis indicates, varying the aluminum concentration for sample s499 is not a viable method to bring the predicted and observed crossings positions into agreement. However, performing a similar analysis, this time

leaving the aluminum concentration at 9 % and varying the well width, Figure 6.10 is generated.

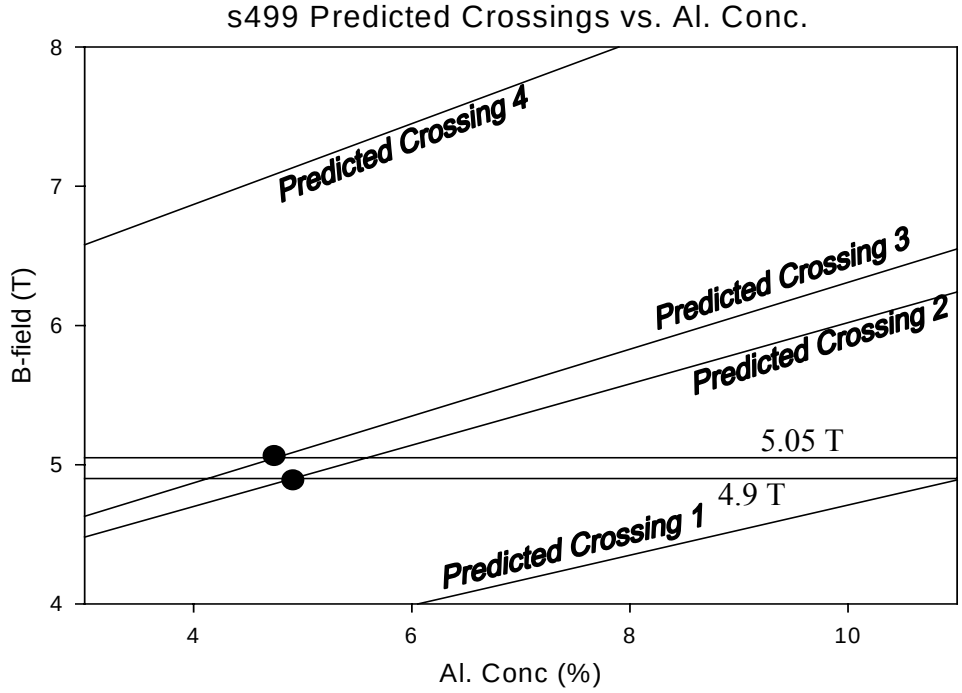

Figure 6.9: Plot of the predicted theoretical crossing positions vs. aluminum concentration for a 300Å well width sample. Observed crossings are those for s499. Notice how an Al conc. of 5 % is required for agreement.

As Figure 6.10 indicates, with a well width of approximately 322 Å, there is good agreement with the theoretical and experimental results. Also, the difference of 22 Å between the intended well width and the width needed to get this agreement is within the uncertainty of the MBE growth process (a thickness uncertainty of approximately ± 10 %). Thus, it does appear that the observed crossings in the black and blue transitions seen in Figure 3.8 for sample s499 are indeed crossings 2 and 3 as speculated earlier.

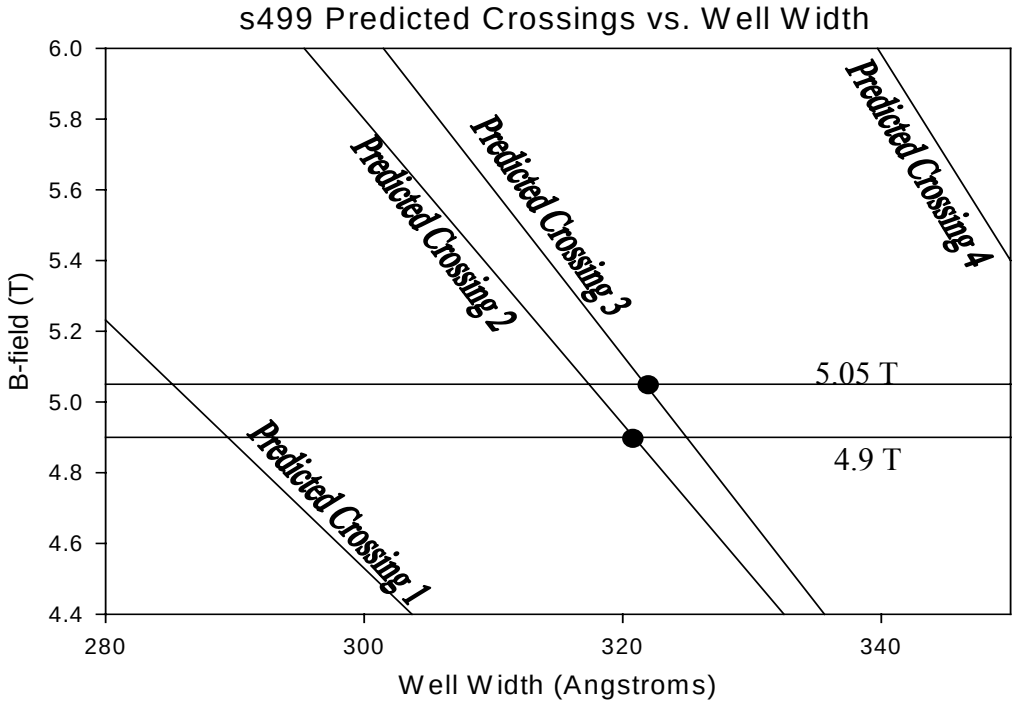

Figure 6.10: Plot of the predicted theoretical crossing positions vs. well width for a 9% Al. conc. sample. Observed crossings are those for s499. Agreement with experiment is achieved for a well width of approx. 322 Å

Given the identification of the crossings seen in the experimental data for s499 with the predicted crossings 2 and 3 the question arises as to whether or not crossings 1 and 4 can also be seen in the data at the magnetic fields predicted by a well width of 322 Å? The predicted positions for crossings 1 and 4 for a sample with a 322 Å well and an aluminum concentration of 9% are approximately 4 Tesla and 7 Tesla respectively. Unfortunately, for sample s499 these magnetic fields would place these crossings near the InSb magneto-phonon energy and the GaAs substrate phonon window discussed in Chapter 3 (see specifically Figure 3.6). That is why these crossings are not observed in this sample. Also, for a

sample with s499's structure, the predicted positions for the half field crossings are between 2.5 and 3.5 Tesla. Unfortunately, the resolution of the scans (approximately 2 cm^{-1}) coupled with the fact that the lowest magnetic field scan taken with this sample was 2.8 Tesla, could explain why these crossings were not observed.

And finally, there exists an unidentified feature in the data gathered from sample s716 that merits further discussion. Although not definitively identified as an avoided level crossing, the cyclotron resonance data for s716 associated with the blue transition shows a clear decrease in intensity in the three to four Tesla range (approximately 160 to 180 wavenumbers) as Figure 6.11 shows. As discussed above, this feature cannot be the result of one of Weick's half field crossings because it occurs in the cyclotron resonance associated with the blue transition. Also, like the samples discussed above, the magnetic field at which this feature occurs is too low to be explained by crossings 1 through 4. However, unlike the data for s702, the feature in s716 is quite clear and not likely the result of noise in the experiment.

Likewise, other unusual features have been seen by Schlesinger *et al.* [77] in GaAs and again by S. Syed *et al.* [78] in GaN samples. Although no explanation has been arrived at concerning these unusual features, it is interesting to note that the data gathered by both groups seems to follow an $E \propto \sqrt{n}$ relationship as indicted in Figure 6.12. More specifically however, the

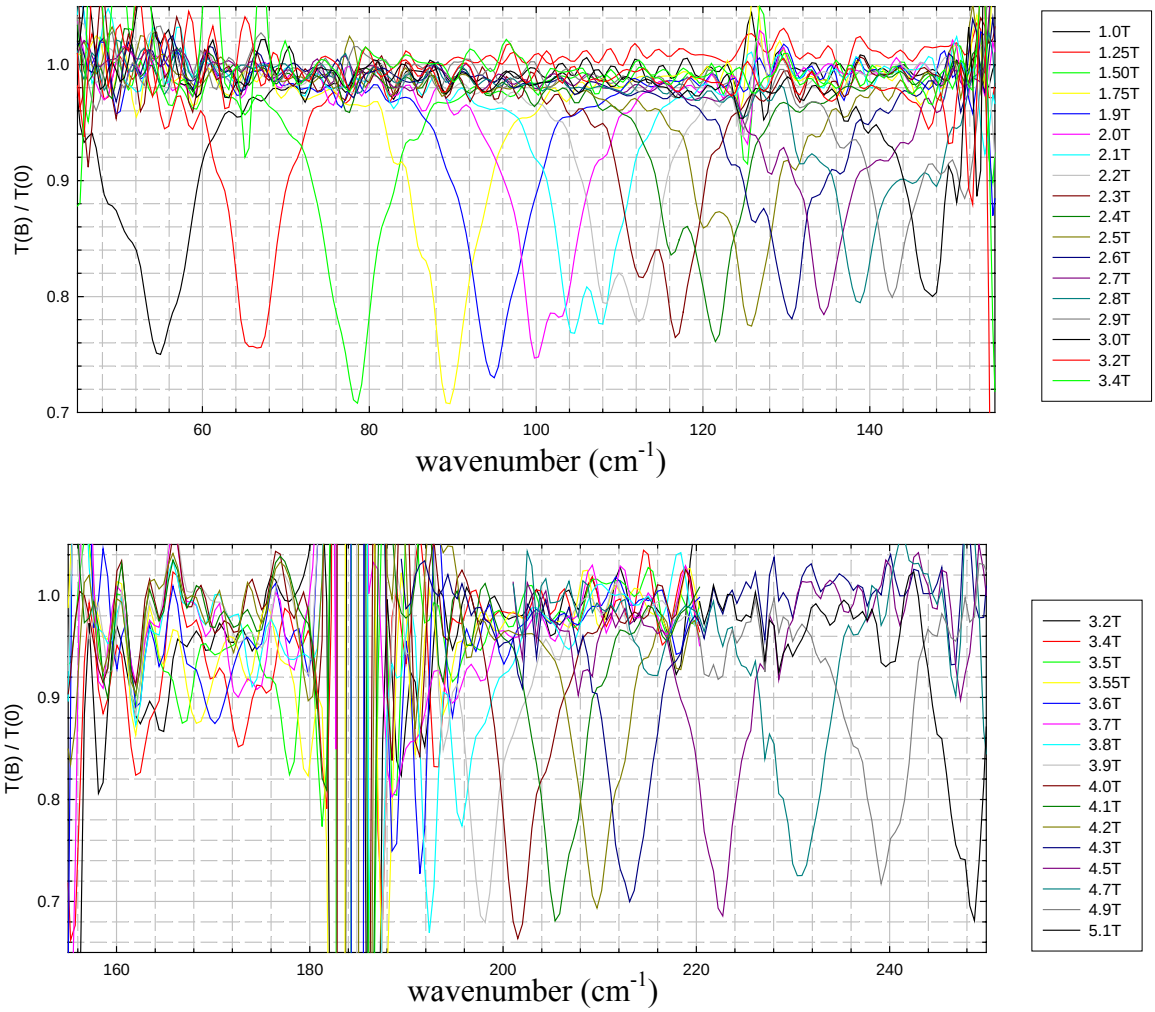

Figure 6.11: Cyclotron resonance data for sample s716 showing a curious drop in the transition intensity between 160 and 180 wavenumbers

data gathered by Schlesinger follows an $E = \frac{\sqrt{n}e^2}{\varepsilon}$ relationship where ε is the dielectric constant of the host material (ε ≈ 12 for GaAs in this case) while at the same time a similar mathematical relationship for Syed's data requires an additional factor of 2.5, as indicted in the figure. Extending this idea to the unexplained feature seen in sample s716 it was found that rather than a factor

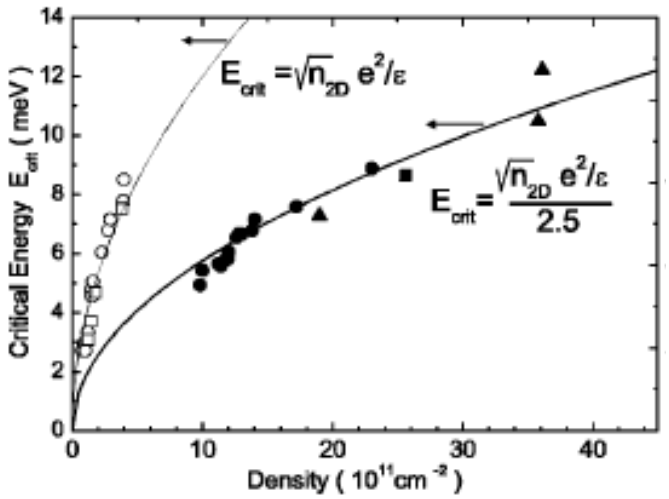

Figure 6.12: Critical energy vs. sample density for an unexplained feature seen by both Schlesinger *et al.* (open squares and circles) [77] and S.Syed *et al.* (filled circles and triangles) [78].

of 2.5, a division by approximately 0.175 is required to fit the unusual feature seen in s716, as shown in Figure 6.13. Although the origin of this phenomenon is yet to be determined, it is interesting to note that the scaling factor needed seems to scale with the effective mass of the material in question.

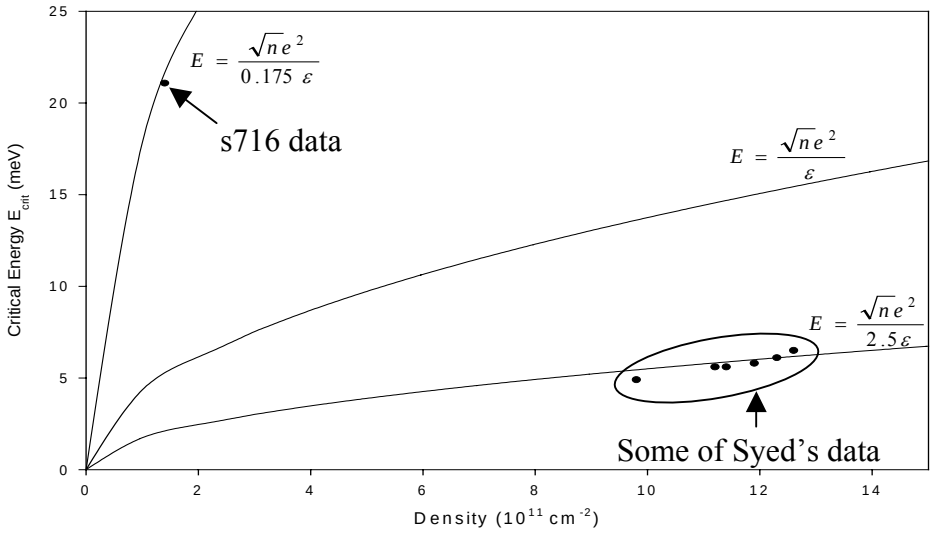

Figure 6.13: Graph showing how s716 data compares to other unexplained features seen previously

However, if the unknown phenomenon discussed by Schlesinger and again by Syed is indeed responsible for the unexplained feature of sample s716, one might wonder if the equation arrived at in Figure 6.13 accurately predicts any unexplained features for any of the other samples of this study, specifically s499, s702, and s842. If the same equation is applied to these samples, the predicted critical energies for these samples are as follows:

s499: E_{crit} = 25.8 meV (208 cm^{-1})

s702: E_{crit} = 27.6 meV (222 cm^{-1})

s842: E_{crit} = 35.6 meV (287 cm^{-1})

Unfortunately, for sample s842, this region is obscured by the phonon window discussed previously. However, this is not the case for s499 and s702. Yet, upon reviewing the data over the regions of interest for these two samples, no unusual features indicating an, as yet unexplained anti-crossing, are found. This fact casts some doubt on whether or not this phenomenon can truly explain the unusual feature seen in sample s716.

There is another possible explanation to explain this unusual feature however. A study done by Heitmann *et al.* [81] on InAs quantum wells found a decrease in intensity of the light transmitted through the sample when at integer filling factors. Referring back to Figure 6.11, one will see that the unusual feature for sample s716 occurs between approximately 3.2 and 3.9 Tesla. Unfortunately, for sample with s716's density (n = 1.4×10^{11} cm^{-2}) the closest integer filling factor

is filling factor 2 which occurs at approximately 2.9 Tesla. Therefore, it seems unlikely that this feature is related to the intensity decrease seen by Heitmann *et al.*

And finally, on sample s716 there are two additional features that merit discussion. The first is the feature seen between approximately 100 cm^{-1} and 140 cm^{-1} (or about 1.9 T – 2.8 T) in Figure 6.11. This feature occurs too low in magnetic field to be associated with crossings 1 – 4. However, unlike the unexplained feature discussed above, this feature does occur in the red transition, so Weick's half field crossings are at least a candidate to explain it. For a sample with s716's growth parameters (300 Å, 9%) the half field crossings occur between 2.5 and 3.5 Tesla, so it is possible that this feature is associated with these half field crossings.

The other feature is seen in a much higher magnetic field regime as seen in Figure 6.14. Clearly, due to the high magnetic field, this feature cannot be associated with crossings 1 – 4. However, referring back to Figure 5.5, there are other crossings that occur at higher fields due to the intersection of the n = 1 Landau Levels of the lowest subband and the n = 0 Landau Levels of the *third* subband (crossings x, y, 5, and 6 in Figure 5.5). And if one looks at the associated Fan diagram for s716 (see Appendix A) it is found that crossing 6 occurs at the appropriate magnetic field range to explain this feature. So it is quite possible that this high field feature is that crossing 6. It should also be noted

that in this Fan Diagram, the inter-subband spacing has NOT been reduced as discussed in Chapter 5 concerning crossing X for sample s842. If one looks at the Fan Diagram for s716 it is quite clear that reducing the inter-subband would move the crossings X, Y, 5 and 6 all down in magnetic field, thus crossings 6 could no longer explain the feature shown in Figure 6.14.

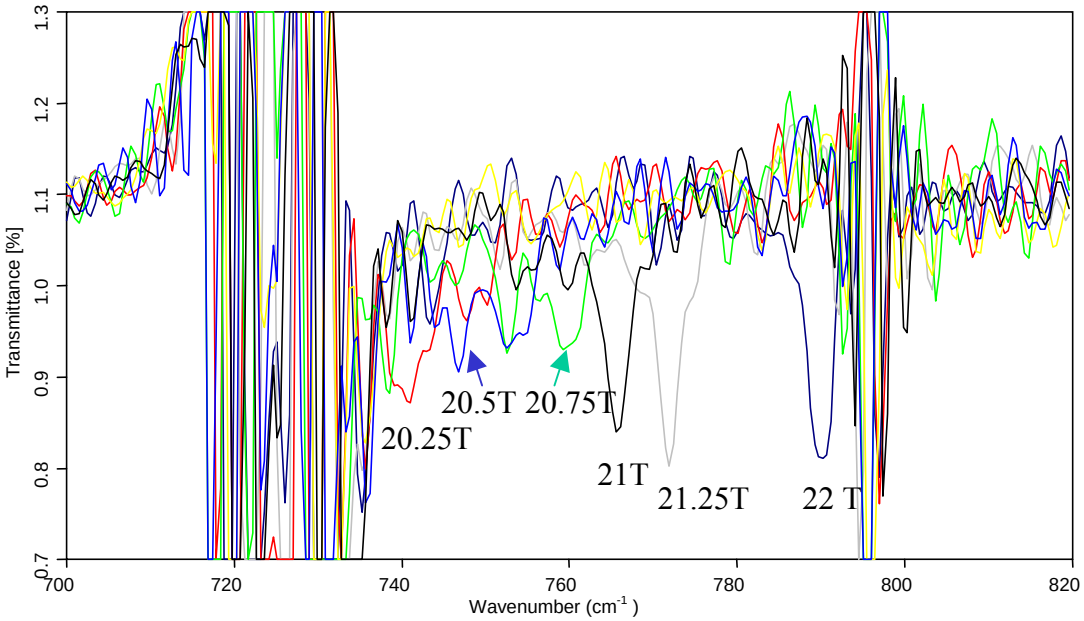

Figure 6.14: Spectra for sample s716 at high magnetic field showing another unusual feature.

6.3 OU FTIR Light Pipe Improvements

In this study, the data used was gathered using the FTIR and magnets at the National High Magnetic Field Laboratory (NHMFL) in Tallahassee, Florida. The reason for this, however, is not entirely due to the high magnetic fields possible at this facility. In addition to the high fields, the FTIR setup at this

laboratory proved to be most reliable in providing good experimental results. Yet, referring back to Figure 2.5, one will see that the far infrared experimental setup at the University of Oklahoma (OU) also possess an FTIR. Unfortunately, however, it was found that the OU FTIR setup using an external light pipe and magnet possessed a signal to noise ratio that simply made the desired experiments impossible. This, however, was not due to any design error in the FTIR itself, as other experiments, such as photo-luminescence, were done using only the FTIR setup alone, and produced usable results. Thus, the problem seemed to lie in the initial light pipe design used in the attempted magneto-optical experiments. Therefore, a redesign of the FTIR light pipe was under taken to produce a lower signal to noise ratio, resulting in a much improved experimental setup and providing a means to continue the study begun in this work. A schematic comparison of the original and the new FTIR light pipes is shown in Figure 6.15.

The improvements to the FTIR light pipe design are numerous, however, probably the most significant is the change in the reflective material used on the interior surface of the light pipe. The original light pipe was constructed entirely from brass, thus the interior surface was polished to produce a reflective surface. The problem, however, is that polished brass only possesses a reflectance coefficient of about 0.80 for infrared light. In other words, when infrared light is incident on polished brass, only about 80% of the incident light is reflected.

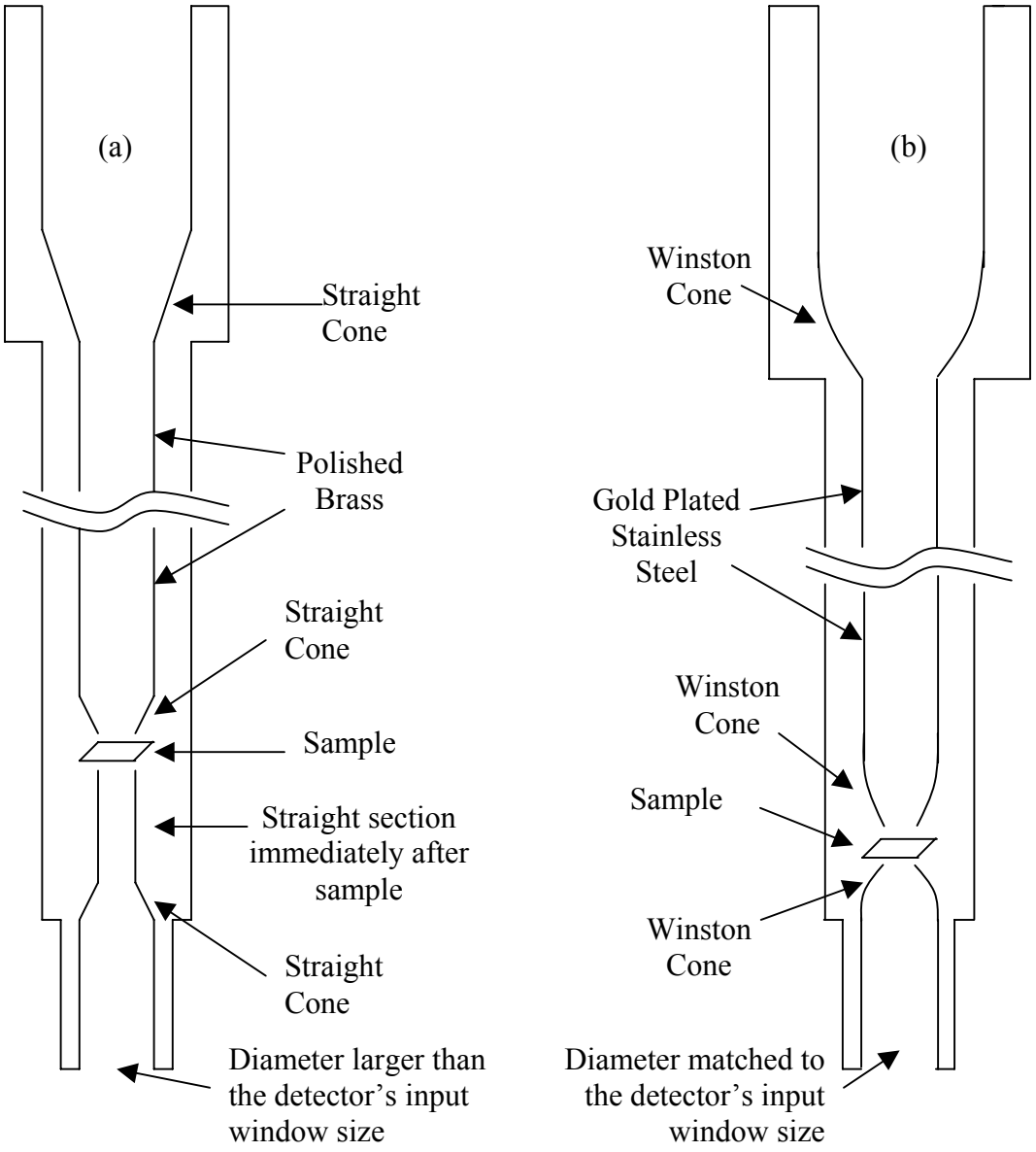

Figure 6.15 Comparison of the (a) original and (b) new light pipes for the FTIR experimental setup at the University of Oklahoma.

Therefore, after the numerous reflections that are inevitable inside any light pipe, the intensity of the infrared light will be greatly reduced. The new light pipe,

however, has been constructed from stainless steel and will have its entire interior surface coated in highly reflective gold. Polished gold possesses a reflectance coefficient of about 0.98 for infrared light. Thus, far less intensity will be lost in the new light pipe, even for a large number of internal reflections.

Another important improvement in the light pipe is in the design of the focusing cones used to concentrate the light on the sample. In the original light pipe, all the focusing cones have flat, angled surfaces, sometimes refereed to as a straight cone. Although this type of cone design is rather simple to design and construct, it is not an ideal design to reduce the number of reflections and focus the light. On the other hand, in the new light pipe all the cones possess a curved, parabolic shape. This type of cone design is known as a Winston Cone [20] and, although somewhat more difficult to design and construct, are far superior to the straight cones in reducing the number of reflections and focusing the light.

Although the inclusion of a gold plated interior and a redesign of the focusing cones using Winston cones are probably the two biggest improvements over the previous light pipe design, two other improvements merit mentioning. First, in the original light pipe, immediately below the sample, there was a straight section of pipe before the final cone (refer to Figure 6.15(a)). The reason for this straight section is a result of how the sample was mounted in the original light pipe. Although at first glance this straight section may not appear to be much of a concern, notice how directly above the sample is a focusing cone. Because of

this, the light passing through the sample will have a significant horizontal component to its direction. Therefore, when the light enters the straight section immediately below the sample, it will experience a large number of additional reflections before encountering the final cone. Referring back to the previous discussion on the reflectance coefficient for polished brass, these additional reflections each reduce the signal strength and are therefore quite undesirable. To overcome this, the technique for mounting the sample has been redesigned in the new light pipe so that the final cone sits immediately below the sample, thus eliminating this straight section and these additional, undesirable reflections.

The final change in the light pipe design worth mentioning is the final interior diameter of the light pipe. This is the section of the light pipe that sits immediately above the bolometer detector, which is mounted on the bottom of the vacuum can assembly in which the light pipe sits. In the original light pipe, this lower interior diameter is larger than the diameter of the bolometer's input window. This results in some of the light being reflected back up the light pipe from the exposed areas of the bolometer's casing immediately outside the diameter of the window. This, again, reduces the strength of the desired infrared signal. Therefore, in the design of the new light pipe, this lower interior diameter was intentionally matched to the diameter of the bolometer's input window in order to maximize the strength of the infrared signal.

All the improvements to the new light pipe mentioned above should greatly increase the signal to noise ratio of the external magneto-optical FTIR setup at OU so further experiments extending this work can be conducted on site.

6.4 Final Conclusions

The purpose of this work was to experimentally explore the both the band structure and spin properties of InSb quantum wells. In almost all samples studied, spin resolved cyclotron resonance was clearly seen and the positions of these resonances were in good agreement with our theoretical model. Also, the intensities of these transitions were studied and were seen to have rough agreement with our model, at least in a lower magnetic field regime. However, at higher magnetic fields (i.e. lower filling factor), these intensities maintained rather constant values not predicted by theory. Also, it was seen that the intensity of the blue transition displayed unusual behavior between filling factors 2 and 3. In addition to spin split cyclotron resonance, this study also looked at anti-crossings that occurred between the Landau Levels of different subbands in the samples. Both same spin and, somewhat surprisingly, opposite spin anti-crossings were observed. For the same spin anti-crossings, it was observed that the size of the energy gap, ΔE, increases with tilt angle θ. However, unlike the theoretical predictions, the experimentally determined slope of ΔE vs. θ depends

on the spin states involved in the avoided-level crossing. Further, again deviating from theory, ΔE did not equal zero for zero tilt for crossing 2, but did seem to for crossing 3. Thus, it was concluded that the standard coupling mechanism does not accurately describe these crossings.

For the opposite spin anti-crossings it was observed that the size of the energy gap, ΔE, is essentially independent of the tilt angle up to 11^0. Also, it was seen that this energy gap is essentially independent of the structural asymmetry of the sample. Various possible explanations were looked at in an effort to explain these observed opposite spin anti-crossings such as the Rashba and Dresselhaus terms, as well as band non-parabolicity. However, it was determined that none of them were able to sufficiently explain the observed anti-crossings.

Finally, the observed positions of the both the same spin and opposite spin crossings were compared to the theoretical crossing positions. It was found that in order to produce agreement between the two, the samples theoretical growth parameters, such as well width and barrier concentration, had to be adjusted. This, coupled with x-ray diffraction measurements, leads to the conclusion that these growth parameters are not necessarily those intended.

In conclusion, there remain a number of unresolved issues in this study. In summary, these issues are:

1) Odd behavior in blue transition intensity between filling factors 2 and 3 (Chapter 3).

2) Constancy in both blue and black transition intensities at higher B-fields (lower filling factor) (Chapter 3).

3) Inconsistent density in classical model used to fit CR line shapes (Chapter 3).

4) Inability of our model to fit all observed anti-crossings with a consistent well width and Al. concentration (Chapter 6 and Appendix B).

5) Discrepancy of our model with ESR data (Chapter 6).

6) Inability of our model to explain the two unusual features seen in s716 data (high field feature could be crossing 6) (Chapter 6).

Clearly, the model used in this study needs improvement. One possibility is the inclusion of more bands. This would bring our results more in line with the ESR data gathered previously. However, as was seen earlier in this chapter, this will only result in an increase in g-factor of 8%, rather than the needed 15 –23 %. Recall that in order to fit our model to the experimental ESR data, the g-factor needed to be increased 15 % for the 300Å samples and 23 % for the 200 Å samples. This, at least, implies a thickness dependence for the necessary g-factor increase (i.e. band structure). It should also be noted that our current "2D" model is actually a 3D model with the correction of an effective band gap (see Chapter 1). A more accurate 2D model would be desirable, however, none is currently available.

Bibliography

[1] E. O. Kane J.Phys. Chem. Solids, **1**, 249 (1957).

[2] G. Bastard, Wave Mechanics Applied to Semiconductor Heterostructures Les Editions Physique, Les Ulis (1988).

[3] O. Madelung, Physics of III-V Compounds. John Wiley & Sons, Inc. (1964).

[4] S. L. Chuang, Physics of Optoelectronic Devices. John Wiley & Sons, Inc. (1995).

[5] N. Dai, G. A. Khodaparast, F. Brown, R. E. Doezema, S. J. Chung, and M. B. Santos, Appl. Phys. Lett. **76**, 3905 (2000).

[6] G. A. Khodaparast, PhD. Dissertation, The University of Oklahoma, 2001.

[7] U. Rösller, Solid State Commun. **65**, 1279 (1988).

[8] G. Bastard, J. A. Brum, and R. Ferreira, Solid State Physics, Volume 44, 229 (1991).

[9] J. Luttinger and W. Kohn, Phys. Rev. **97**, 869 (1955).

[10] I. M. Tsidilkovski, Band Structure of Semiconductors, International Series in the Science of the Solid State, Volume 19, Pergamon Press.

[11] Landolt-Bornstein, in Numerical Data and Functional Relationships in Science and Technology, edited by O. Madelung (Springer, Berlin, 1987), Group III, Vol. 22.

[12] J. P. Eisenstein & H. L. Stormer, Science **248**, 1510 (1990).

[13] B. I. Halperin, Scientific American, April, 52-60 (1986).

[14] Kory J. Goldammer, Ph.D. Dissertation, The University of Oklahoma, (1998).

[15] K. J. Goldammer, W. K. Liu, G. A. Khodaparast, S. C. Lindstrom, M. B. Johnson, R. E. Doezema, and M. B. Santos, J. Vac. Sci. Technol. B16, 1367 (1998).

[16] D. K. Schroder, editor, *Semiconductor Material and Device Characterization,* Wiley, 1976.

[17] L. J. van der Pauw, Philips Res. Rep. **13**, 1 (1958).

[18] D. K. de Vries and A. D. Wieck, Am. J. Phys. **63**, 12 (1995).

[19] J. F. James, *A Students Guide To Fourier Transforms*, Cambridge University Press, 1995.

[20] D. A. Harper, R. H. Hildebrand, R. Stiening, and R. Winston, Applied Optics **15**, 53 (1976).

[21] J. Scriba, A. Wixforth, J. P. Kotthaus, C. R. Bolognesi, C. Nguyen, G. Tuttle, J. H. English, H. Kroemer, Semicond. Sci. Technol. 8 S133 (1993).

[22] M. J. Yang, R. J. Wagner, B. V. Shanabrook, J. R. Waterman, W. J. Moore, Phys. Rev. B. 47 6807 (1992).

[23] C. R. Pidgeon, R. N. Brown, Phys. Rev. 146 575 (1966).

[24] M. J. Yang, R. J. Wagner, P. J. Lin-Chung, B. V. Shanabrook, J. R. Waterman, W. J. Moore, and J. L. Davis, Surf. Sci. 305, 271 (1994).

[25] C. R. Pidgeon and R. N. Brown, Phys. Rev. **146**, 575 (1966).

[26] C.R. Pigeon, "Landau Level Spectroscopy," ed. G. Landwehr and E. I. Rashba, Modern Problems in Condensed Matter Sciences, Vol. 27.1 (North-Holland, Amsterdam, 1991) pp.447-479.

[27] M. Horst, U. Merkt, and J. P. Kotthaus, Phys. Rev. Lett. **50**, 754 (1983).

[28] F. M. Peeters, J. M. Shi, J. T. Devreese, J. P. Cheng, B. McCombe and W. Schaff, Solid-State Electronics, Volume 37, Issues 4-6, April-June 1994, Pages 1217-1220.

[29] D. F. Howell, T. J. B. M. Janssen, R. J. Nicholas, C. J. G. M. Langerak, J. Singleton and A. Chevy, Surface Science, Volume 229, Issues 1-3, 2 April 1990, Pages 496-500.

[30] R. Lassnig and W. Zawadzki, Surface Science, Volume 142, Issues 1-3, 1 July 1984, Pages 388-393

[31] G. M. Summers, R. J. Warburton, J. G. Michels, R. J. Nicholas, J. J. Harris, and C. T. Foxon, Phys. Rev. Lett. **70**, 2150 (1993).

[32] C. M. Hu, T. Friedrich, E. Batke, K. Köhler, and P. Ganser, Phys. Rev. B **52**, 12090 (1995).

[33] S. J. Chung, K. J. Goldammer, S. C. Lindstrom, M. B. Johnson, and M. B. Santos, J. Vac. Sci. Technol. B17, 1151 (1999).

[34] F. A. Johnson, Proc. Phys. Soc. (London) **73**, 265 (1959).

[35] L. Patrick and W. J. Choyke, Phys. Rev. **123**, 813 (1961).

[36] D. A. Kleinman and W. G. Spitzer, Phys. Rev. **118**, 110 (1960).

[37] R. J. Cherry, Phys. Rev. Letters **4**, 234 (1963).

[38] S. J. Fray, F. A. Johnson, and R. H. Jones, Proc. Phys. Soc. (London) **76**, 939 (1960).

[39] W. Cochran, S. J. Fray, F. A. Johnson, J. E. Quarrington, and N. Williams, J. Appl. Phys. **32**. 2102 (1961).

[40] W. J. Turner and W. E. Reese, Phys. Rev. **127**, 126 (1962).

[41] S. S. Mitra, Phys. Rev. **132**, 986 (1963).

[42] V. P. Gnezdilov, D. J. Lockwood, J. B. Webb, Phys. Rev. B, **48**, 11228 (1993).

[43] G. A. Khodaparast, R. C. Meyer, X. H. Zhang, T. Kasturiarachchi, R. E. Doezema, S. J. Chung, N. Goel, M. B. Santos, and Y. J. Wang, Physica E **20**, 386 (2004).

[44] X.G. Wu, F.M. Peeters, Y.J. Wang, and B.D. McCombe, Phys. Rev. Lett. 84, 4934 (2000)

[45] M. J. Chou and D. C. Tsui, Mat. Res. Soc. Symp. Proc., **37**, 7 (1985).

[46] M. J. Chou, D. C. Tsui, and G. Weimann, Phys. Rev. B, **37**, 848 (1988).

[47] T. Ando, Phys. Rev. B, **19**, 2106 (1979).

[48] Frank Stern, Phys. Rev. B, **5**, 4891 (1972).

[49] R. Merlin, Soild State Commun. **64**, 99 (1987).

[50] T. Ando, Journal of the Phy. Soc. of Japan, **38**, 989 (1975).

[51] W. Kohn, Phys. Rev., **123**, 1242 (1961).

[52] R. Borroff, R. Merlin, J. Pamulapati, P. K. Bhattacharya, and C. Tejedor, Phys. Rev. B **43**, 2081 (1991).

[53] B. Huckestein and R. Kümmel, Z. Phys. B **66**, 475 (1987).

[54] M. Załuzny, Phys. Rev. B **40**, 8495 (1989).

[55] W. Beinvogl and J. F. Koch, Phys. Rev. Lett. **40**, 1736 (1978).

[56] G. L. J. A. Rikken, H. Sigg, C. J. G. M. Langerak, H. W. Myron, J. A. A. J. Perenboom, and G. Weimann, Phys. Rev. B **34**, 5590 (1986).

[57] S. Huant, M. Grynberg, G. Martinez, and B. Etienne, Solid State Commun. **65**, 457 (1988).

[58] K. Ensslin, D. Heitmann, and K. Ploog, Phys. Rev. B **39**, 10 879 (1989).

[59] S. Huant, G. Martinez, and B. Etienne, Superlatt. Microstruct. **6**, 103 (1989).

[60] M. Shayegan, T. Sajoto, J. Jo, M. Santos, and H. D. Drew, Phys. Rev. B **40**, 3476 (1989).

[61] K. Karrai, H. D. Drew, M. W. Lee, and M. Shayegan, Phys. Rev. B **39**, 1426 (1989).

[62] Z. Schlesinger, J. C. M. Hwang, and S. J. Allen, Jr., Phys. Rev. Lett. **50**, 2098 (1983).

[63] M. A. Brummell, M. A. Hopkins, R. J. Nicholas, J. C. Portal, K. Y. Cheng, A. Y. Cho, J. Phys. C 19 L107 (1986).

[64] A. D. Weick, F. Thiele, U. Merkt, K. Ploog, G. Weimann, and W. Schlapp, Phys. Rev. B **39**, 3785 (1989).

[65] J. Pillath, E. Batke, G. Weimann, and W. Schlapp. Phys. Rev. B **40**, 5879 (1989).

[66] T. Ando, A.B. Fowler, and F. Stern, Rev. Mod. Phys. **54**, 437 (1982).

[67] Y. A. Bychkov and E. I. Rashba, J. Phys. C **17**, 6039 (1984).

[68] Y. A. Bychkov and E. E. Rashba, Pis'ma Zh. Eksp. Teor. Fiz. **39**, 66 (1984).

[69] G. Dresselhaus, Phys. Rev. **100**, 580 (1955).

[70] B. Das, S. Datta, and R. Reifenberger, Phys. Rev. B **41**, 8278 (1990).

[71] N. R. Ogg, Proc. Phys. Soc. **89**, 431 (1966).

[72] Y. F. Chen, M. Dobrowolska, and J. K. Furdyna, Phys. Rev. B **31**, 7989 (1985).

[73] W. Zawadzki, *Landau Level Spectroscopy*, Modern Problems in Condensed Matter Sciences, Vol. 27.1, (North-holland, Amsterdam, 1991) pp. 485-479.

[74] B. D. McCombe and R. J. Wagner, *Intraband Magneto-Optical Studies of Semiconductors in the Far-Infrared, Advances in Electronics and Electron Physics,* Vol. 37, (Academic, New York, 1975), pp.1-78.

[75] R. J. Nicholas, C. C. Chang, and V. Zhitomirskiy, *Optical Properties of Semiconductor Nanostructures,* pp. 33-44.

[76] G. A. Khodaparast, R. E. Doezema, S. J. Chung, K. J. Goldammer, M. B. Santos, Phys. Rev. B **70**, 155322 (2004).

[77] Z. Schlesinger, S. J. Allen, J. C. M. Hwang, P. M. Platzman, N. Tzoar, Phys. Rev. B **30**, 435 (1984).

[78] S. Syed, M. J. Manfra, Y. J. Wang, H. L. Stormer, R. J. Molnar, Phys. Rev. B **67**, 241304 (2003).

[79] E. J. Johnson and D. H. Dickey, Phys. Rev. B **1**, 2676 (1970).

[80] A. D. Weick, J. C. Maan, U. Merkt, J. P. Kotthaus, K. Ploog, G. Weimann, Phys. Rev. B **35**, 4145 (1987).

[81] D. Heitmann, M. Ziesmann, and L. L. Chang, Phys. Rev. B **34**, 7463 (1986).

Appendix A - Experimental Data and Misc.

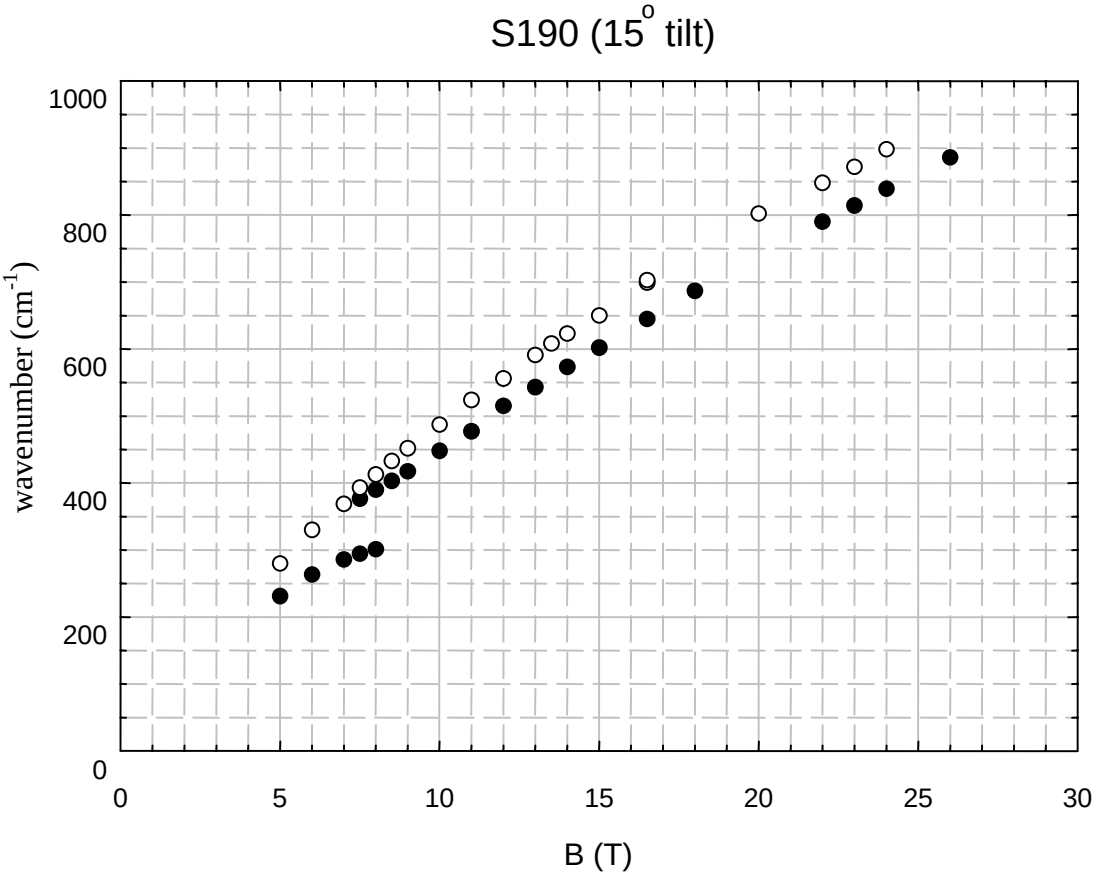

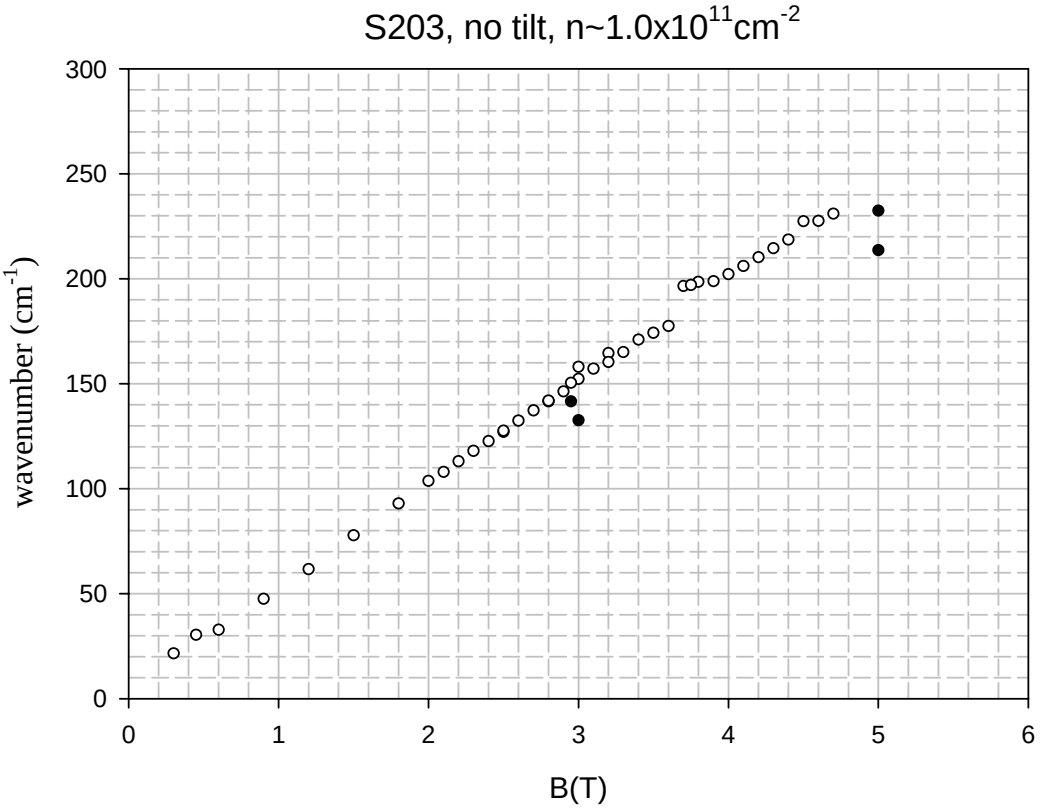
S203, no tilt, n~1.0x10^11cm^-2
wavenumber (cm^-1)
B(T)
0
50
100
150
200
250
300
0
1
2
3
4
5
6

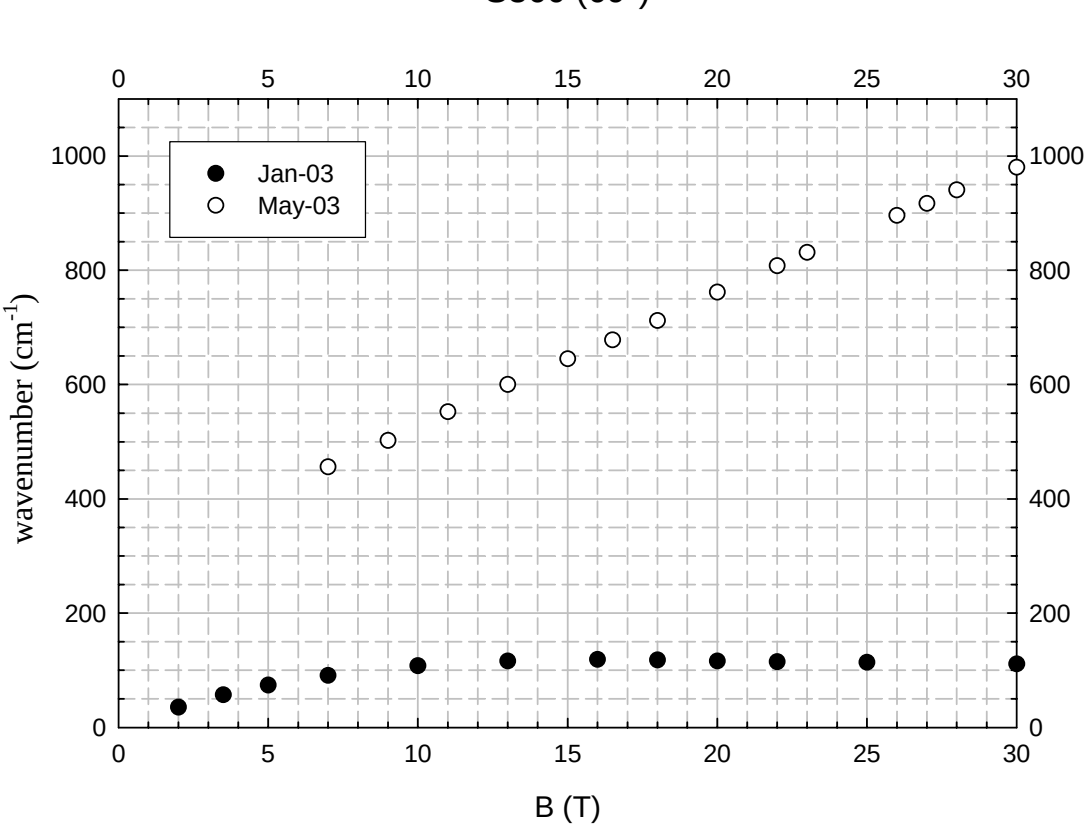
S360 (69°)
Jan-03
May-03
wavenumber (cm^-1)
B (T)
0
200
400
600
800
1000
0
5
10
15
20
25
30

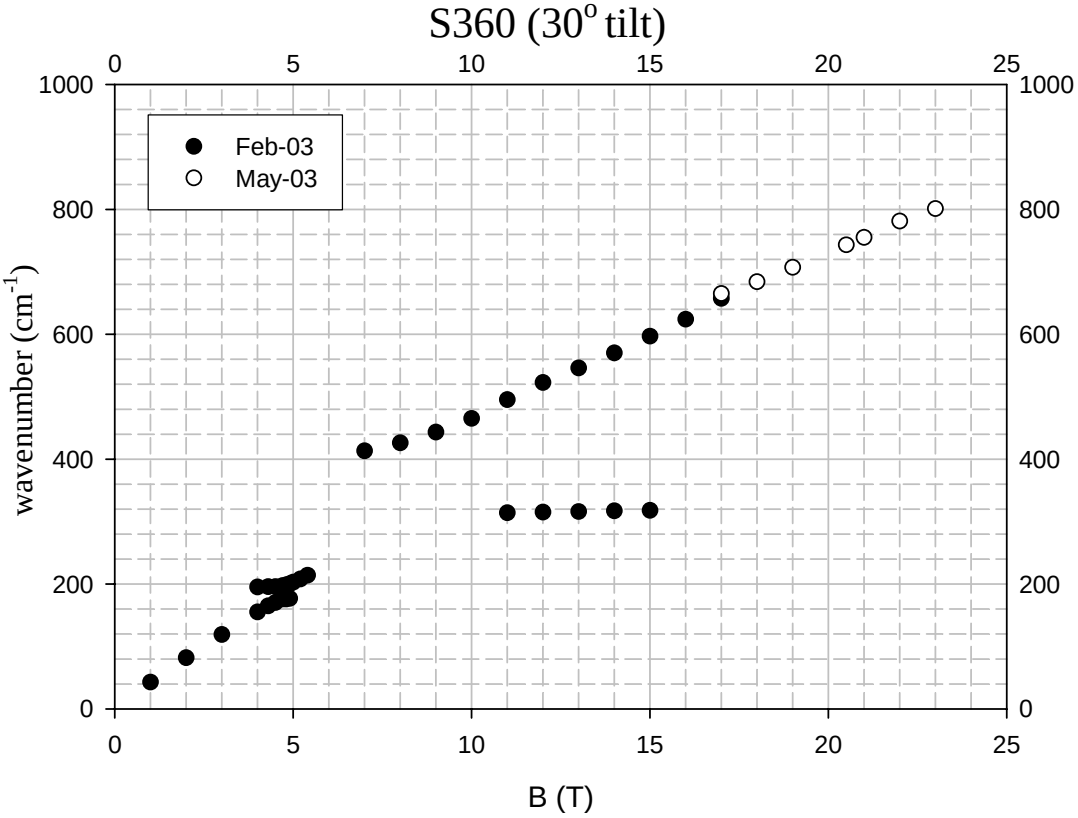
S360 (30° tilt)
Feb-03
May-03
wavenumber (cm-1)
B (T)

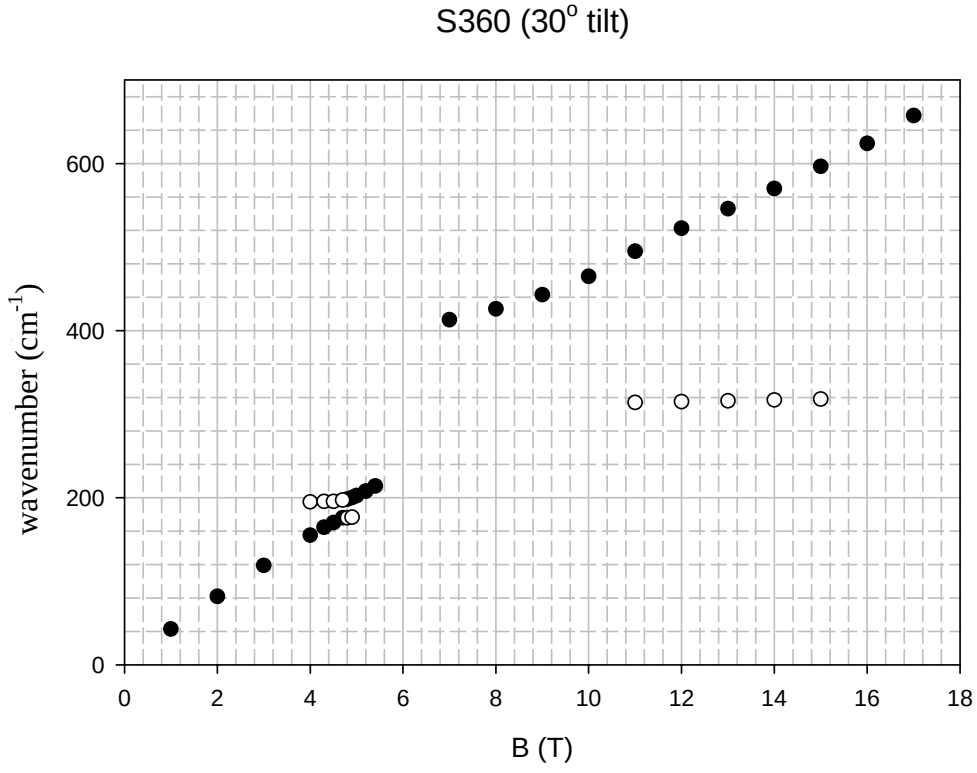
S360 (30° tilt)
wavenumber (cm-1)
B (T)

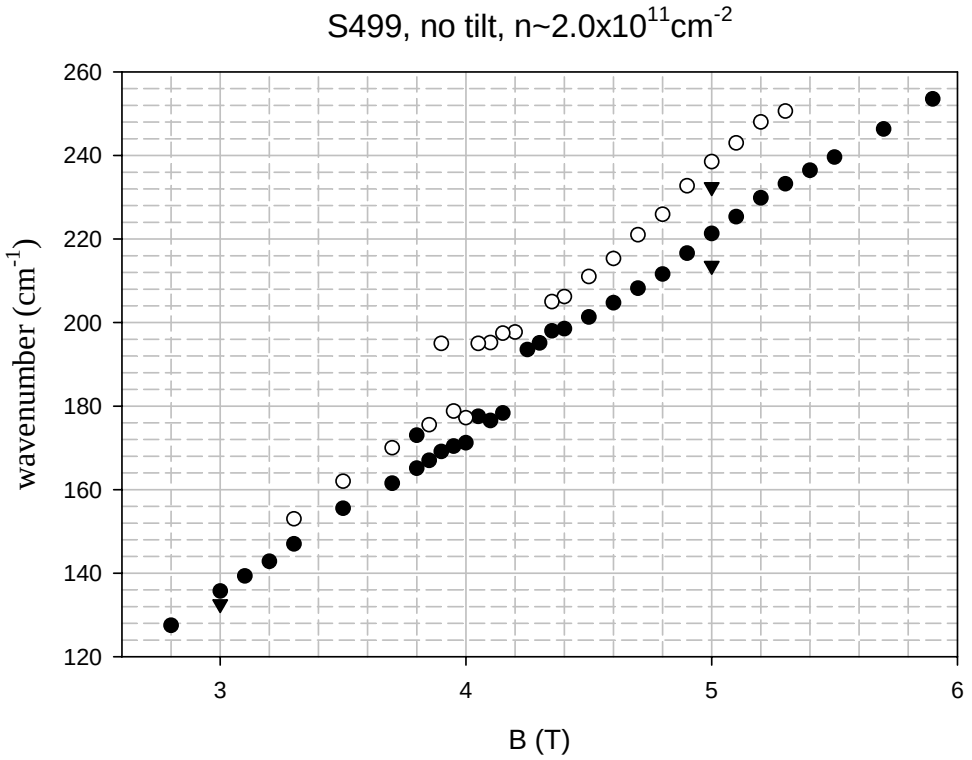
S499, no tilt, n~2.0x10^11cm^-2
wavenumber (cm^-1)
B (T)
260
240
220
200
180
160
140
120
3
4
5
6

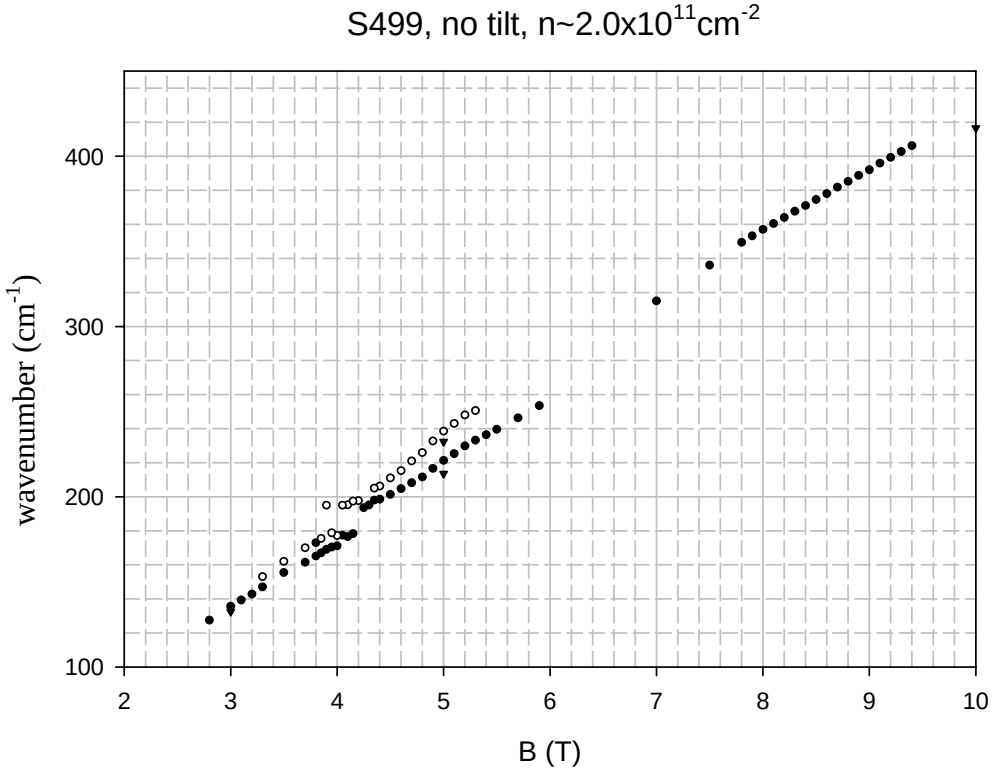
S499, no tilt, n~2.0x10^11cm^-2
wavenumber (cm^-1)
B (T)
400
300
200
100
2
3
4
5
6
7
8
9
10

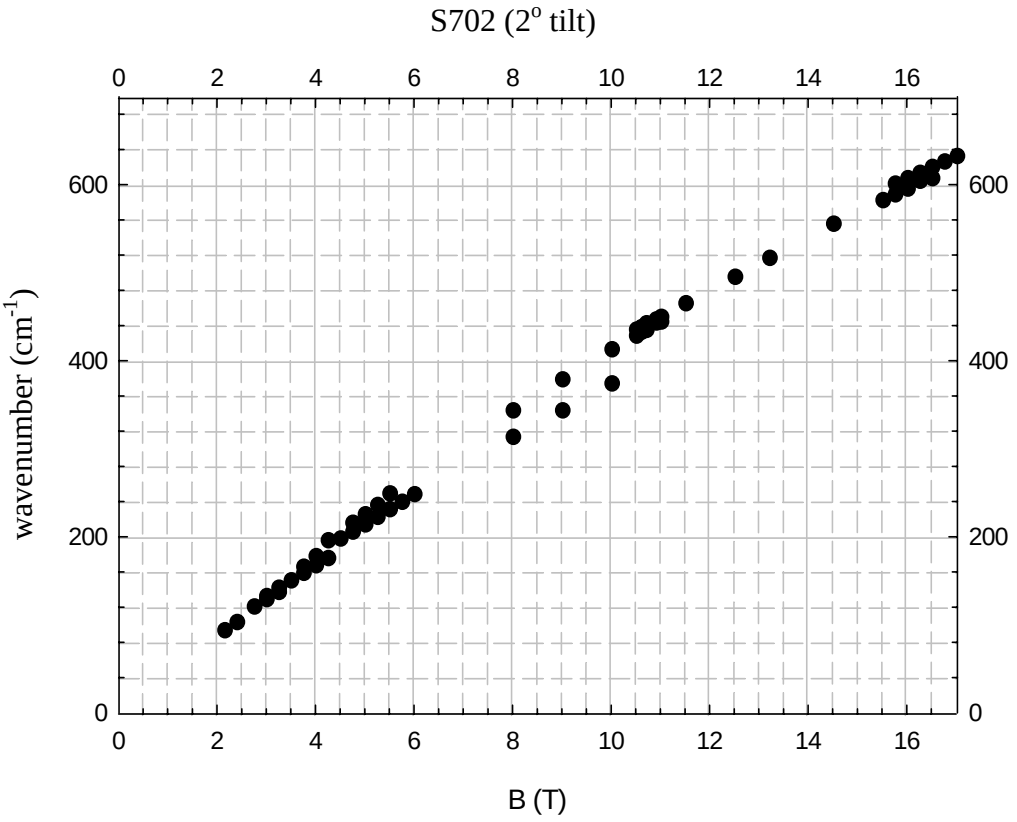
S702 (2° tilt)
wavenumber (cm-1)
B (T)
0
2
4
6
8
10
12
14
16
200
400
600

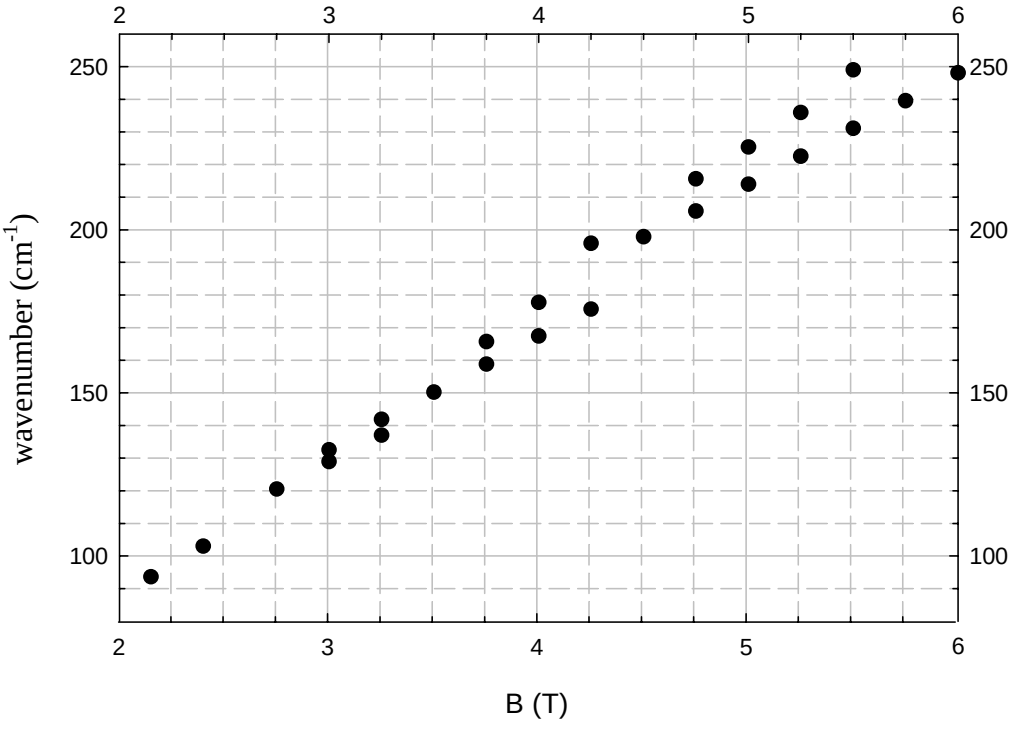
wavenumber (cm-1)
B (T)
2
3
4
5
6
100
150
200
250

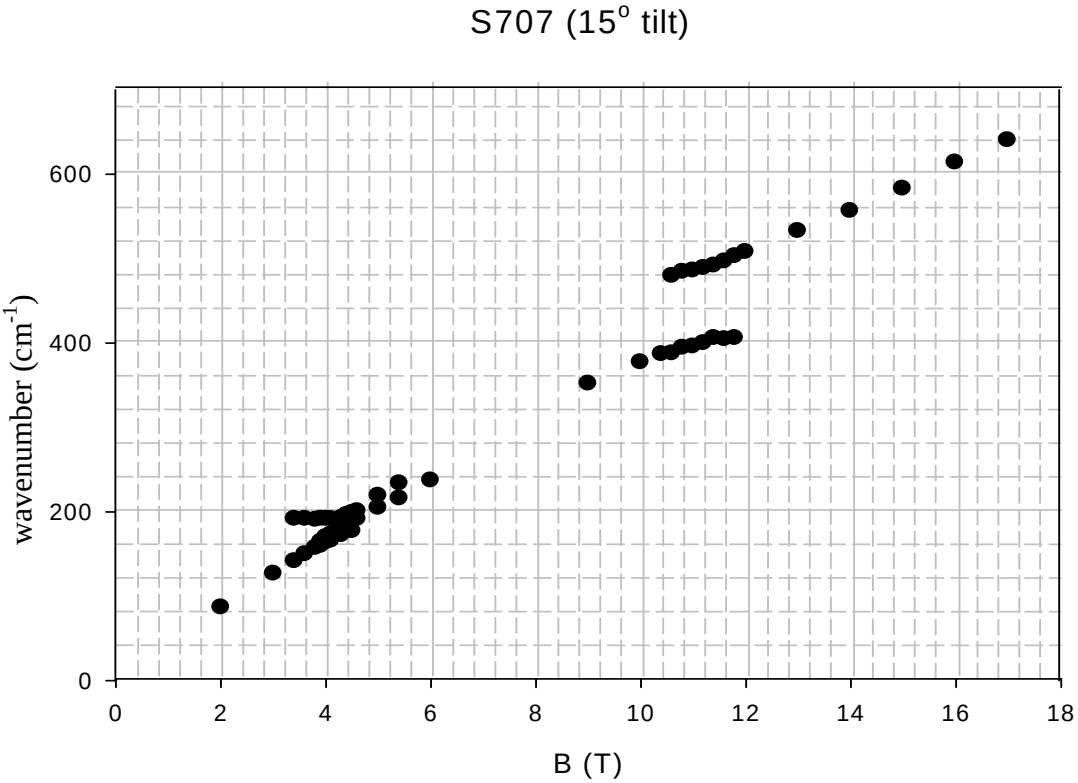
S707 (15° tilt)
wavenumber (cm-1)
0
200
400
600
0
2
4
6
8
10
12
14
16
18
B (T)

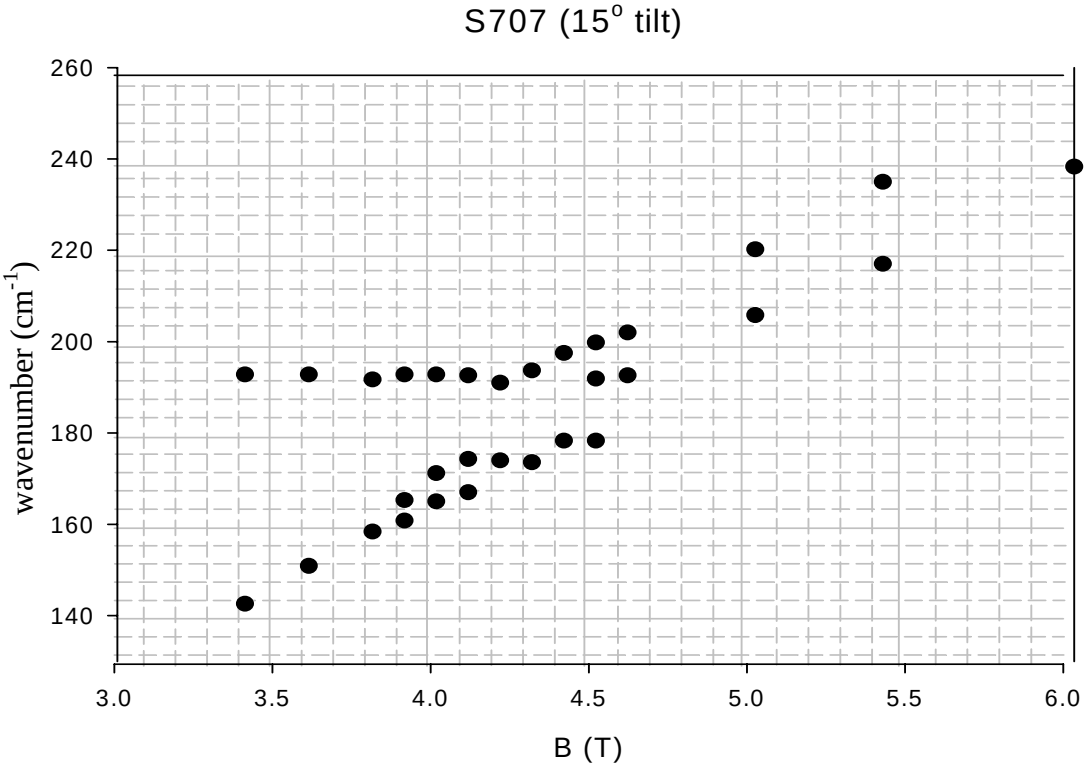
S707 (15° tilt)
wavenumber (cm-1)
140
160
180
200
220
240
260
3.0
3.5
4.0
4.5
5.0
5.5
6.0
B (T)

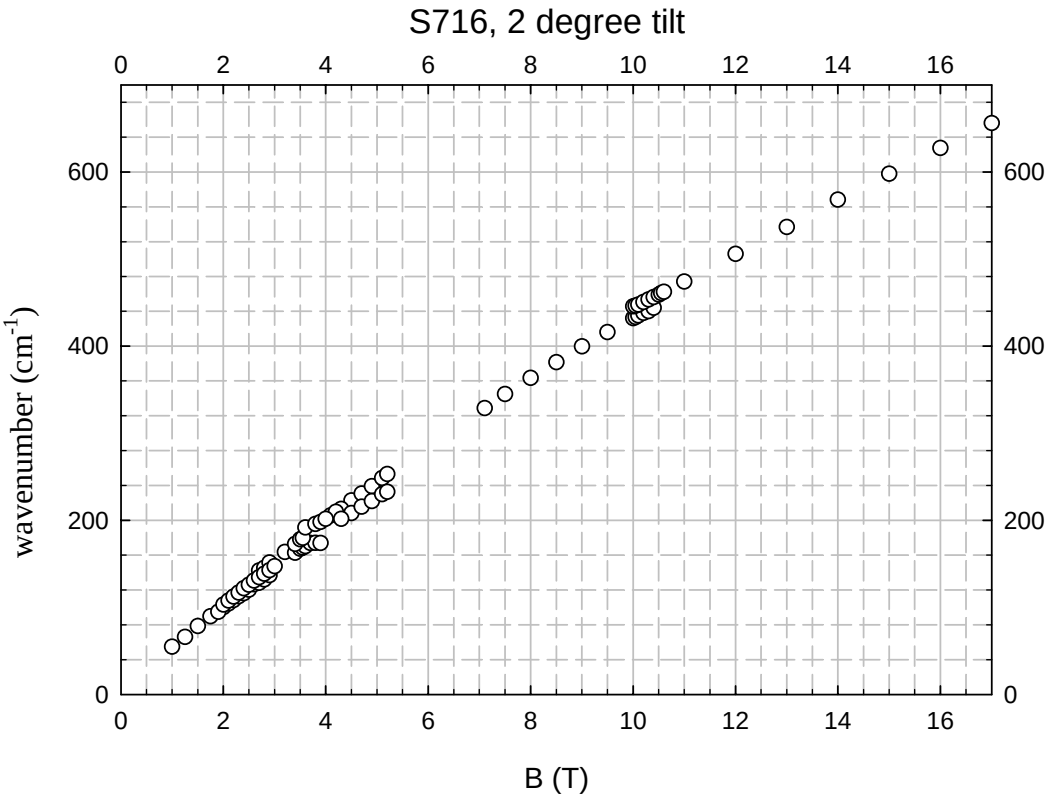
S716, 2 degree tilt
wavenumber (cm-1)
B (T)
0
2
4
6
8
10
12
14
16
0
200
400
600

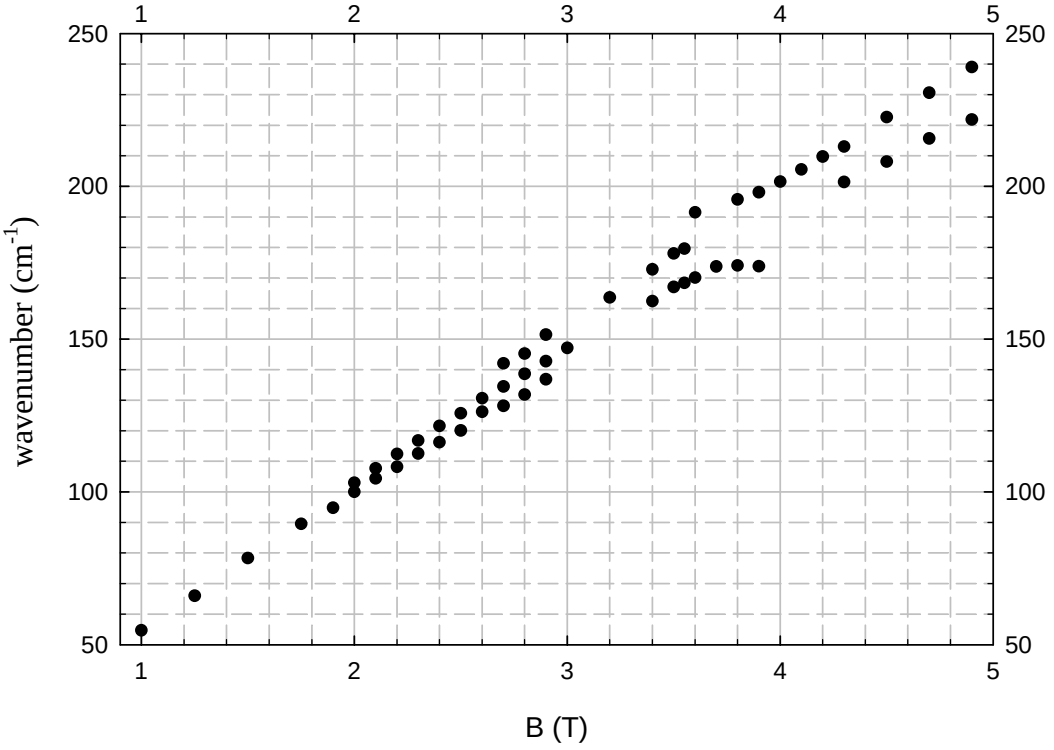
wavenumber (cm-1)
B (T)
1
2
3
4
5
50
100
150
200
250

S842, 4° tilt

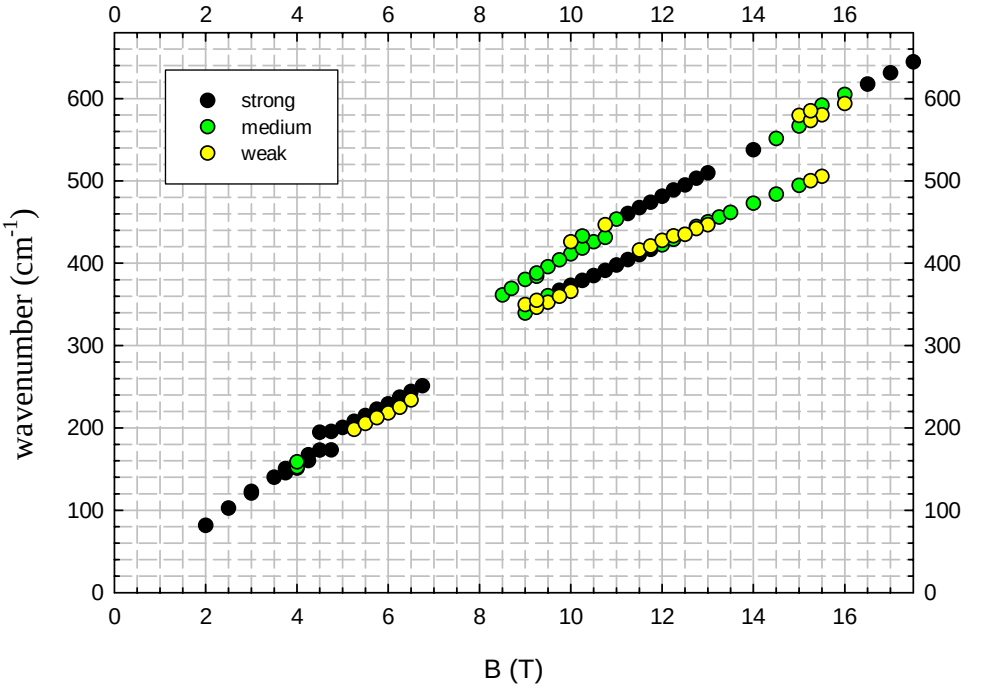
strong
medium
weak
wavenumber (cm-1)
B (T)

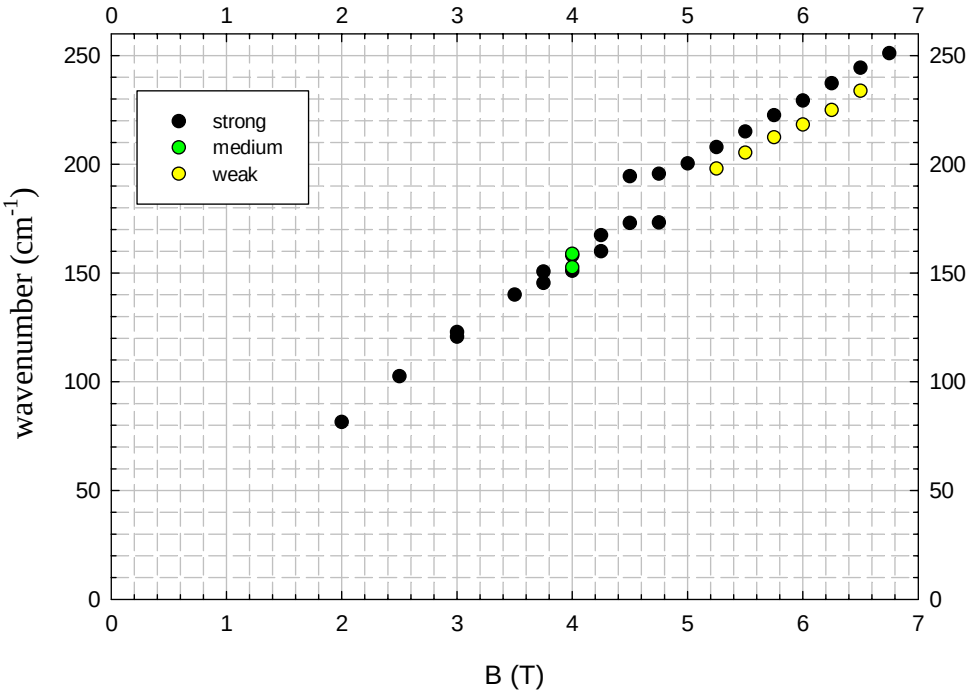
strong
medium
weak
wavenumber (cm-1)
B (T)

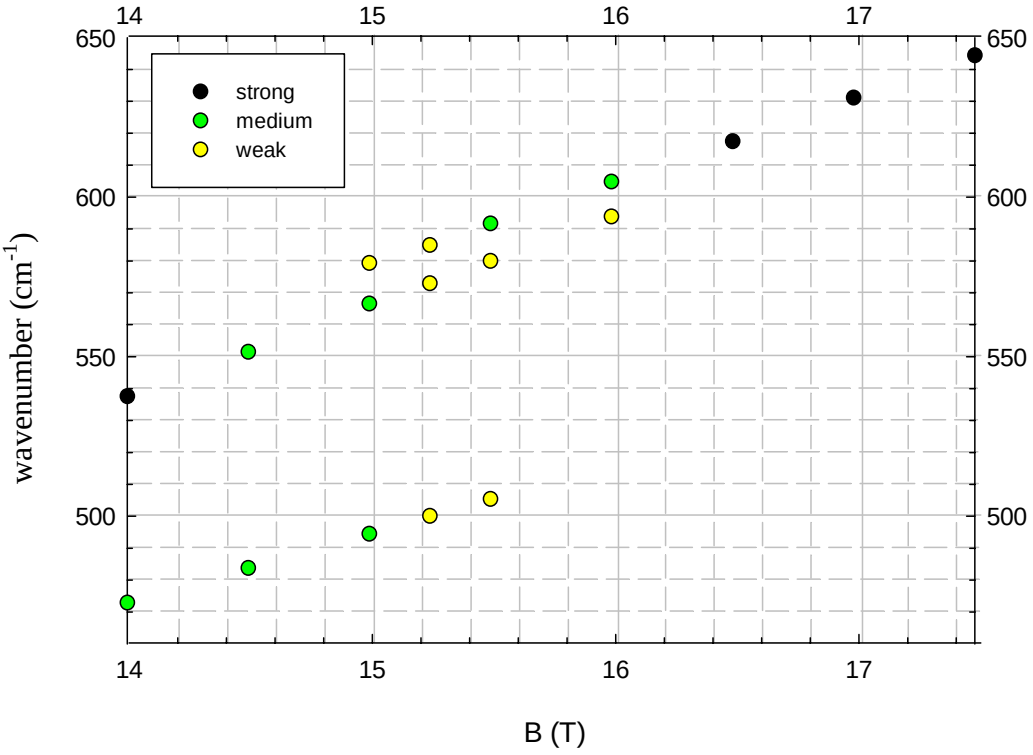
strong
medium
weak
wavenumber (cm-1)
B (T)
14
15
16
17
650
600
550
500

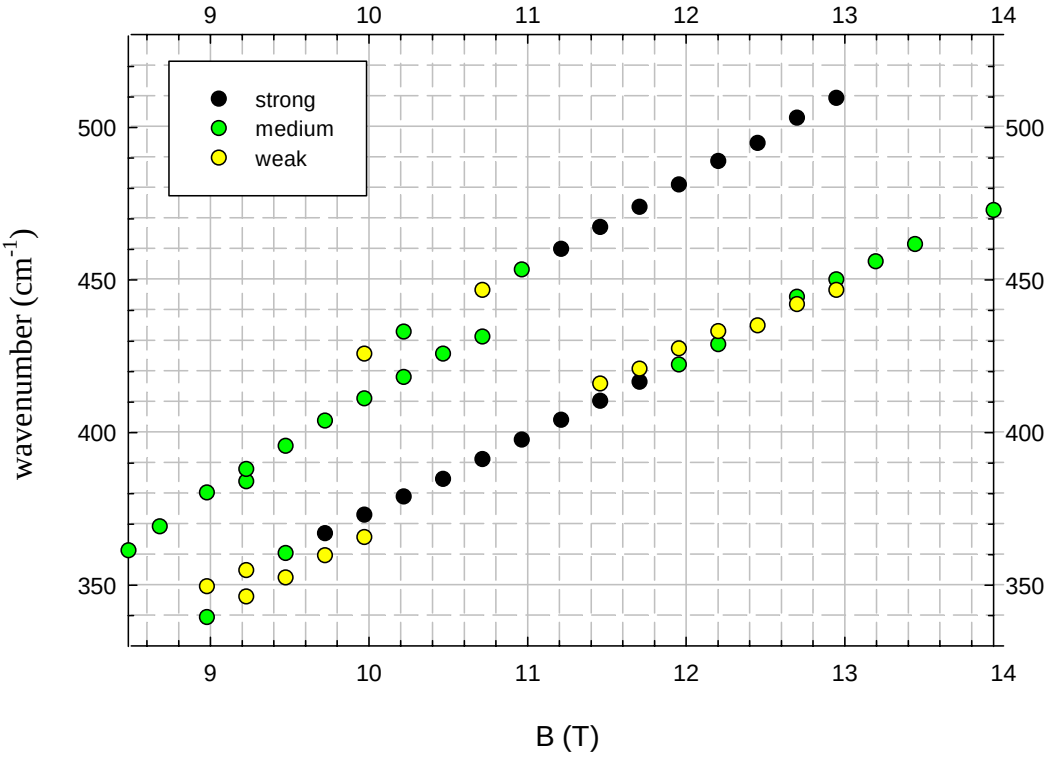
strong
medium
weak
wavenumber (cm-1)
B (T)
9
10
11
12
13
14
500
450
400
350

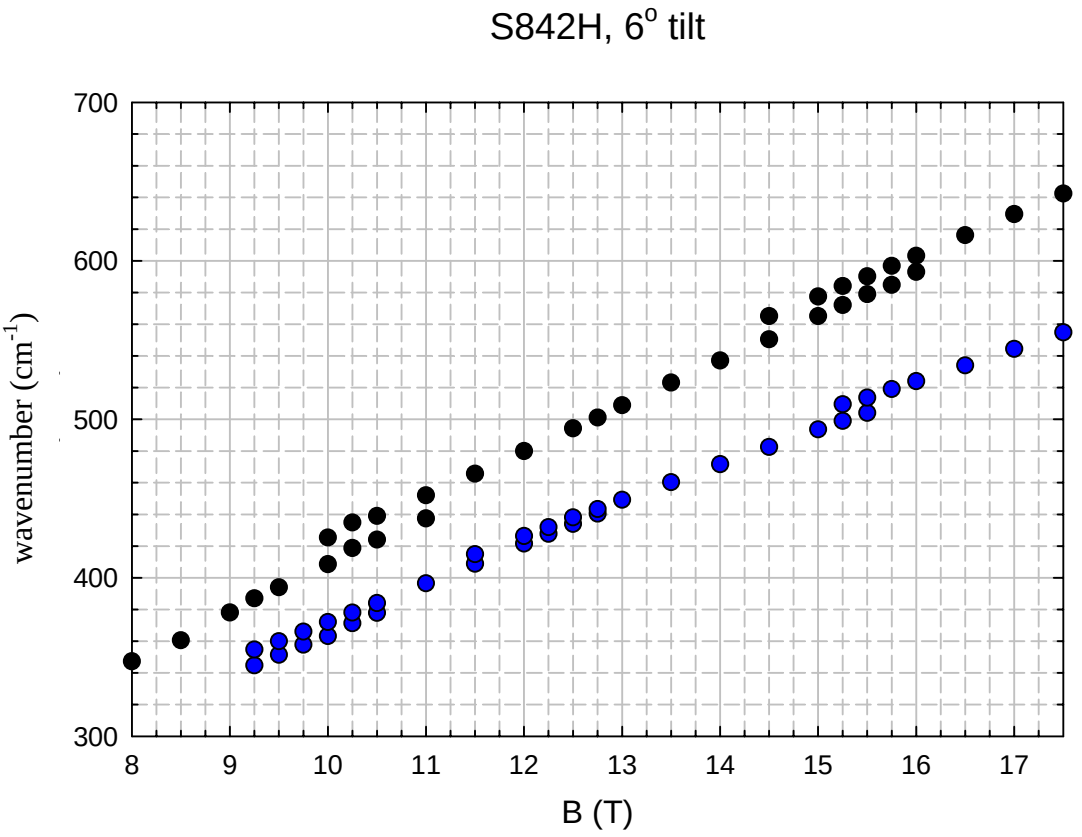
S842H, 6° tilt
wavenumber (cm-1)
B (T)
700
600
500
400
300
8
9
10
11
12
13
14
15
16
17

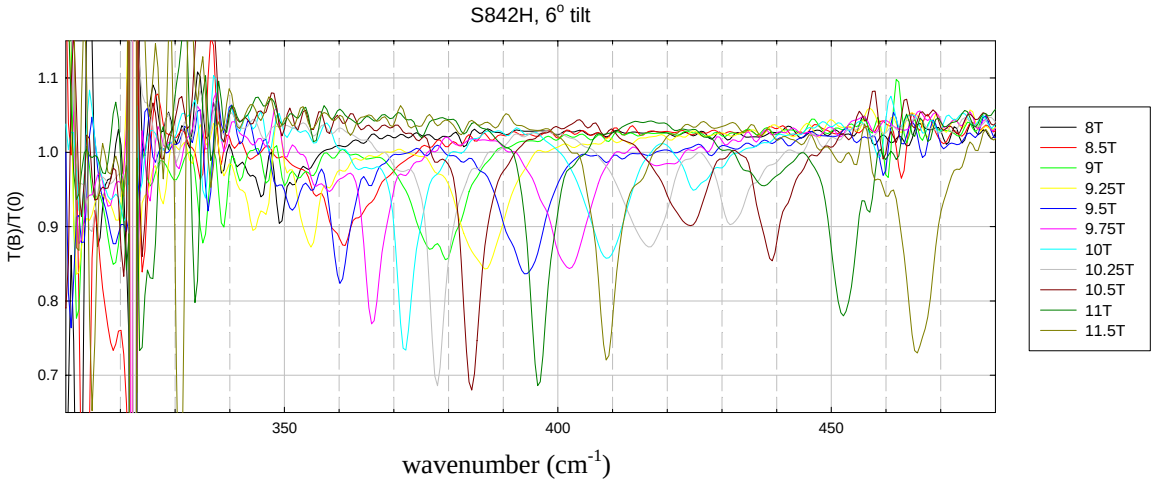
S842H, 6° tilt
T(B)/T(0)
1.1
1.0
0.9
0.8
0.7
350
400
450
wavenumber (cm-1)
8T
8.5T
9T
9.25T
9.5T
9.75T
10T
10.25T
10.5T
11T
11.5T

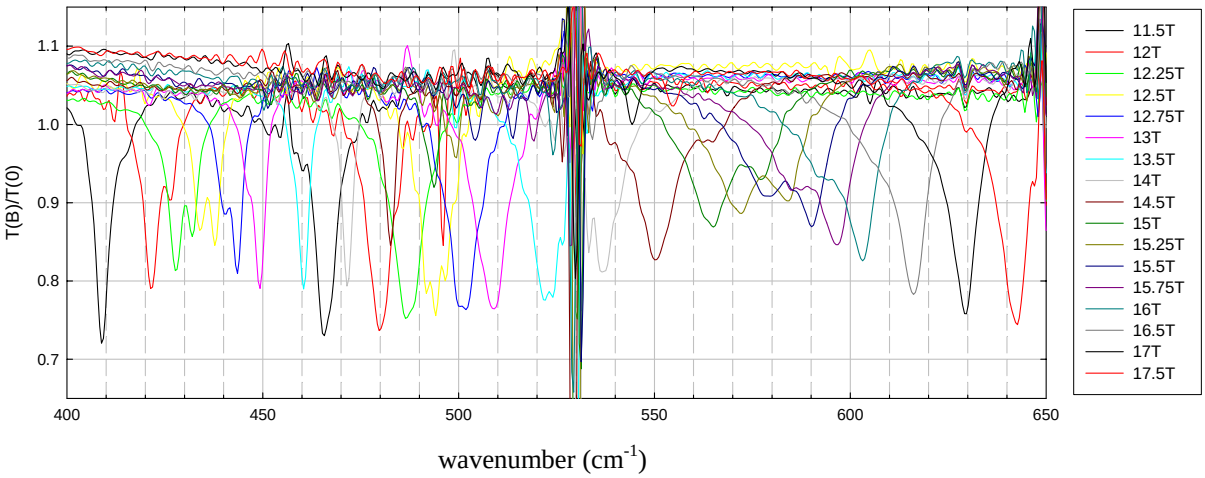
T(B)/T(0)
1.1
1.0
0.9
0.8
0.7
400
450
500
550
600
650
wavenumber (cm-1)
11.5T
12T
12.25T
12.5T
12.75T
13T
13.5T
14T
14.5T
15T
15.25T
15.5T
15.75T
16T
16.5T
17T
17.5T

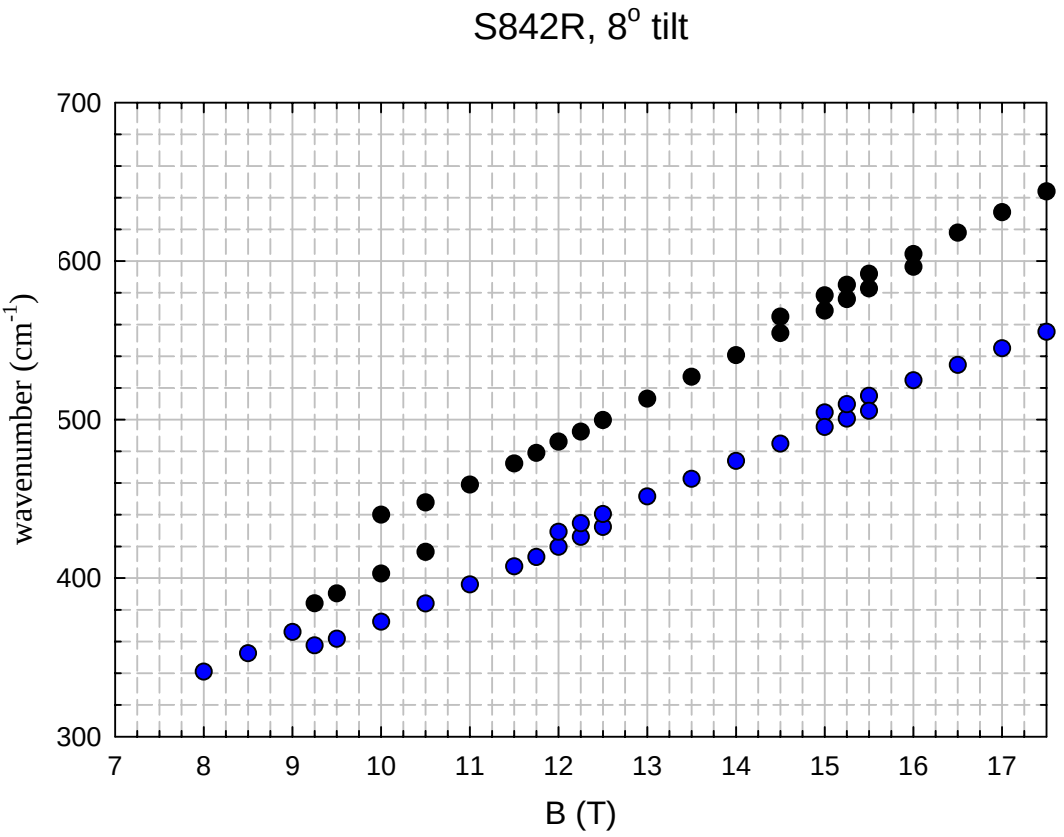
S842R, 8° tilt
wavenumber (cm-1)
B (T)
700
600
500
400
300
7
8
9
10
11
12
13
14
15
16
17

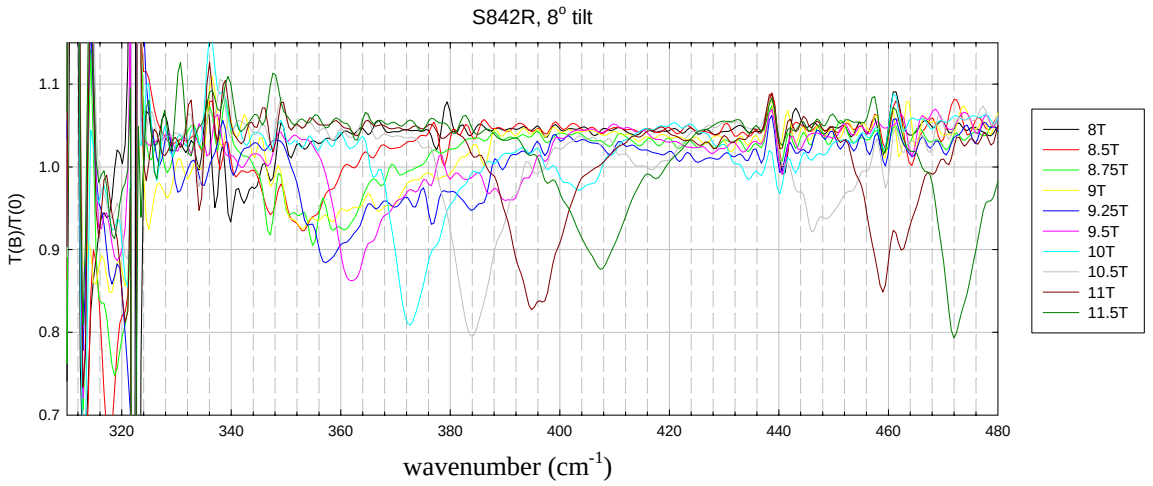
S842R, 8° tilt
T(B)/T(0)
wavenumber (cm-1)
8T
8.5T
8.75T
9T
9.25T
9.5T
10T
10.5T
11T
11.5T

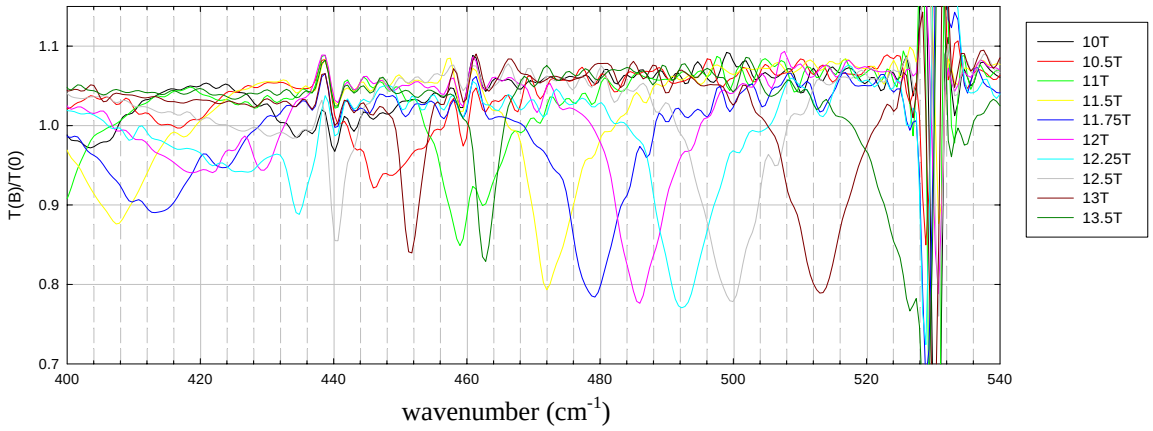
T(B)/T(0)
wavenumber (cm-1)
10T
10.5T
11T
11.5T
11.75T
12T
12.25T
12.5T
13T
13.5T

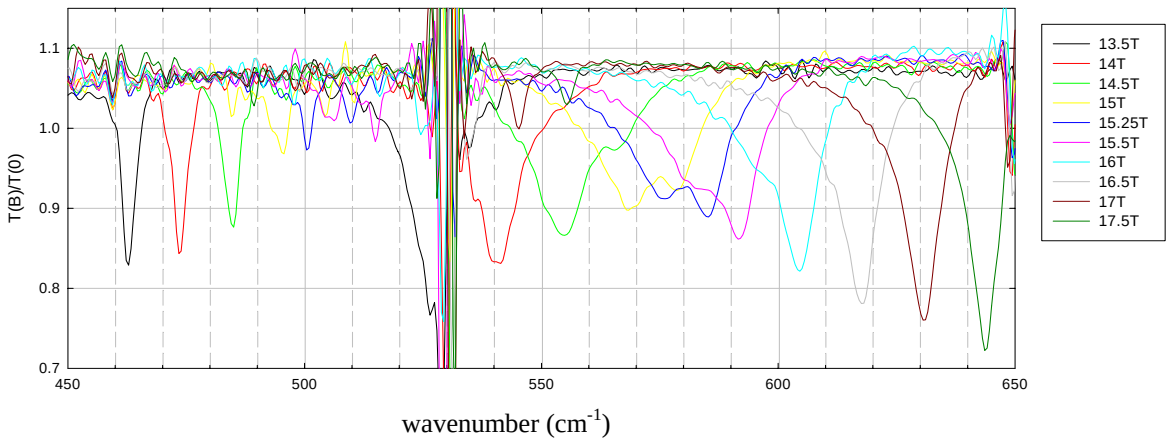
T(B)/T(0)
wavenumber (cm-1)
13.5T
14T
14.5T
15T
15.25T
15.5T
16T
16.5T
17T
17.5T

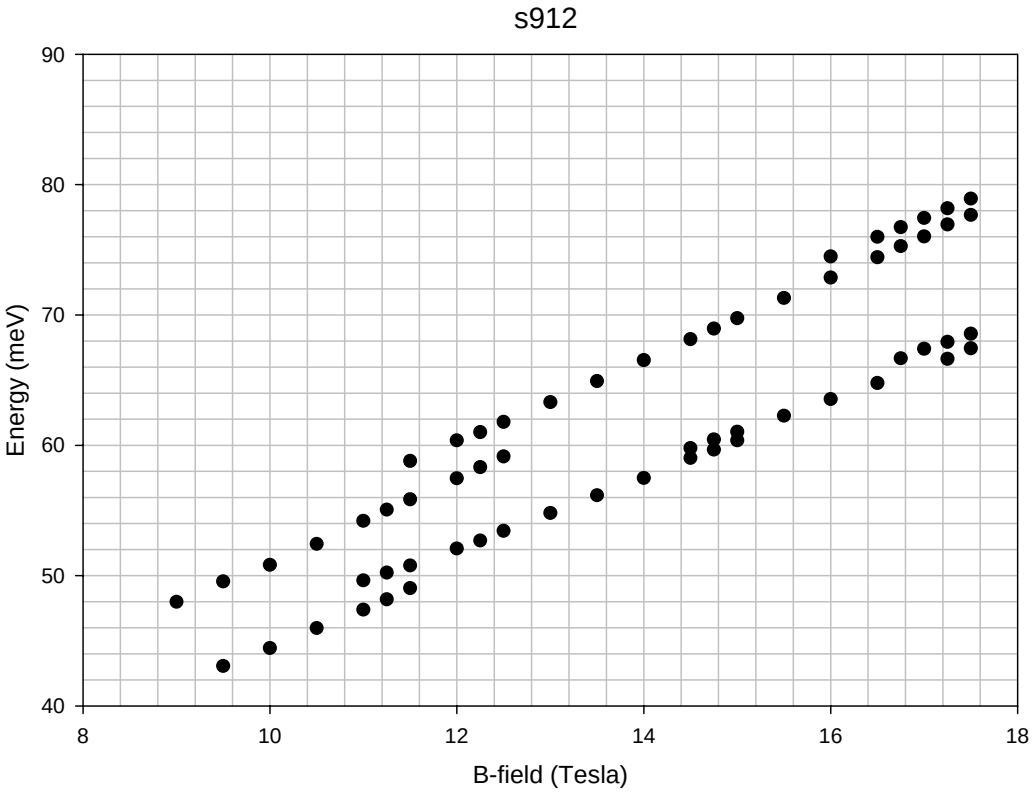
s912
Energy (meV)
B-field (Tesla)
90
80
70
60
50
40
8
10
12
14
16
18

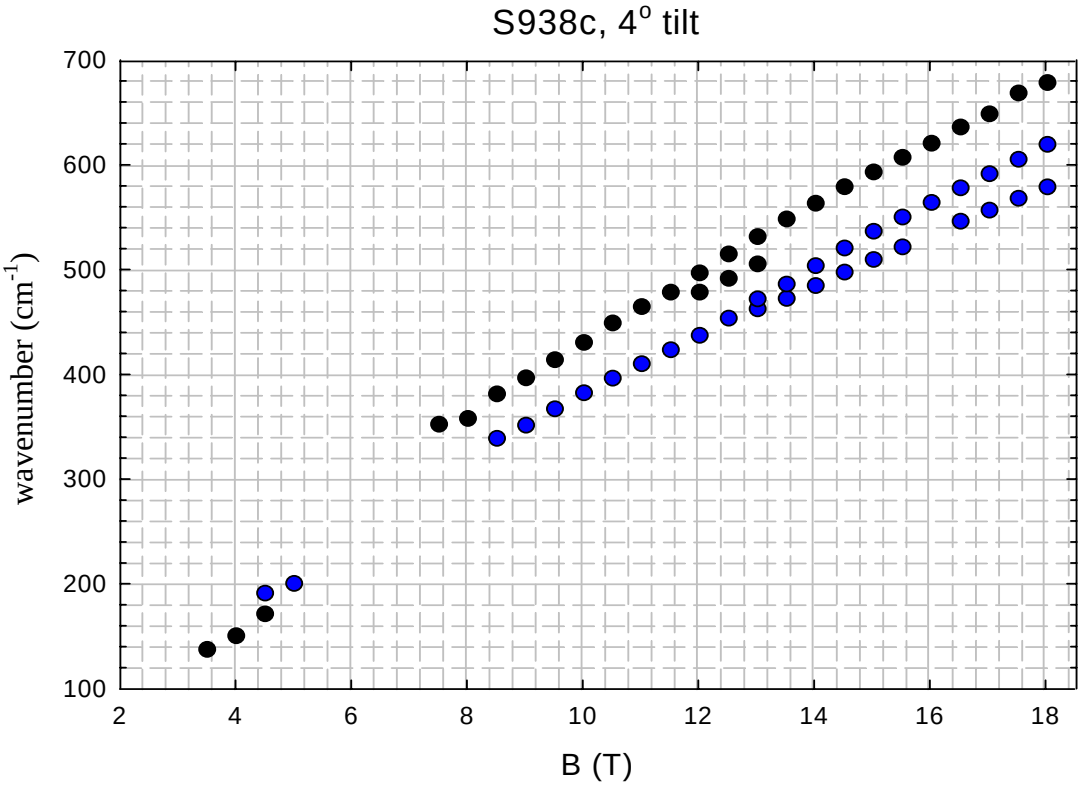
S938c, 4° tilt
wavenumber (cm-1)
B (T)
700
600
500
400
300
200
100
2
4
6
8
10
12
14
16
18

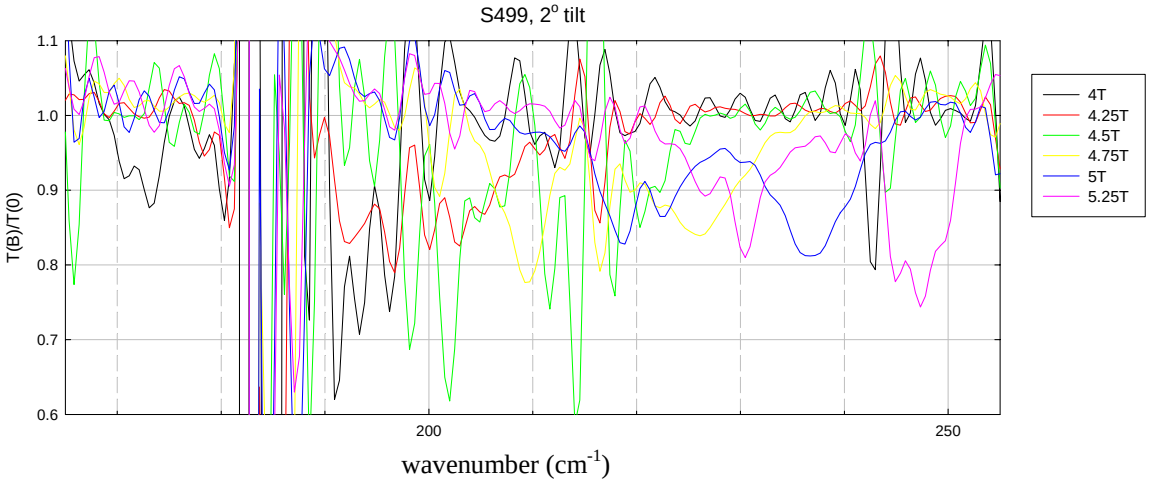
S499, 2° tilt
T(B)/T(0)
wavenumber (cm-1)
4T
4.25T
4.5T
4.75T
5T
5.25T

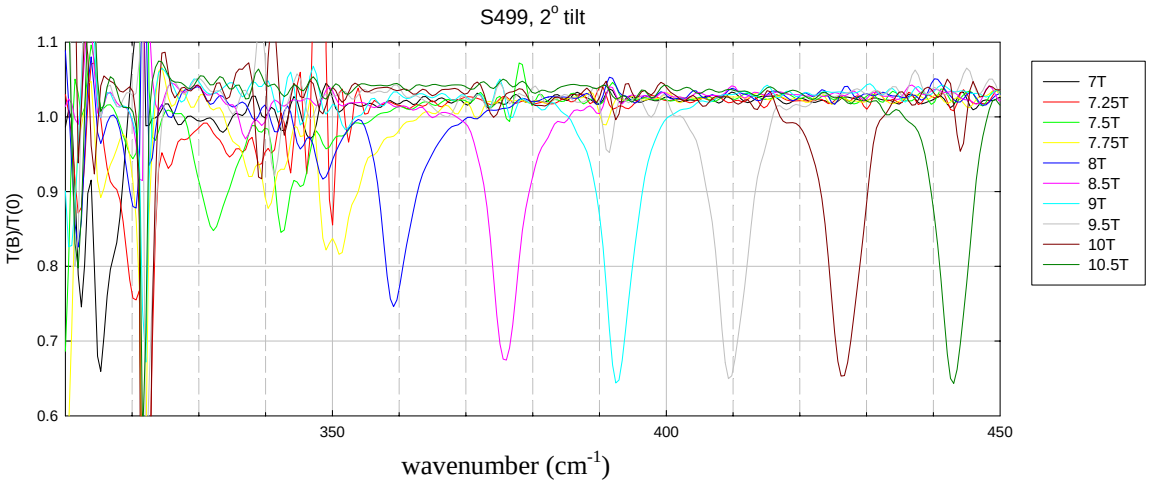
S499, 2° tilt
T(B)/T(0)
wavenumber (cm-1)
7T
7.25T
7.5T
7.75T
8T
8.5T
9T
9.5T
10T
10.5T

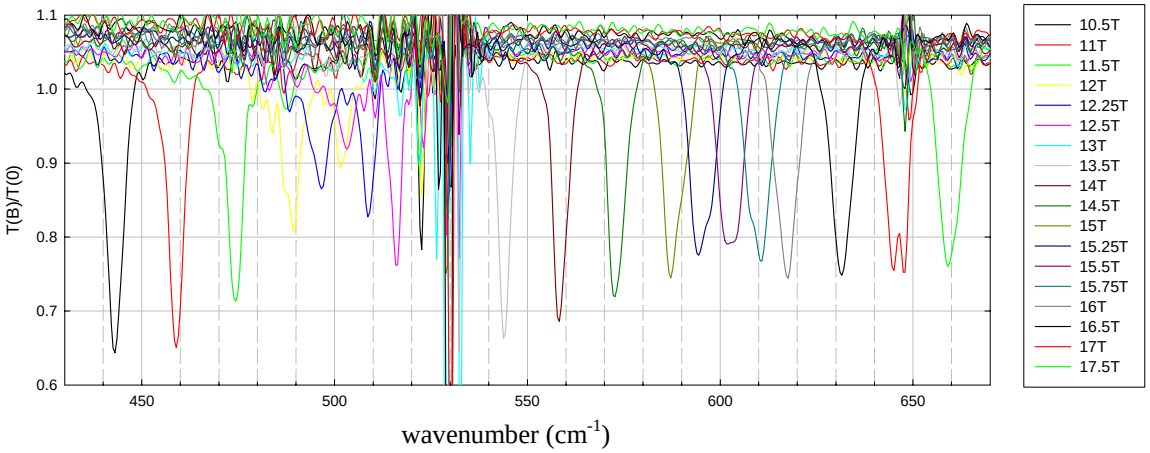
T(B)/T(0)
wavenumber (cm-1)
10.5T
11T
11.5T
12T
12.25T
12.5T
13T
13.5T
14T
14.5T
15T
15.25T
15.5T
15.75T
16T
16.5T
17T
17.5T

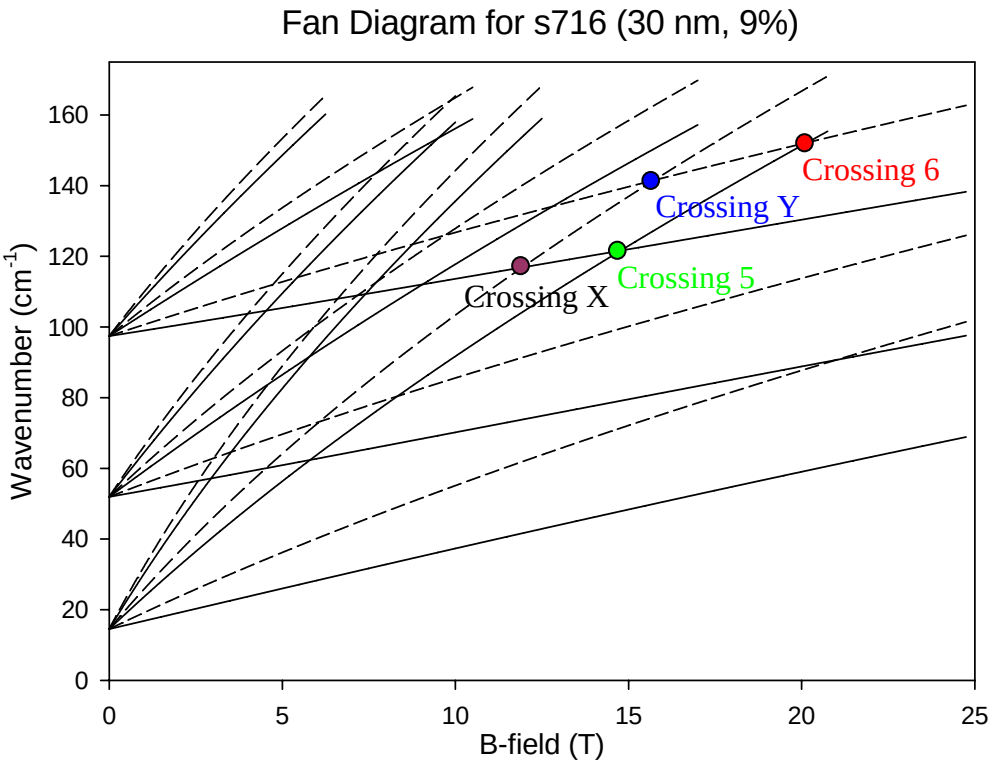
Fan Diagram for s716 (30 nm, 9%)
Wavenumber (cm-1)
B-field (T)
Crossing 6
Crossing Y
Crossing 5
Crossing X
0
20
40
60
80
100
120
140
160
0
5
10
15
20
25

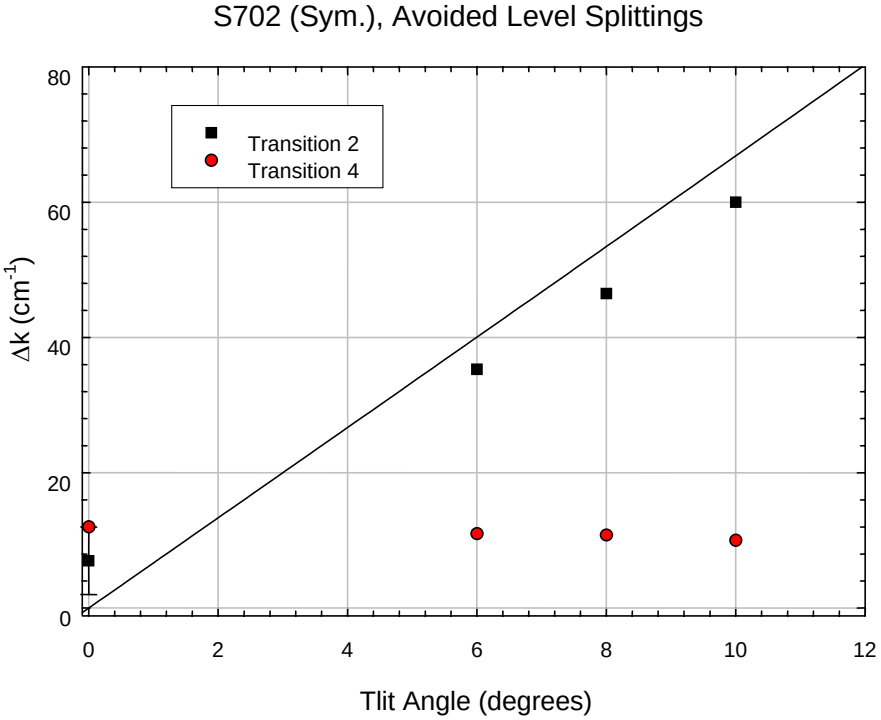
S702 (Sym.), Avoided Level Splittings
Transition 2
Transition 4
Δk (cm-1)
Tlit Angle (degrees)
0
20
40
60
80
0
2
4
6
8
10
12

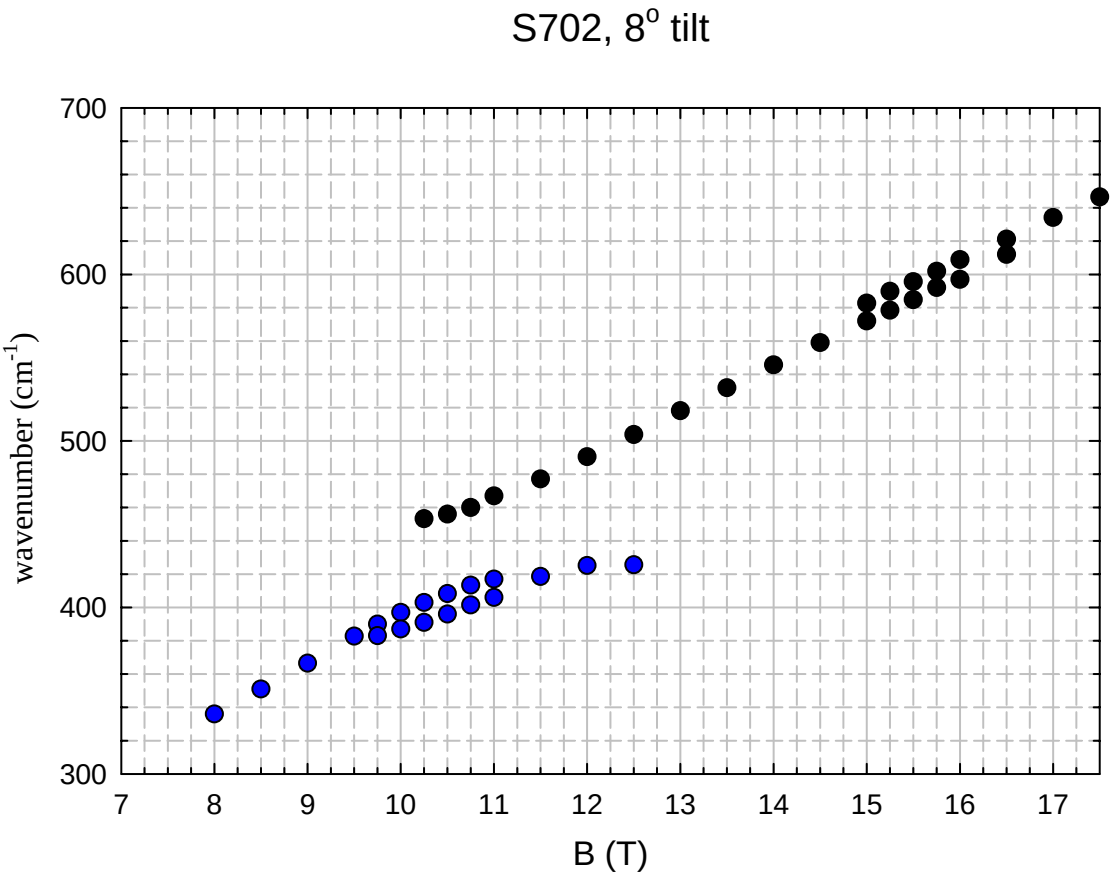
S702, 8° tilt
wavenumber (cm-1)
B (T)
700
600
500
400
300
7
8
9
10
11
12
13
14
15
16
17

S702, 8 degree tilt

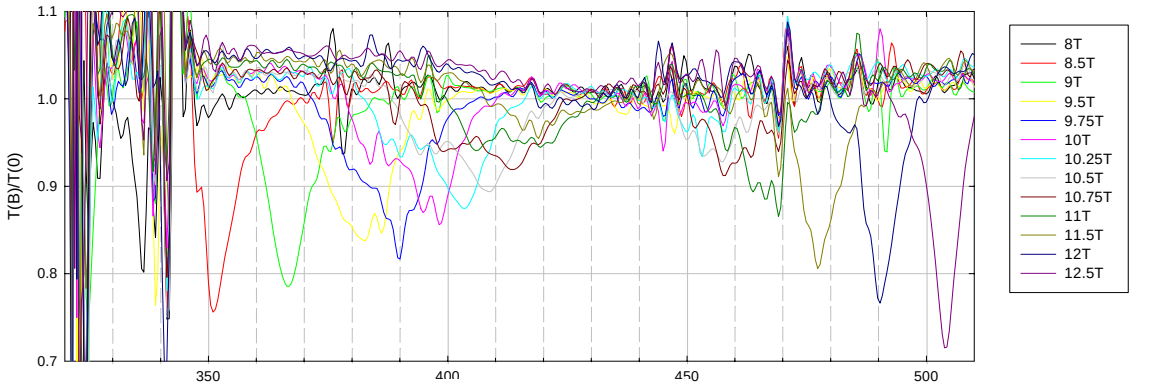

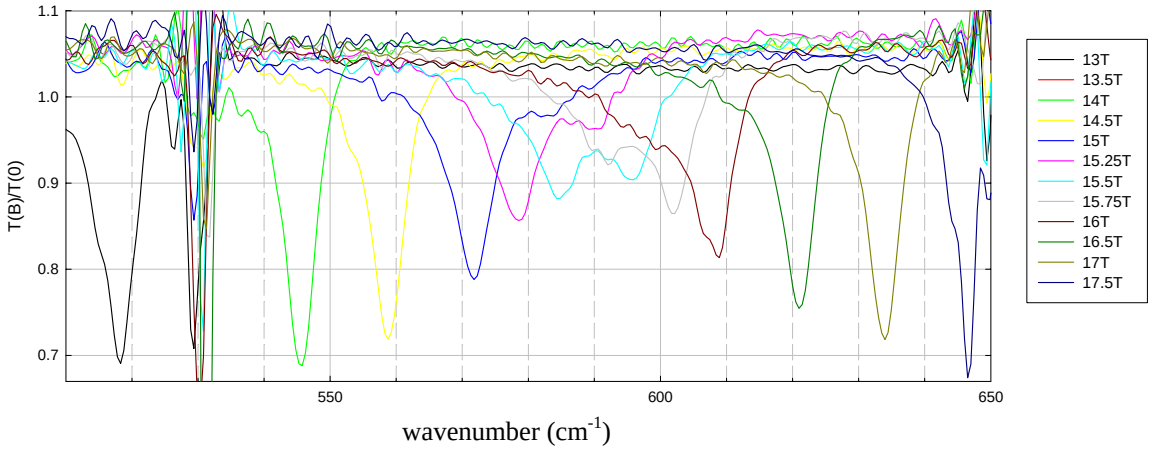

Appendix B – Sample Crossing Data

s702 (200 Å, 9%)	Crossing 1	Crossing 2	Crossing 3	Crossing 4
observed	**------**	**10.875 T**	**------**	**16.0 T**
175 Å, x = 8.1 %	8.58 T	10.78 T	11.53 T	15.16 T
187 Å, x = 8.1 %	8.07 T	10.16 T	10.84 T	14.30 T
200 Å, x = 8.1 %	7.51 T	9.48 T	10.09 T	13.38 T
212 Å, x = 8.1 %	7.02 T	8.88 T	9.42 T	12.56 T
225 Å, x = 8.1 %	6.52 T	8.27 T	8.75 T	11.72 T
200 Å, x = 8.3 %	7.64 T	9.63 T	10.24 T	13.56 T
200 Å, x = 9.0 %	8.04 T	10.11 T	10.76 T	14.16 T
200 Å, x = 10.25 %	8.70 T	10.89 T	11.62 T	15.17 T
200 Å, x = 12.25 %	9.58 T	11.93 T	12.78 T	16.52 T
200 Å, x = 15.0 %	10.34 T	12.78 T	13.70 T	17.50 T

Table B1: Observed and calculated crossing positions for sample s702.
(intended growth parameters: well width = 200 Å, x = 9 %)

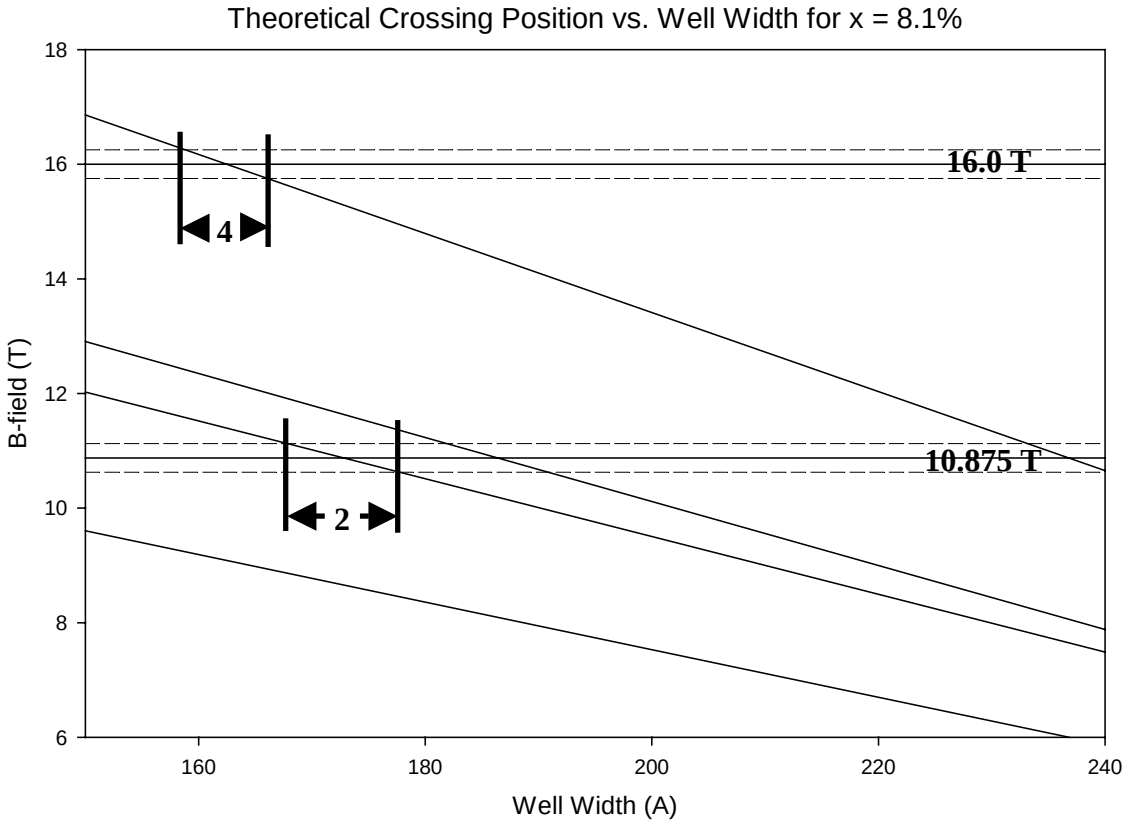

Figure B1: Plot of the predicted theoretical crossing positions vs. well width for a sample with an aluminum concentration of 8.1%. Observed crossings are those for s702.

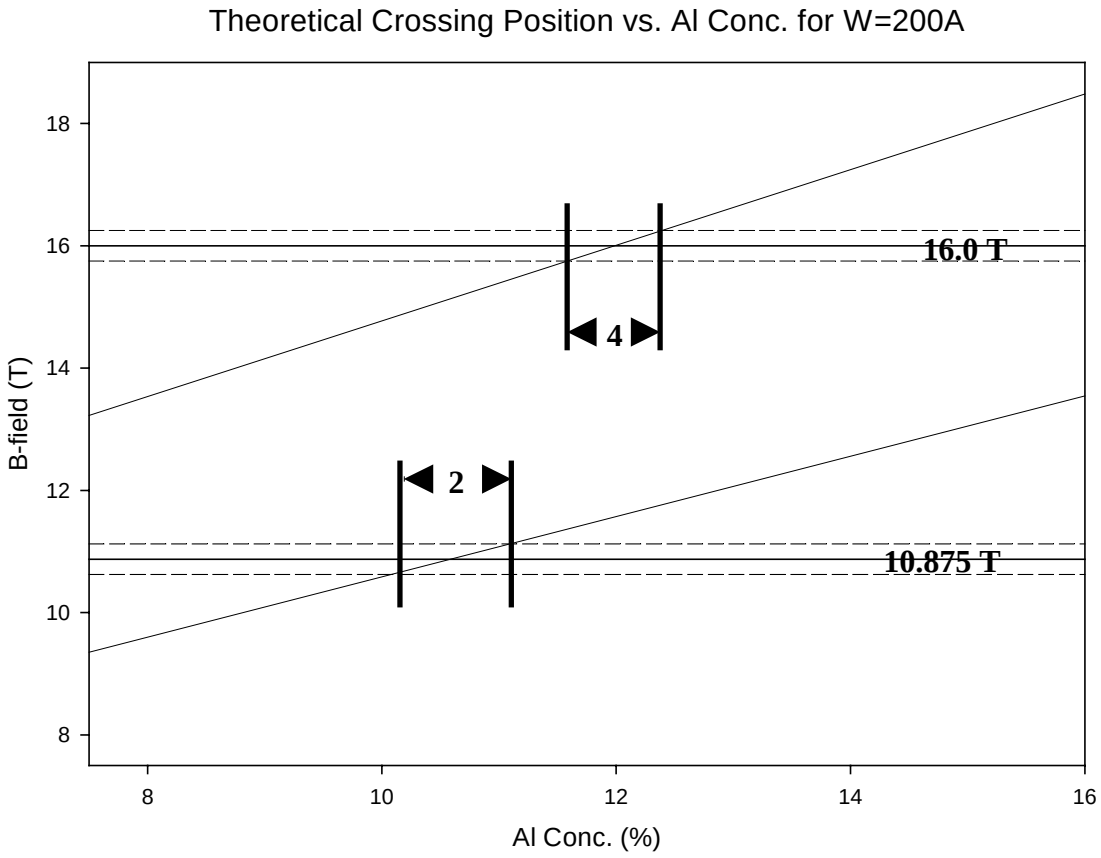

Figure B2: Plot of the predicted theoretical crossing positions vs. aluminum concentration for a well width of 200 Å. Observed crossings are those for s702.

s839 (250 Å, 15%)	Crossing 1	Crossing 2	Crossing 3	Crossing 4
observed	**-----**	**9.375 T**	**11.75 T**	**14.875 T**
225 Å, x = 15 %	8.51 T	10.62 T	11.32 T	14.71 T
200 Å, x = 12 %	9.37 T	11.65 T	12.46 T	16.10 T
212 Å, x = 12 %	8.58 T	10.71 T	11.42 T	14.87 T
225 Å, x = 12 %	7.83 T	9.81 T	10.43 T	13.68 T
237 Å, x = 12 %	7.21 T	9.08 T	9.62 T	12.71 T
250 Å, x = 12 %	6.63 T	8.37 T	8.85 T	11.76 T

Table B2: Observed and calculated crossing positions for sample s839.
(intended growth parameters: well width = 250 Å, x = 15 %)

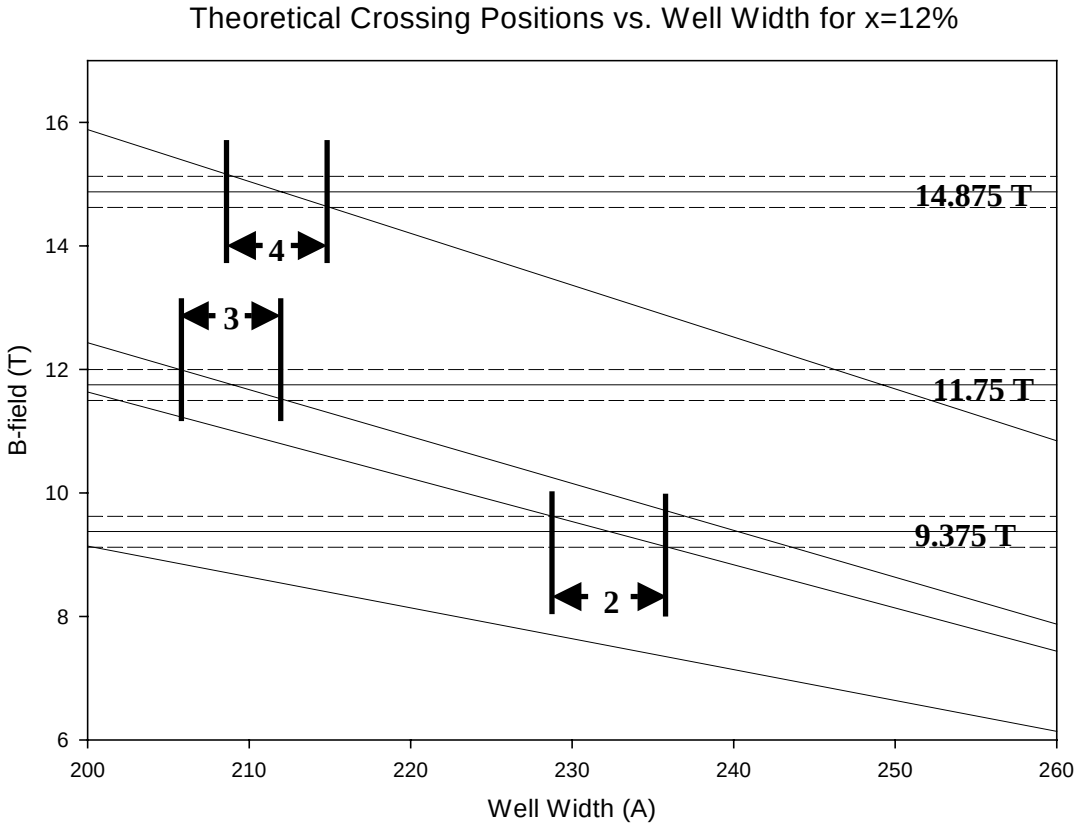

Figure B3: Plot of the predicted theoretical crossing positions vs. well width for a sample with an aluminum concentration of 12%. Observed crossings are those for s839.

s912 (230 Å, 15%)	Crossing 1	Crossing 2	Crossing 3	Crossing 4
observed	**11.25 T**	**12.25 T**	**14.75 T**	**17.0 T**
175 Å, x = 12.4 %	11.59 T	14.26 T	15.35 T	19.45 T
187 Å, x = 12.4 %	10.52 T	13.02 T	13.96 T	17.84 T
200 Å, x = 12.4 %	9.51 T	11.82 T	12.64 T	16.30 T
212 Å, x = 12.4 %	8.70 T	10.86 T	11.57 T	15.04 T
230 Å, x = 12.4 %	7.66 T	9.61 T	10.20 T	13.41 T
200 Å, x = 15 %	10.34 T	12.78 T	13.70 T	17.50 T

Table B1: Observed and calculated crossing positions for sample s912.
(intended growth parameters: well width = 230 Å, x = 15 %)

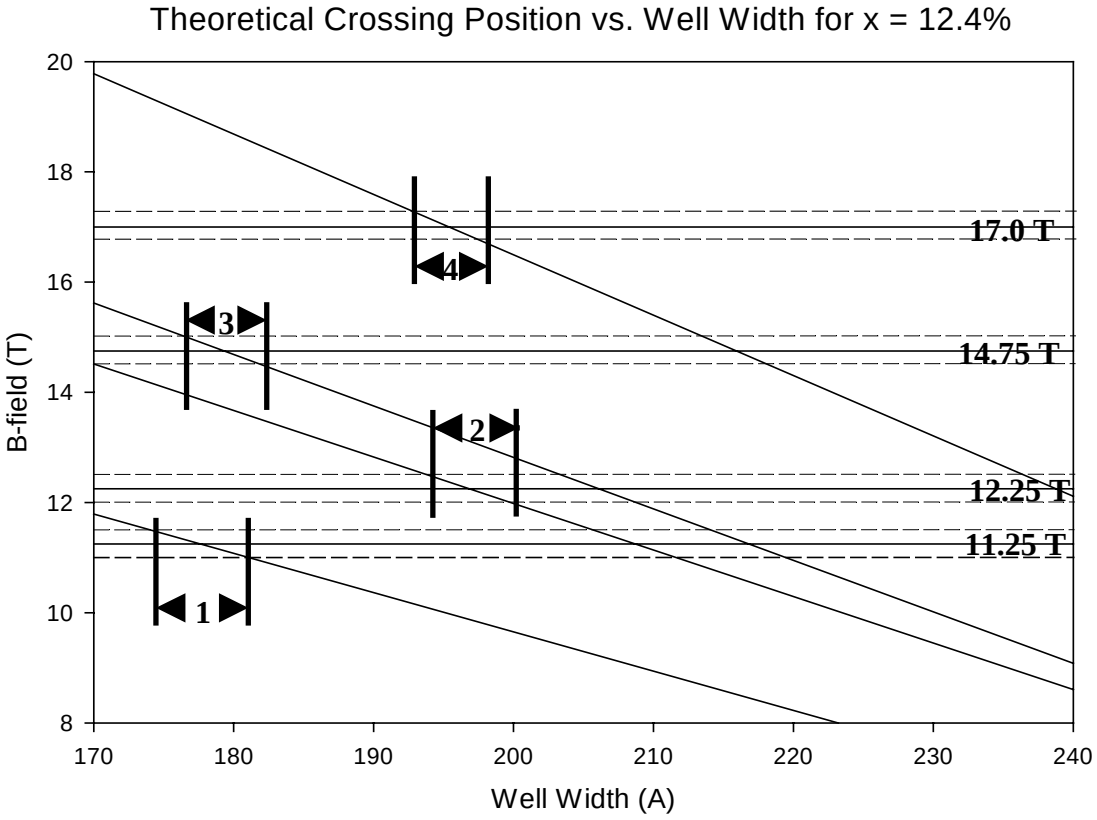

Figure B4: Plot of the predicted theoretical crossing positions vs. well width for a sample with an aluminum concentration of 12.4%. Observed crossings are those for s912.

Appendix C

Table of Samples

The following is a table of specific information concerning when and under what circumstances specific sample pieces were used to gather data. An explanation of column titles is given below:

Ref. # → A reference number for each sample run. This number can be useful since the same sample number could have been run multiple times and there are, on occasion, various pieces of the same sample run at different times.

Date Measured → The specific date that the particular sample piece in question was run.

Sample → The specific sample number and piece. Usually, when more than one piece of a sample is cut from the wafer, an additional letter is added to the end of the sample number to distinguish the various sample pieces. (ex: s842N and s842R).

B_{max} → The maximum B-field (in Tesla) the sample was run at. This number is usually 29 - 30 T if the magnet used was the water cooled resistive magnet at the NHMFL, or 16 – 17.5 T if it was the superconducting magnet, also at the NHMFL.

Substrate → The type of substrate material the sample was grown on.

W → The intended well width (in nm) for the sample.

Barrier → The composition of the barrier for the sample.

Sym. → The symmetric nature of the sample (S = symmetric, A = asymmetric).

n (10^{11}cm^{-2}) → The density of the sample as measured by Shubnikov-de Haas.

Comments → Any unusual or noteworthy comments concerning the sample run.

Ref. #	Date Measured	Sample	B_{max} (T)	Tilt (degrees)	Substrate	W (nm)	Barrier	Sym.	n ($10^{11}cm^{-2}$) From SdH	Comments
1	Aug. 22, 2002	S499	32	2	GaAs	30	$Al_{0.09}In_{0..91}Sb$	S	2.1	
2	Jan. 2003	S360	32	32	GaAs	30	$Al_{0.09}In_{0..91}Sb$	A	2.15 to 2.7	
3	Jan. 2003	S360	32	65	GaAs	30	$Al_{0.09}In_{0..91}Sb$	A	2.15 to 2.7	
4	Jan. 2003	S360	32	69	GaAs	30	$Al_{0.09}In_{0..91}Sb$	A	2.15 to 2.7	
5	Jan. 2003	S769	32	69	GaAs	30	$Al_{0.09}In_{0..91}Sb$	S	2.0	
6	Feb. 6, 2003	S203	5	0	GaAs	30	$Al_{0.07}In_{0..93}Sb$	A		
7	Feb. 7, 2003	S360’	17.5	30	GaAs	30	$Al_{0.09}In_{0..91}Sb$	A	2.15 to 2.7	
8	Feb. 7, 2003	S499’	5.9	2	GaAs	30	$Al_{0.09}In_{0..91}Sb$	S	2.1	
9	Feb. 7, 2003	S707	17.5	15	GaAs	20	$Al_{0.09}In_{0..91}Sb$	A	2.1	
10	Feb. 7, 2003	S499b	9.4	2	GaAs	30	$Al_{0.09}In_{0..91}Sb$	S	2.1	
11	Feb. 7, 2003	S360sr	17.5	30	GaAs	30	$Al_{0.09}In_{0..91}Sb$	A	2.15 to 2.7	
12	May 2003	S190	26	15	InSb	30	$Al_{0.07}In_{0..93}Sb$	A		
13	May 2003	S360	27	30	GaAs	30	$Al_{0.09}In_{0..91}Sb$	A	2.15 to 2.7	
14	May 2003	S360	32	69	GaAs	30	$Al_{0.09}In_{0..91}Sb$	A	2.15 to 2.7	
15	June 2, 2003	S842N	NA	0	GaAs	25	$Al_{0.15}In_{0..85}Sb$	S	4.0	Sample fell off mount
16	June 2, 2003	S716Q	17.5	2	GaAs	30	$Al_{0.09}In_{0..91}Sb$	S	1.4	
17	June 4, 2003	S194	17.5	0	InSb	30	$Al_{0.07}In_{0..93}Sb$	A		
18	June 4, 2003	S190	17.5	0	InSb	30	$Al_{0.07}In_{0..93}Sb$	A		
19	June 5, 2003	S716R	17.5	4	GaAs	30	$Al_{0.09}In_{0..91}Sb$	S	1.4	
20	June 6, 2003	S702	17.5	2	GaAs	20	$Al_{0.09}In_{0..91}Sb$	S	2.4	
21	June 7, 2003	S842R	17.5	4	GaAs	25	$Al_{0.15}In_{0..85}Sb$	S	4.0	
22	June 7, 2003	S716Q	17.5	25	GaAs	30	$Al_{0.09}In_{0..91}Sb$	S	1.4	
23	Oct. 2003	S702	17.5	0	GaAs	20	$Al_{0.09}In_{0..91}Sb$	S	2.4	
24	Oct. 2003	S702	17.5	10	GaAs	20	$Al_{0.09}In_{0..91}Sb$	S	2.4	
25	Oct. 2003	S707	17.5	0	GaAs	20	$Al_{0.09}In_{0..91}Sb$	A	2.1	
26	Oct. 2003	S707	17.5	10	GaAs	20	$Al_{0.09}In_{0..91}Sb$	A	2.1	
27	Oct. 2003	S842	17.5	0	GaAs	25	$Al_{0.15}In_{0..85}Sb$	S	4.0	
28	Oct. 2003	S842	17.5	11	GaAs	25	$Al_{0.15}In_{0..85}Sb$	S	4.0	
29	Oct. 2003	S842	17.5	14	GaAs	25	$Al_{0.15}In_{0..85}Sb$	S	4.0	
30	Oct. 2003	S842	17.5	19	GaAs	25	$Al_{0.15}In_{0..85}Sb$	S	4.0	
31	Oct. 2003	S842	17.5	6	GaAs	25	$Al_{0.15}In_{0..85}Sb$	S	4.0	
32	Oct. 2003	S842R	17.5	11	GaAs	25	$Al_{0.15}In_{0..85}Sb$	S	4.0	

Ref. #	Date Measured	Sample	B_{max} (T)	Tilt (degrees)	Substrate	W (nm)	Barrier	Sym.	n ($10^{11}cm^{-2}$) From SdH	Comments
33	Oct. 27, 2003	S499	26	13	GaAs	30	$Al_{0.09}In_{0..91}Sb$	S	2.1	
34	Oct. 28, 2003	S499	22	2	GaAs	30	$Al_{0.09}In_{0..91}Sb$	S	2.1	
35	Oct. 29, 2003	S842R	27	4	GaAs	25	$Al_{0.15}In_{0..85}Sb$	S	4.0	
36	Oct. 30, 2003	S716R	29	4	GaAs	30	$Al_{0.09}In_{0..91}Sb$	S	1.4	
37	Oct. 31, 2003	S716R	24	11	GaAs	30	$Al_{0.09}In_{0..91}Sb$	S	1.4	
38	Feb. 16, 2004	S839R	17.5	4	GaAs	25	$Al_{0.15}In_{0..85}Sb$	S	3.9	Slightly lower density than s842
39	Feb. 17, 2004	S702	17.5	8	GaAs	20	$Al_{0.09}In_{0..91}Sb$	S	2.4	
40	Feb. 17, 2004	S702Q	17.5	6	GaAs	20	$Al_{0.09}In_{0..91}Sb$	S	2.4	Wedge came unglued → tilt was ≈ 0 degrees
41	Feb. 18, 2004	S842H	17.5	6	GaAs	25	$Al_{0.15}In_{0..85}Sb$	S	4.0	Data implies smaller angle
42	Feb. 18, 2004	S842R	17.5	8	GaAs	25	$Al_{0.15}In_{0..85}Sb$	S	4.0	
43	Feb. 19, 2004	S912A	17.5	4	GaAs	23	$Al_{0.15}In_{0..85}Sb$	S		Higher density than s842
44	Feb. 20, 2004	S702Q	17.5	6	GaAs	20	$Al_{0.09}In_{0..91}Sb$	S	2.4	
45	Feb. 20, 2004	S842R	17.5	6	GaAs	25	$Al_{0.15}In_{0..85}Sb$	S	4.0	
46	Feb. 21, 2004	S499	17.5	2	GaAs	30	$Al_{0.09}In_{0..91}Sb$	S	2.1	
47	Feb. 21, 2004	S360	NA	2	GaAs	30	$Al_{0.09}In_{0..91}Sb$	A	2.15 to 2.7	Signal too low for good measurement
48	June 6, 2004	S936C	17.5	4	GaAs	25	$Al_{0.12}In_{0..88}Sb$	S	5.3	Density desc. with transmission AC #1 obscured by GaAs phonons
49	June 7, 2004	S939C	17.5	4	GaAs	11.5	$Al_{0.15}In_{0..85}Sb$	S	4.0	No observed anti-crossings Trans. linewidth does not vary much
50	June 8, 2004	S917	17.5	8	InSb	20	$Al_{0.15}In_{0..85}Sb$	S		Interference fringes
51	June 9, 2004	S938C	18	4	GaAs	36	$Al_{0.12}In_{0..88}Sb$	S	8.7	Low mobility → broad linewidths Possible 2^{nd} subband occupied
52	June 9, 2004	S928C	18	4	GaAs	14	$Al_{0.25}In_{0.75}Sb$	S		
53	June 10, 2004	S928D	18	8	GaAs	14	$Al_{0.25}In_{0.75}Sb$	S		
54	June 11, 2004	S938C	18	8	GaAs	36	$Al_{0.12}In_{0..88}Sb$	S		
55	June 12, 2004	S936C	18	10	GaAs	25	$Al_{0.12}In_{0..88}Sb$	S		
56	June 13, 2004	S917	7	4	InSb	20	$Al_{0.15}In_{0..85}Sb$	S		